THE LUX DARK MATTER EXPERIMENT: DETECTOR PERFORMANCE AND ENERGY CALIBRATION

by

PATRICK PHELPS

Submitted in partial fulfillment of the requirements for
the degree of Doctor of Philosophy

Dissertation Advisers:
Daniel S Akerib & Thomas A Shutt
Department of Physics

CASE WESTERN RESERVE UNIVERSITY

August, 2014

Case Western Reserve University

SCHOOL OF GRADUATE STUDIES

We hereby approve the thesis/dissertation of

Patrick Harvey Phelps
candidate for the degree of Doctor of Philosophy*.

Committee Chair
Dr. Daniel Akerib

Committee Member
Dr. Thomas Shutt

Committee Member
Dr. John Ruhl

Committee Member
Dr. Stacy McGaugh

Date of Defense
July 3$^{\text{rd}}$, 2014

*We also certify that written approval has been obtained for any proprietary material contained therein.

For my parents, who supported me every step of the way, hard to believe it's done.

Contents

List of Tables

List of Figures

“The lights begin to twinkle from the rocks:
The long day wanes: the slow moon climbs: the deep
Moans round with many voices. Come, my friends,
’T is not too late to seek a newer world.
Push off, and sitting well in order smite
The sounding furrows; for my purpose holds
To sail beyond the sunset, and the baths
Of all the western stars, until I die.
It may be that the gulfs will wash us down:
It may be we shall touch the Happy Isles,
And see the great Achilles, whom we knew.
Tho’ much is taken, much abides; and tho’
We are not now that strength which in old days
Moved earth and heaven, that which we are, we are;
One equal temper of heroic hearts,
Made weak by time and fate, but strong in will
To strive, to seek, to find, and not to yield.”

Ulysses, Alfred Tennyson

Acknowledgements

There was a point where I wondered if this project and document would ever be written, when the light at the end of the tunnel could have been the proverbial train. Indeed, this document was only completed thanks to the supporting efforts of many, many people for whom I am thankful. Of course I have to start with Dan and Tom, a pair of advisors unlike any other, who challenged me, spurred me, taught me, and shepherded me through an incredible experience over seven years. May their journey to the west bring them happiness and opportunity.

I also couldn't have done this without the years of support by my family, working behind the scenes to encourage in me a love of science and endless support when things went awry.

To my incredible coworkers and friends, I thank you for keeping me sane. To Ken Clark, thank you for being a mentor to a foolish young student, even when he froze his shoes with LN. To Tim Atherton, for giving us the unicorn as the symbol of LUX, sadly no limits on the horn-chirality yet. To Kati and Rosie, you were wonderful office mates and I apologize for my grumpiness. To Chang I appreciated your insights and witticisms. To Alastair for the wonderful debates on probability theory, though you were mostly right and probably wrong. To Markus, Attila, and Jeremy Mock, we really did it, we really built an experiment and it worked, we'll always have the Silver Star. To the Alexey, "Sex-Machine," for teaching me how to fix the pumps with a hammer, to Ethan for teaching me how to create electrical shielding at two in the morning, to James Nikkel for teaching me how to be Canadian, yes, people still think I'm Canadian, and to Maria del Carmen Carmona Benitez for sharing in the burden of carrying an experiment.

To Luke, Amanda, Matt, Chad, Carlos, Scott, Mia, Yun-ting, Blake, Blair, Chris, Nick and Mary, J.T., Heather and Mike Patrick, Mike Wolf, David Malling, Geoff, Alex, James, Rachel, Dave Jacobs, Joel and Sam, I salute you for being better people than I and for the wonderful laughter, friendship, and celebratory beers.

Finally, to those I've forgotten, not because you aren't important, but because my memory is flawed, thank you, for all the things you did or didn't do.

The LUX Dark Matter Experiment: Detector Performance and Energy Calibration

Abstract

by

PATRICK PHELPS

Dark matter, the mysterious substance that seems to make up most of the mass of the universe has never been detected in the laboratory. In this document I outline the current world's leading experiment, LUX, to look for a class of dark matter, the Weakly Interacting Massive Particle. I outline the general principles of searching for dark matter through low background detectors and event rejection, I move on to a description of the LUX experiment and its performance, reviewing its internal structure and subsystems including a novel heat exchange system that expedited system readiness and resulted in a stable platform for WIMP searching. The LUX energy reconstruction is then examined, followed by a breakdown of signal fluctuations as a function of energy as part of our understanding of background discrimination in this class of detectors. Finally, I review the first LUX WIMP search result, culminating in the world's most sensitive limit on the spin-independent WIMP-nucleon cross section, before moving to a discussion of next steps in the search for dark matter for LUX and next generational experiments.

Chapter 1

Evidence for Dark Matter

The last 100 years have been an incredibly productive time for the field of physics. Since the founding of general relativity in 1916 and modern quantum theory in the 1920's-1930's we have witnessed the birth of the Standard Model, which accurately describes the interactions of all matter we have observed, as well as the emergence in the 1990's of the concordance cosmological model, ΛCDM, which successfully describes the structure of our universe on the largest scales. Yet, the two models are disparate, with ΛCDM requiring the existence of new kinds of matter and energy which are little understood within or beyond the structure of the Standard Model. Indeed, since the 1930's, evidence has been slowly accruing that most of the universe is made of substances unlike anything described in the Standard Model, referred to as dark matter and dark energy, substances which we have never observed in the laboratory.

The study of dark matter has a long history with evidence coming from a wide variety of astrophysical studies on many different scales. From the early observations of Oort [1] and Zwicky [2], studying star dynamics in galaxies and clusters, from our understanding of big bang nucleosynthesis (BBN) [3], to modern studies of the cosmic microwave background radiation (CMB) [4], [5], [6] and large-scale structure surveys [7], [8], on cosmological distance scales, dark matter appears to be an integral part of the picture of how the universe works. These studies tell us this dark matter is unlike any form of matter we know, being neither baryonic nor relativistic neutrinos [9].

We conclude that no particle in the Standard Model can account for the dark matter component required in ΛCDM. Stepping beyond the Standard Model, a range of possibilities have been considered as constituents of the dark matter, the most generally favored being some form of Weakly Interacting Massive Particle (WIMP) though other candidates, such as the axion, or modifications to our laws of gravity are also being considered.

In this chapter we review the cosmological evidence for dark matter, as well as provide a brief overview of the currently preferred candidates. This is followed in chapter 2 by an examination of detector technologies aimed at finding direct evidence of this elusive substance. Chapter 3 details the LUX detector, a currently ongoing effort to directly detect WIMPs in a laboratory on Earth. Chapter 4 continues the detailing of the LUX detector, focusing on detector stability as provided by a novel heat exchange system designed to provide a stable platform on which to conduct this search. In chapter 5, we take up the treatment of the LUX energy reconstruction, finding an energy scale independent of event-site microphysics. Chapter 6 then builds on the results of chapter 5, examining the microphysics which underlie the dark matter search power of the LUX detector. Finally, in chapter 7, we conclude with the first LUX WIMP search result and comment on next steps both for the LUX experiment and further generations of dark matter searches.

1.1 Modified Gravity

Though a large component of the universe appears to be missing based on our knowledge of general relativity (GR), we could equivalently argue that the laws of gravitation need updating, removing the need for new exotic forms of matter. Modified gravity theories are a rich topic with many different proposed possible modifications, with classes of theories such as Einstein-Aether, TeVeS, Galileons, Ghost Condensates, and models of extra dimensions. In general, these types of theories modify either the gravitational couplings, the number of dimensions, the mass of the gravitational force carrier, or the distance dependence of the gravitational force at some scale [10]. The main appeal of such classes of theories is the potential to no longer require a $\sim 95\%$ dark universe, and certain classes of modified gravity theories are more accurate in the reconstruction of galactic rotation curves than ΛCDM with fewer free parameters [11], [12].

Modified gravity provides an interesting alternative to the ΛCDM picture, which we discuss further in section (1.2.1); however, tests of general relativity such as measurements of solar gravitational deflection of radio waves from distant sources agree very well with predictions from GR [13]. This leads to the difficulty of creating a theory that is simultaneously theoretically consistent, meets all stringent constraints from the tests of GR, and diverges from GR at a significant enough level that it can explain much of the dark sector.

While modified gravity is an interesting topic, with many ongoing theoretical efforts, it is outside the scope of this work and for the rest of this document we will work in the standard ΛCDM framework described below, referring the reader to one of the comprehensive reviews of the modified gravity field, such as [10] or [12].

1.2 Historical Evidence for Dark Matter

Since the early 1930's, evidence has gradually accumulated for what is interpreted as a large dark component to the universe. While modifications to general relativity have been attempted to explain possible measured discrepancies, the vast majority of results are consistent with a new form of matter, referred to as cold dark matter. Evidence has been observed across a wide range of scales, from the "small" scale of galactic rotation curves to the largest scales observable, set by the cosmic microwave background. Evidence also arises through the observation of gravitational lensing in clusters of galaxies, including the well-known bullet cluster [14]. These measurements in the last 20 years have largely converged into the current picture of concordance cosmology, ΛCDM.

1.2.1 ΛCDM

The current model of cosmology, ΛCDM, is a six-parameter model with the parameters of most interest here being the density of baryons and dark matter with respect to the critical density. The critical density is defined as the energy-density required for a spatially flat universe. Studies of the CMB, such as the new PLANCK satellite results, demonstrate that the universe is spatially flat and find dark matter composes 26.8% of the energy-density with respect to the critical density [15]. At the same time, these measurements tell us 4.9% of the energy-density is ordinary baryonic matter, and the remaining 68.3% is composed of dark energy, a substance that seems to underlie the accelerating expansion of the universe observed today [15]. The finding of consistency with the six-parameter ΛCDM model by modern experiments such as PLANCK and WMAP, [4], adds a large amount of weight to the idea of particle dark matter with supporting evidence accumulated in other ways as well.

1.2.2 Galaxy and Cluster Dynamics

The first observations of the need for a dark matter component in cosmology were done by Oort and Zwicky in 1932 and 1937, respectively. Both Oort and Zwicky were interested in the dynamics of galaxies and clusters of galaxies. While Oort observed anomalous mass-to-light ratios in N.G.C 4594, the Sombrero Galaxy, measured to be ~ 10 times larger than in the area near the Sun, Oort did not postulate the existence of extensive dark matter components but instead possible light absorption in the central region of the galaxy [1]. Zwicky's studies of the Coma cluster were the initial basis of the for the large part dark matter must play in maintaining galactic dynamics. Calling this dark matter "dunkle materie," Zwicky observed mass-to-light ratios of 500, well above what could be explained away by absorption [2]. Modern surveys of galaxy rotation curves, done with the 21 cm hydrogen (H1) line, continue to support that galaxies are found in the center of large dark matter halos, extending significantly past the radii typical for their stellar components, where this dark matter dominates the amount of luminous mass and thus dominates dynamics of the galaxies as a function of radii outside the central most regions [16].

1.2.3 Cosmology

Galaxies and clusters of galaxies provide evidence for clumping of dark matter over a range of length scales from several hundred thousand light years to one hundred million light years, larger scales can be probed with baryon acoustic oscillations (BAO) and the Cosmic Microwave Background (CMB).

BAO are the periodic oscillations in the clustering of baryonic matter at the largest scales, the result of oscillations in the primordial plasma, the initial mixture of protons, electrons, and photons, that also gives rise to the CMB. In the early universe, temperatures were high enough that the formation of neutral hydrogen was largely suppressed by high energy photons. However, as the universe expanded and cooled, the photons eventually lost enough energy that neutral hydrogen could form in a process called recombination. The formation of neutral hydrogen then made the universe optically transparent to the photons, resulting in a phase-change from a coupled plasma of baryons and photons, to a decoupled universe where the photons could free stream. After the plasma cools, and the photons decouple from the protons and electrons, sound waves in the initial plasma leave shells of baryons at characteristic horizon sizes, providing observable standard rulers that are used to measure ΛCDM parameters [17], [7].

The CMB also arises from the primordial plasma, namely at the time of recombination and resulting photon decoupling. Since that time, these CMB photons have traveled through the universe largely without interacting, red-shifting until they are at the current observed temperature of 2.72548 ± 0.00057 K [18]. Though incredibly uniform in temperature, correlations in the tiny fluctuations around this mean temperature allow us to extract a large amount of information, providing strong constraints on many of the ΛCDM parameters including the overall dark matter density from which we derive the numbers quoted in 1.2.1 [15], [5].

1.2.4 Gravitational Lensing

Another form of evidence for dark matter is gravitational lensing, the bending of light due to the gravitational potentials between the observer and source. Lensing provides a direct spatial map of the mass density of clusters of galaxies. While strong-lensing, in which multiple images or even Einstein arcs are observed, is of use in mapping dark matter distributions internal to clusters, [19], it is weak-lensing, in which lensing can only be reconstructed statistically, that is often used in these examinations [20].

In addition to normal lensing measurements to map dark matter distributions about galaxies and clusters of galaxies, lensing, when combined with X-ray gas measurements and optical imagery has proven especially interesting in the case of 1E 0657 - 56, commonly referred to as the "bullet-cluster." Here, two clusters have recently collided, passing through each other, with the gas from each galaxy being observed to have interacted and lag behind the stellar component as seen through the combination of X-ray (gas) and optical (stellar) observations [14]. Corresponding measurements of weak-lensing for the two clusters show that the majority of the mass is observed to follow the stellar component of the clusters, indicating that the majority of the mass passed through without interacting. From this we infer that the majority of the mass in the clusters is non-interacting as would be expected for dark matter, with a measured 8σ separation between the center of mass from lensing and the observed mass peaks in baryonic gas [21].

Having now identified the large amount of evidence for some dark matter component of the universe, we turn to the obvious question, what is the identity of the dark matter?

1.3 Dark Matter Candidates

As a large amount of evidence points to 26.8% of the energy-density of the universe to be dark matter, an obvious question is then what makes up this dark component. While originally postulated to possibly be the result of small planets or dead stars, knowledge of big-bang nucleosynthesis has forced us to confront the paradigm that the dark matter is non-baryonic in nature. From structure formation, we derive that the dark matter must be non-relativistic in the early universe, ruling out obvious candidates such as neutrinos. We conclude this chapter by examining the two currently favored candidate particles, the axion and the WIMP, both of which arise out of other areas of physics than our desire to identify a dark matter candidate. Searches for both axions and WIMPs are ongoing, with no confirmed observation of either at the present time.

1.3.1 Standard Model Dark Matter

When it first became apparent that a large amount of mass was in the form of dark matter, the first natural candidate was to assume that this dark matter was simply regular baryonic matter, planets or dead stars collectively referred to as Massive Compact Halo Objects (MACHOs). While this assumption seemed natural at the time, big-bang nucelosynthesis (BBN) results confirmed that dark matter can not be baryonic in nature due to constraints on the baryon to photon ratio, η_{10}, arising from the upper limits on primordial deuterium, with increasing baryonic concentration resulting in a longer period for BBN to proceed resulting in a reduction in the deuterium fraction with respect to the relic ^{4}He abundance [9]. Recent results from BBN constrain $\Omega_b h^2 = 0.02202 \pm 0.00046$, largely from measurement of deuterium abundance through deuterium absorption lines [3]. Here Ω_b is the ratio of the energy-density of baryons to the critical density, so that we write the energy-density of the i^{th} component as:

$$\Omega_i \equiv \frac{\rho_i}{\rho_c} = \frac{8\pi G\rho_i}{3H^2}, \tag{1.3.1}$$

where H is the Hubble parameter, the value of which today we refer to as the Hubble Constant, H_0, related to h above by $H_0 \equiv 100\,h\,\mathrm{kms^{-1}\,Mpc^{-1}}$, and found to have a value of 67.3 ± 1.2 km s^{-1} Mpc^{-1} [15].

Independent of BBN measurements of baryonic concentrations, modern CMB surveys such as WMAP and PLANCK can verify the baryon-to-photon ratio at the time of the CMB formation, leading to recent more precise constraints of $\Omega_b h^2 = 0.02207 \pm 0.00033$ [15], in good agreement with BBN measurements, while also directly measuring the overall matter energy-density, $\Omega_M = 0.3175$ [15].

From these measurements it is clear dark matter cannot be baryonic in nature, but the standard model also contains non-baryonic candidates for dark matter, the neutrinos, which must have small masses to explain the observed flavor-oscillation [22]. However, structure formation models require that dark matter be "cold," non-relativisitc at the time galaxy structure formation begins, as otherwise smaller scale density fluctuations are smoothed out by the free-streaming neutrinos. Indeed, models of early universes in which neutrinos are the dominant form of dark matter fail to produce structures that collapse gravitationally below the supercluster scale, $\sim 10^{15}$ solar masses, in direct contrast to what we observe [23].

Thus we conclude the standard model contains no particles that naturally fill the roll of dark matter and instead turn to hypothesized particles that could be dark matter candidates, such as the axion and the WIMP. Other possible dark matter candidates do exist, the sterile neutrino and primordial black holes for example, but the axion and the WIMP have emerged as overall favored candidates which are the focus of current experimental searches.

1.3.2 Axions

The axion was a particle proposed as a way to solve the strong CP problem, the observation that although strong interactions in the standard model can theoretically violate CP (charge-parity) symmetry no observation of this effect has been documented, but in time have also emerged as a DM candidate. The main test of strong interaction CP violation is an observable neutron electric-dipole moment (nEDM) [24]. As currently no detection of the nEDM has been observed, with current best limits constraining its value to $< 2.9 \times 10^{-26}$ e-cm [25], the lack of CP violation in strong interactions is viewed as a fine-tuning problem within the standard model.

Axions, if they exist, would solve this problem, and could, for a certain range of couplings and masses, produce possible dark matter candidates that could be observed in the laboratory [26]. As the original predicted axion, with a mass ~ 100 keV, has already been ruled out, searches instead focus on "invisible" axion models, in which the axion decouples at very high temperature (early time), $T_{\text{decoupling}} \gg T_{\text{Electroweak}}$, with the result being axions of extremely low mass [24].

Despite their predicted light masses, axions are candidates for dark matter as they can be produced non-relativistically through various mechanisms such as the decay of topological defects [27], [28], [29], [30] or from vacuum state transitions [26], [31]. As these axions are non-thermal and produced non-relativistically they meet the cold requirement for dark matter. Axions also have no long-range interactions other than gravity, making them attractive candidate particles.

Searches for axionic dark matter have been either in the form of resonating cavity experiments, such as the ADMX experiment [32], or via examination for axion couplings in the sun, the CAST experiment [33]. CAST is oriented around detecting axions of energy $\sim$ a few keV produced in the interior of the sun when photons transform into axions due to electric fields in the solar plasma, with the experiment using a large dipole magnet detector on Earth which could reconvert these axions into detectable X-rays, a method first proposed by Silkivie [26]. Most recent findings from CAST have limited the axion to photon coupling, $g_{a\gamma} \leq 8.8 \cdot 10^{-11}$ GeV^{-1} for axion masses $m_a \leq 0.02$ eV [34]. ADMX, which makes use of the possible resonant transition of axions into microwave photons in the presence of a static magnetic field and tunable electric field, has recently published results ruling out some of the phase space of one of two fundamental invisible axion paradigms between axion masses of 3.3 μeV and 3.53 μeV. ADMX plans upgrades that will enhance its sensitivity to be sensitive to the other invisible-axion paradigm within two years of running [32].

1.3.3 WIMPs

The other favored candidate particle for dark matter is the Weakly Interacting Massive Particles (WIMP), relic particles theorized to have been produced in thermal equilibrium early in the universe. The most compelling arguments for dark matter with a weak-scale cross section, the source of the “Weakly Interacting” in WIMP, is known as the “freeze out” argument, a thermodynamic argument that relates the abundance of particles today to their annihilation cross sections. Following [35], here we only construct the single-parameter freeze out argument, which assumes the WIMP annihilation cross section is not energy dependent, but refer readers to the review by Jungman [35], for the energy dependent annihilation cross-section corrections.

We begin by asking what we would expect if in addition to the standard model particles there could have been produced in the early universe a long-lived, or stable, additional particle, the χ. For such a particle, the equilibrium number density will be:

$$n_\chi^{eq} = \frac{g}{(2\pi)^3} \int f(\boldsymbol{p}) d^3\boldsymbol{p}, \tag{1.3.2}$$

where $f(\boldsymbol{p})$ is either a Fermi-Dirac or Bose-Einstein distribution and g is the X particle's number of internal degrees of freedom. Noting immediately that if $T \ll m_\chi$, as should be expected as the universe expands and cools,

$$n_\chi^{eq} \approx g \left(\frac{m_\chi T}{2\pi}\right)^{\frac{3}{2}} \cdot e^{(-m_\chi/T)}, \tag{1.3.3}$$

and normal Boltzmann suppression is observed. If the χ particle stayed in equilibrium they would be exponentially suppressed today and of no interest, with thermodynamic equilibrium being maintained by the reactions of the form:

$$\chi\overline{\chi} \leftrightharpoons l\bar{l}, \tag{1.3.4}$$

where the $l\bar{l}$ could be quark-antiquark or lepton-antilepton pairs. As the universe cools, the rate of production of χ pairs is suppressed, but it is the annihilation reaction which sets the scale for freeze out. If the χ particles become rare enough such that, $n_\chi\langle\sigma_A v\rangle = H$, where n_χ is the number density of the χ's, σ_A is the annihilation cross section, and v is the relative velocity, the annihilation process turns off and the χ fall out of equilibrium, freezing out and forming a relic population.

Quantitatively, we use the fact that barring entropy-producing phenomena, the entropy per comoving volume is constant [35]:

$$\left(\frac{n_\chi}{s}\right)_f = \left(\frac{n_\chi}{s}\right)_0, \tag{1.3.5}$$

where s is the comoving entropy density, with subscripts f and 0 representing at the time of freeze out and today, respectively. Solving under the assumption of radiation domination $H(T) = 1.66\, g_r^{1/2}\, T^2/m_P$, with g_r the number of relativistic degrees of freedom and m_P the Planck mass and using the comoving entropy density, $s \sim 0.4 g_r T^3$ [35] with our freeze out condition $n_\chi \langle \sigma_A v \rangle = H$:

$$\left(\frac{n_\chi}{s}\right)_f = \frac{H}{m_P(0.4 g_r^{1/2} T^3)\langle \sigma_A v \rangle} \sim \frac{4}{m_P g_r^{1/2} \langle \sigma_A v \rangle} \cdot \frac{1}{T}. \tag{1.3.6}$$

Converting from $1/T$ to the mass of the χ, m_χ using $T \sim m_\chi/20$ [35], and combining with equation 1.3.5 we arrive at:

$$\left(\frac{n_\chi}{s}\right)_0 \sim \frac{100}{m_P m_\chi g_r^{1/2} \langle \sigma_A v \rangle}. \tag{1.3.7}$$

Using the current entropy density and rewriting in terms of the critical density we find:

$$\Omega_\chi h^2 = \frac{m_\chi n_\chi h^2}{\rho_c} \approx \frac{3 \cdot 10^{-27}\,\mathrm{cm}^3\mathrm{s}^{-1}}{\langle \sigma_A v \rangle}. \tag{1.3.8}$$

From equation (1.3.8) if we take a weak-scale cross section, $\langle \sigma_A v \rangle \approx 3 \cdot 10^{-26}\,\mathrm{cm}^3\mathrm{s}^{-1}$, a particle such as the χ will have a relic density today of $\Omega_\chi h^2 \approx 0.1$, very close to the measured dark matter concentration in the universe, with $\Omega_{DM} h^2 = 0.12029$ [15], we find natural dark matter candidates using just thermodynamical arguments.

None of this line of reasoning tells us the identity of the χ, with candidates being model dependent. Currently favored candidates are the lightest super-symmetric partners arising in super-symmetry extensions to the standard model [35].

Though a large body of evidence has accumulated that the majority of the matter in our universe is dark, and several candidates have been proposed, no direct laboratory detection of dark matter has been made. It is this laboratory search for signals from dark matter that we turn to in the next chapter, examining various ways that experimenters search for the faint traces resulting from WIMP dark matter, either astrophysical, in colliders, or through direct detection of extremely rare interactions between WIMPs and standard model particles.

Chapter 2

WIMP Dark Matter Searches

The search for WIMP dark matter is divided into three types of experimental approaches: looking for dark matter through observation of its annihilation remnants, in astrophysical objects; the generation of WIMP/anti-WIMP pairs inside a collider such as the Large Hadron Collider, detected through missing energy; and the observation of interactions between WIMPs and Standard Model particles.

Searches for remnants of dark matter annihilations, either in the form of excess positron or gamma-ray flux show excess positron flux above 10 GeV [36], [37], but no observed line-features or significant diffuse flux seen in the gamma-ray results of Fermi-LAT are seen [38]. Observations of this type are limited by difficulties in modeling astrophysical backgrounds, so without a “smoking gun,” such as observing a mono-energetic line through multiple sources, these searches are seen as complementary evidence to other methods of WIMP detection such as collider or the “rare-event” interaction with Standard Model searches [39].

The search for WIMP production in colliders is the search for possible pair-production of WIMP/anti-WIMP pairs. As the WIMPs will leave the detector without interaction, these searches are performed through examination of well reconstructed events with missing-transverse momentum. Observation of a class of events of this type would allow for a direct determination of the WIMP mass, as the missing energy would be greater than twice this mass, and would constrain the WIMP cross-section, assuming the production and interaction cross-sections for the WIMP are the same. Searches of this kind have been performed at the Large Hadron Collider at CERN, through examination of events with hadronically decaying W and Z bosons, with no WIMP production observed [40]. While these results are not competitive when compared to the rare-event searches in the spin-independent model of WIMP interaction, they set leading results on spin-dependent WIMP couplings and will continue to gain sensitivity with increased integrated luminosity.

For the rest of this chapter we focus on the third type of WIMP search, direct laboratory observation of WIMP interactions with a target medium. We begin by reviewing the expected WIMP signal given our knowledge of the local dark matter halo before examining the major hurdle to the observation of this signal, radioactive background events. We review techniques of background rejection including detectors with the ability to discriminate between nuclear and electron recoils, the leading class of detectors in use today. As a conclusion to this chapter we examine the dual-phase liquid-gas noble-element time-projection chamber (TPC), a class of technology leading the laboratory search for WIMPs today. In the next chapter we examine a specific dark matter detector, the Large Underground Xenon experiment, a dual-phase TPC and the basis of this dissertation.

2.1 The WIMP signal

Of obvious importance in the search for a WIMP is a model for what the signal looks like, the WIMP recoil spectrum. Following the seminal treatment by Lewin and Smith [41], we derive the expected differential recoil spectrum as a function of the mass of the target, M_T, the mass of the WIMP, M_χ, the local distribution of WIMP velocities, and a nuclear form factor, F, for which we will take the Helm form factor [42].

We begin by writing the differential distribution of WIMP densities about the target,

$$dn = \frac{n_0}{k} f\left(\boldsymbol{v}, \boldsymbol{v_E}\right) d^3\boldsymbol{v}, \tag{2.1.1}$$

where n_0 is the mean WIMP number density, k is a normalization factor, $\boldsymbol{v}$ is the velocity of the WIMP relative to the target, $\boldsymbol{v_E}$ the velocity of the Earth with respect to the dark matter halo, and we interpret dn to then be the density of WIMP particles around our target with relative velocities within $d^3\boldsymbol{v}$ of $\boldsymbol{v}$. For our WIMP velocity distribution, $f\left(\boldsymbol{v}, \boldsymbol{v_E}\right)$, we take

$$f\left(\boldsymbol{v}, \boldsymbol{v_E}\right) = e^{\left(-v+v_E\right)^2/v_0^2}, \tag{2.1.2}$$

a Maxwellian distribution selected as we treat the dark matter halo as an ideal, non-interacting, gas. Here v_0 is the modal velocity of the WIMP distribution. As there is a finite escape velocity for the galaxy, we must truncate our velocity distribution at $|\boldsymbol{v} + \boldsymbol{v_E}| = v_{esc}$, thus forcing the normalization factor,

$$k = \left(\pi v_0^2\right)^{3/2} \left[\mathrm{erf}\left(\frac{v_{esc}}{v_0}\right) - \frac{2}{\pi^{1/2}} \frac{v_{esc}}{v_0}\, e^{-v_{esc}^2/v_0^2}\right]. \tag{2.1.3}$$

For the event rate on our target, per unit mass, we take

$$dR = \frac{N_0}{A} \sigma_T v dn, \tag{2.1.4}$$

where $N_0 = 6.02 \cdot 10^{26}$, Avagadro's number, A is the atomic mass of the nucleus, σ_T is the cross section per nucleus as a function of momentum transfer, and dn comes from equation (2.1.1).

To translate this to an event rate with respect to energy we take the simple model of isotropic scattering in the center-of-mass frame,

$$E_R = \frac{1}{2} M_\chi v^2 \cdot \frac{2 M_\chi M_T}{\left(M_\chi + M_T\right)^2} \left(1 - \cos\theta\right), \tag{2.1.5}$$

with E_R being the recoil energy in the lab frame and θ being the scattering angle measured in the center-of-mass frame. As we are assuming the scattering to be isotropic, corresponding to a distribution that is uniform in $\cos\theta$, we expect our recoil energy to be uniformly distributed over the range $0 \leq E_R \leq E_{R,max}$, with:

$$E_{R,max} = \frac{1}{2} M_\chi v^2 \cdot \frac{4 M_\chi M_T}{\left(M_\chi + M_T\right)^2} \,. \tag{2.1.6}$$

This in turn leads to the formulation of the event rate per unit energy:

$$\frac{dR}{dE_R} = \int_{v_{min}}^{v_{max}} \frac{v_0^2}{v^2} \cdot dR(v), \tag{2.1.7}$$

which we combine with our previously defined quantities to get the numerically useful form:

$$\frac{dR}{dE_R} = \frac{\left(M_T + M_\chi\right)^2}{2 M_T^2 M_\chi^2} \frac{\rho_0}{M_\chi} \frac{\sigma_T}{k} \int d^3\boldsymbol{v} \frac{\Theta\left(v_{esc} - |\boldsymbol{v} + \boldsymbol{v_E}|\right) \Theta\left(E_{R,max} - E_R\right)}{|\boldsymbol{v}|} e^{\frac{-|\boldsymbol{v}+\boldsymbol{v_E}|^2}{v_0^2}} \,. \tag{2.1.8}$$

Here we have made use of the relation between the number density of the WIMPs and their mass density, and the theta functions constrain us to velocities of WIMPs found within the halo that are capable of producing a recoil of energy E_R.

Finally, we express σ_T, conventionally, as a product of σ_T at zero momentum transfer ($q = 0$), the coherent scattering limit in which the WIMP interacts with the entire nucleus, and a nuclear form factor F, which accounts for loss of coherence with increasing momentum transfer:

$$\sigma_T(q) = \sigma_T F^2(q) = A^4 \frac{\left(M_n + M_\chi\right)^2}{\left(A M_n + M_\chi\right)^2} \sigma_n \cdot F^2(q), \tag{2.1.9}$$

where σ_n is the WIMP-nucleon cross-section [41], A the atomic number, and M_n the mass of a nucleon and for which we use the Helm form factor [42] for $F(q)$. Combining this all, and taking the standard estimates for v_{esc}, v_E, and ρ_0 from [41], one can numerically compute the expected recoil spectra for various targets assuming spin-independent interactions, figure (2.1), finding exponentially falling spectra as a function of recoil energy.

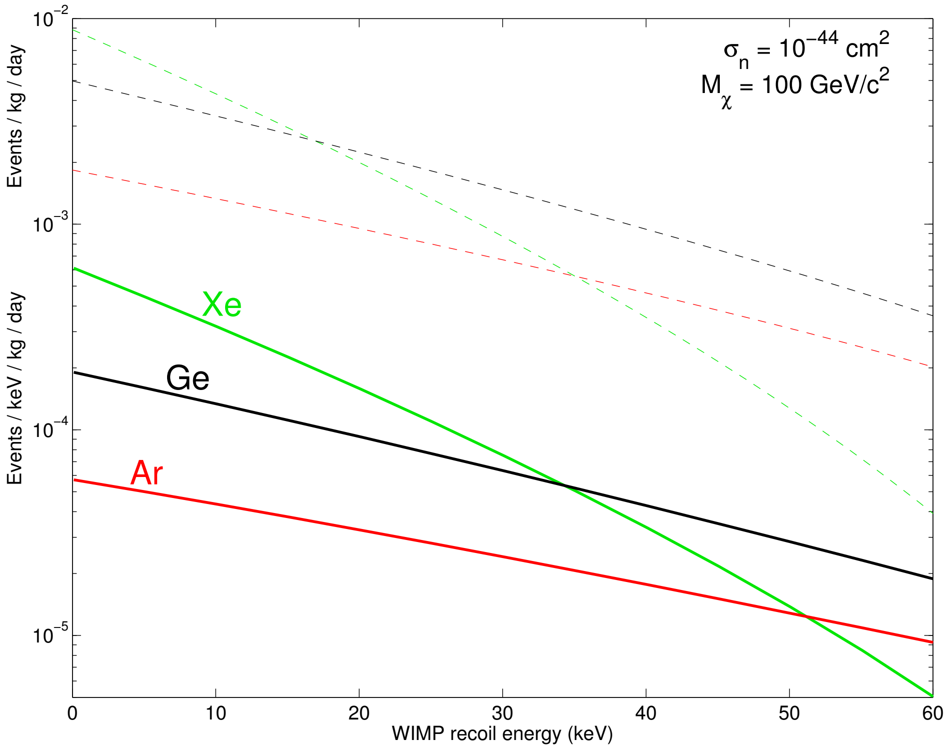

FIGURE 2.1: Expected WIMP differential [solid] and integrated above-threshold [dashed] interaction rates as a function of WIMP recoil energy in xenon [green], germanium [black], and argon [red] for a 100 GeV/c^2 WIMP with a WIMP-nucleon spin-independent cross section of 10^{-44} cm^2. Xenon has the greatest integrated rate, and thus highest sensitivity, for 16.5 keV or lower detection thresholds. The xenon differential rate falls faster than germanium or argon as at higher WIMP recoil energies the interaction loses coherence over the large nucleus. Here no annual modulation of the modal WIMP velocity is used.

2.2 Background Mitigation

The main challenge to detecting any possible signal due to WIMP events is the mitigation of background events. Mitigation of cosmic ray induced backgrounds is accomplished by choice of experiment location, with several underground laboratories around the world in use: Gran Sasso in Italy, SNOLAB in Canada, and SURF in the United States. Other radioactive backgrounds can be suppressed through material selection in detector construction but some backgrounds are can't be fully eliminated, requiring background discrimination based on differential response in the detector measurements. The most successful direct dark matter searches use a combination of all three approaches to background rejection to limit the often many orders of magnitude greater rate of interactions due to background compared to rates expected from WIMP interactions. In this section we briefly review background sources before moving on to currently-used background-mitigation techniques for dark matter searches.

2.2.1 Background Sources

Sources of backgrounds for a WIMP search can originate both from outside and inside the detector. Backgrounds from outside the detector result from particles penetrating into the target, while backgrounds from the detector, can arise from the surfaces and materials used in construction, or even from sources intrinsic to the detector media itself, such as long-lived radio-isotopes. While external backgrounds, such as high energy gammas and neutrons are mitigated with shielding and choice of materials, background internal to the detector and the target media are harder to mitigate.

Backgrounds from the detector or its media can be both high energy or low energy, short-range, radiation. In a detector with calorimetry, high energy backgrounds are not a problem due to the difference in energy as compared to expected WIMP signals, but care must be taken where events from these backgrounds can “leak” to lower energy due to misconstruction or physical effects. Lower energy backgrounds arise from electron capture decays and resulting x-rays, internal conversion electrons, alphas and associated (α,n) reactions, and beta decays. Decays in which a beta is produced with no associated gamma ray, which would otherwise allow for relatively easy tagging as either a multiple scatter or outside the WIMP energy range, known as “naked” betas, can create significant backgrounds to WIMP signal. These naked decays generally result from decays to the ground state of stable nuclei, hence the absence of an associated gamma, but can also be imitated by events near the edges of the detector where an associated gamma ray from the decay can escape the actively monitored volume.

After all methods of background reduction have been exhausted, through material selection and screening, detector media purification, and detector shielding and location choice, remaining backgrounds must be rejected from being WIMP candidate events. The most successful techniques are the use of self-shielding, use of expected annual-modulation of the WIMP signal, and identification of recoil type. Recoil discrimination is useful because differences between nuclear recoils, such as those expected from a WIMP, and electron recoils resulting from backgrounds, allow for another handle in background identification.

2.2.2 Self-Shielding

Some classes of detectors possess what is termed “self-shielding,” the ability to use the outer part of the active detector as an additional layer of shielding and thus cut to some radioactively quieter inner volume of the detector through the use of reconstructed event position. This effect can lead to powerful reductions in background event rate even after material selection. Figure (2.2) shows the level of additional shielding achieved in the fiducial volume of the LUX detector due to the use of the outer layers of xenon acting as shielding for the inner layers.

Self-shielding is particularly effective in WIMP searches due to the extremely low cross-section for WIMP interactions. WIMPs will not scatter multiple times inside the detector, while backgrounds such as γ-rays or neutrons have an extremely low probability of passing through the center of the detector with only a single scatter.

This can be approximated analytically, under the assumption that an incident particle continues traveling in the same direction and with the same energy after a scatter. We justify this approximation as we will only be interested in scatters in energy ranges likely for WIMP scatters, $E < 10$ keV for electron recoils, orders of magnitude below the average energy, $\langle E \rangle$, of a penetrating gamma or neutron.

Under this approximation, the single scatter rate, R, at any point in the detector is:

$$R = \int d\phi \, d\theta \, sin\,\theta \, \frac{1}{x_0} \cdot e^{-d(\theta,\phi)/x_0} \cdot P_{E<E_0} \int dr A(r,\theta,\phi), \tag{2.2.1}$$

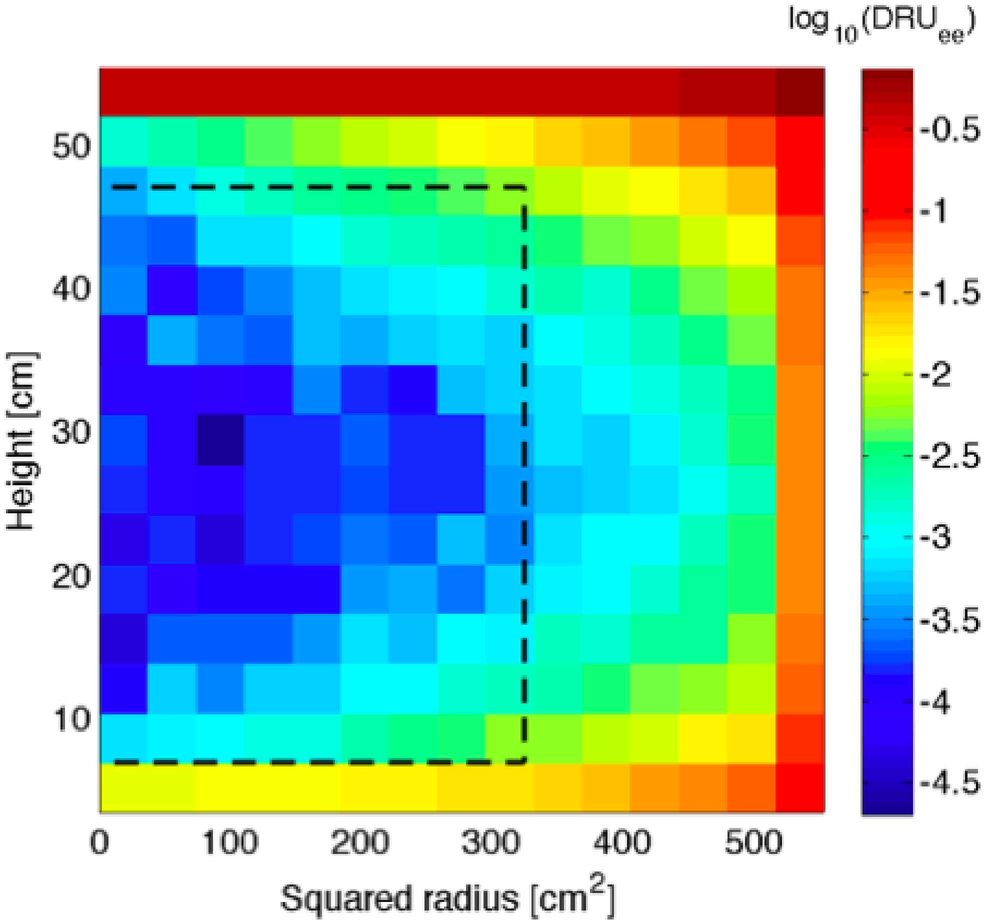

FIGURE 2.2: γ-ray recoil background density in LUX as a function of position. Displayed is the density in DRU$_{ee}$ (cnts/kg/day/keVee) for extrapolated electron recoil events with energies reconstructed between $0.9 - 5.3$ keV energy. Extrapolation is from Monte Carlo fitting to high-energy background events (E $>$ 500 keV electron equivalent). The fiducial volume of the LUX detector taken for the first WIMP result is shown as a black-dashed line. Figure reproduced from [43].

where $1/x_0 \cdot e^{-d(\theta,\phi)/x_0}$ characterizes the probability of a single scatter along path $d(\theta,\phi)$ for a particle of interaction length x_0, $P_{E<E_0}$ represents the probability for a scatter to be in the energy region of interest, and $A(r,\theta,\phi)$ is the expected activity along each path.

The total rate at each point is proportional to the exponential of the ratio of $-d(\theta,\phi)/x_0$, which can be large only when $d(\theta,\phi)$ is small compared to the penetration depth characteristic of the background. This can occur in two limits, near the edges of the detector, where $d(\theta,\phi)$ is small, or for high energy events, for which x_0 is large. While high energy events might seem worrying, they are suppressed by the probability of the single internal scatter being low energy, $P_{E<E_0}$. Thus, the observed event rate in the energy region of interest falls off rapidly from the edges of the detector to its center.

In practice, self-shielding is extremely important for achieving the low background rates required for a WIMP search, offering several orders of magnitude reduction in event rate in a detector the size of the LUX detector. However, self-shielding only lowers the event rate for penetrating backgrounds such as from detector components, but does not assist in the reduction of backgrounds uniform in the detector volume, such as beta emissions from ^{39}Ar in argon based dark matter detectors, ^{222}Rn from air contamination, or ^{85}Kr present residually in xenon.

2.2.3 Annual Modulation

One possible difference between a WIMP signal and more common backgrounds is the time structure expected for each signal. If an experiment runs for a long enough period, annual modulation in the WIMP signal is expected due to directional effects between the rotation of the earth about the sun and the sun about the galactic center. Simple halo models, such as the Standard Isothermal Halo Model, predict a O(1-10)% variation in the observed WIMP flux due to this effect [44]. The seminal measurement of possible annual modulation is the DAMA/LIBRE experiment, with a $\sim 9\,\sigma$ observation of annual modulation [45]; however these results are in tension with non-detection from more sensitive experiments [46],[47]. A significant difficulty of this method is showing that backgrounds do not show annual modulation due to the large number of systematics related to seasonal phenomena.

2.2.4 Nuclear Recoil Discrimination

The third major method used for background rejection is nuclear recoil discrimination. Here methods are employed by various classes of detectors to distinguish between interactions in the target resulting from interactions with the electrons of the target atoms (electron recoils) and interactions with the target atom nuclei (nuclear recoils). While this technique does not reduce nuclear recoil backgrounds, such as those resulting from elastic scattering of neutrons produced in either cosmic ray muon interactions or alpha-n reactions, it does allow for background rejection against naked betas and gamma rays. As nuclear recoil backgrounds resulting from U/Th activity are several orders of magnitude lower than associated Compton scatter backgrounds, these methods can provide a powerful additional level of background discrimination and are used by many of the leading dark matter searches. We refer to the ability to distinguish nuclear recoils from electron recoils as discrimination, and inversely refer to leakage fraction as the fraction of electron recoil events that are mis-reconstructed as nuclear recoils, and thus WIMP candidates.

2.2.4.1 Cryogenic detectors

A series of experiments based around cryogenic detectors, with $T < 100$ mK, use signal read out in two channels: phonons/thermal and either charge from ionization, such as used by CDMS [48], or scintillation such as used by CRESST-II [49]. Discrimination power in this class of detectors arises from nuclear recoils producing only one fourth the electronic excitation of electron recoils, with the majority of the energy loss being to elastic collisions with other nuclei [50]. (A similar effect occurs in liquid xenon, the Lindhard factor of chapter 5, but is not the source of discrimination in that class of detectors, as discussed in chapter 6).

Several detectors of this type have recently reported possible dark matter detections at low masses, in conflict with results from liquid-noble detectors discussed below. While these results are interesting they unfortunately favor different regions of spin-independent WIMP nucleon cross section [51], [49], [52]. Whether these results are due to detector systematics or more complicated dark matter interaction types, such as those proposed by Haxton [53], has yet to be seen. Currently no single underlying theory for dark matter interactions that explains all known potential signals and exclusion limits has been published.

While scaling to larger mass is often more difficult with this class of detectors, extremely low energy sensitivity may be possible, with demonstrated 170 eV (electron recoil) sensitivity using the method of voltage-assisted Luke-Neganov amplification [54]. This low energy threshold could allow for a search for extremely low-mass WIMPs, well below the possible current thresholds for liquid noble or bubble chamber detectors.

2.2.4.2 Bubble Chambers

Bubble chambers using superheated liquids have shown recent promise as a new technology for WIMP searches. Discrimination power here comes by tuning the pressure and temperature so that electron recoils do not deposit enough energy in a localized track to nucleate a bubble, while maintaining the ability of nuclear recoils to nucleate a bubble that grows until it is observable and the chamber is reset. Examples of detectors of this type are COUPP and PICASSO, and their planned merger, PICO. Detectors of this type demonstrate extremely high discrimination fractions, 1 in 10^{10} from COUPP at a threshold of a 10 keV nuclear recoil [55]. However, a limit of this technology is that no energy calorimetry is possible, outside choosing the set point for bubble nucleation. While historically alpha backgrounds present problems for this technology, recent results from COUPP indicate $> 99.3\%$ α event rejection using a frequency-weighted acoustic-power density calculated through measurement of the sound the bubble formation creates [56]. However, contamination of the first WIMP search result of the 4-kg chamber of COUPP was observed due to additional bubble formation that correlated in time with previous events, limiting WIMP sensitivity. Preliminarily, it is thought these events may be due to particulate contamination inside the chamber, but more work is required to understand and reduce this background [56].

2.2.4.3 Liquid Noble Detectors

This class of detector uses a liquid noble element as the main target, with both single-phase and dual-phase (liquid-gas) detectors currently in use or development. Single-phase detectors, such as DEAP/CLEAN, make use of pulse-shape discrimination in liquid argon and neon to gain discrimination power. As noble liquids produce excimers, excited molecules, in either a single or triplet state, with a shorter and longer life, respectively, discrimination is found due to nuclear recoils relatively higher rate of exciting singlet states. With the different production of excimer states detected through the significant difference in lifetime between the two states in argon and neon [57]. It is the production of these excimers that also results in liquid nobles being transparent to their own scintillation light, an extremely useful property for scintillation-based detectors. With good timing resolution, the pulse shape of the prompt scintillation can then be studied, with nuclear recoils showing a greater fraction of light in the initial samples. Here, a leakage fraction of $< 6 \cdot 10^{-8}$ has been demonstrated in liquid argon between 43 and 86 keV as measured for electron recoils [58]. High discrimination rates are required in liquid argon due to the long-lived radioactive isotope ^{39}Ar, a naked beta emitter, that requires extremely good event rejection, expensive isotopic separation removal, or the mining of underground Ar naturally depleted in ^{39}Ar, to eliminate.

Two-phase liquid-gas noble-element detectors, use the principles of a time-projection chamber. Here a prompt scintillation light and a secondary charge (or scintillation light) signal are observed. This approach allows three dimensional position reconstruction and associated self-shielding, with discrimination coming from the relative rate of producing atomic excitation or ionization [59] at the event site. For this class of detector, xenon is the most commonly used noble [60],[46],[47], due to its lack of long-lived radio-isotopes and high atomic number, useful for enhancement of the expected WIMP signal, though work towards dual-phase argon is also ongoing, [61].

2.3 Dual-Phase Xenon TPCs

A subclass of liquid noble detectors, dual-phase liquid noble time-projection chambers (TPCs) are currently the technology showing the greatest sensitivity and scalability for WIMP searches [62]. Here we focus on liquid xenon, but point to the obvious parallels with other liquid nobles such as argon or neon, beginning with a discussion of the basic interaction physics followed by a summary of event reconstruction and finally a brief discussion of event discrimination.

2.3.1 Interaction Physics

Interactions in liquid xenon can distribute energy down three possible channels: prompt scintillation, ionization at the event site, and heat production, resulting from soft elastic scatters with the xenon nucleus. We expect that this splitting could be both a function of interaction type, be it a nuclear interaction, an electron interaction, an alpha interaction or something more exotic, as well as the amount of energy deposited in the xenon during the interaction itself. In this section we briefly introduce xenon interaction physics, covered in greater detail in chapters 5 and 6.

Figure 2.3 gives a basic schematic representation of the interaction chain in xenon. Incident ionizing radiation gives rise to the production of both ionization and excitation of xenon atoms. While some of the ionization produced electrons escape the event site, the remainder recombine with ionized xenon atoms at the event site, through a process called recombination. Recombining electrons result in a contribution to the production of excited xenon excimers, Xe_2^*, and scintillation light produced as these excimers return to ground-state neutral pairs of xenon atoms. Light at the event site, whether from initial excitation of xenon atoms, or resulting from recombination, produces prompt scintillation. Electrons from the event site are drifted under an applied electric field to the liquid surface where they are either detected via charge readout or extracted into the gas phase and accelerated under a stronger electric field, producing a secondary pulse of electroluminescence [63]. We refer to all prompt scintillation light as S1 signal and all

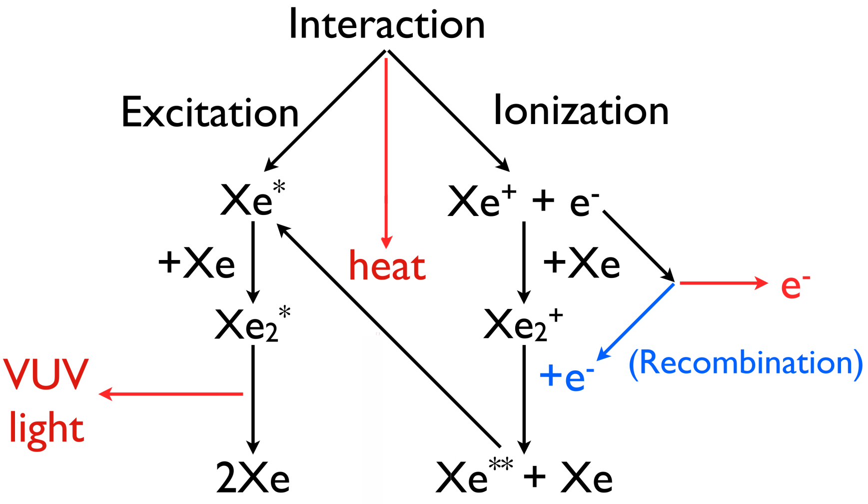

FIGURE 2.3: After a recoil with a xenon atom, deposited energy from the interaction is split along several different paths. Initially the interaction produces a mixture of ionization, excitation, and heat. The ionization branch yields electrons which can either be drifted away from the event site via an applied electric field, or recombined with ionized xenon atoms resulting in a return to the excitation branch, the source of the 178 nm Vacuum Ultraviolet light.

secondary scintillation light, or charge readout, as S2 signal. Figure 2.4 shows a schematic representation of an event in a TPC with secondary light readout.

2.3.2 Interaction Reconstruction

To reconstruct energy, the area in photoelectrons (phe) or charge observed for both the S1 and S2 signals are used, as we describe in chapter 5. Here we obtain two estimates of energy, one for if it was an electronic recoil and one for if it was a nuclear recoil. This dual-energy scale accounts for the much greater fraction

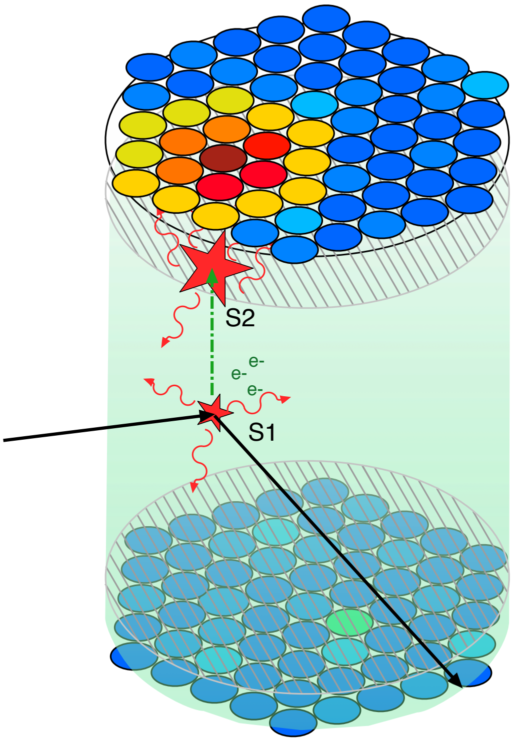

FIGURE 2.4: Event topology in a Xenon TPC. Particle interaction gives rise to prompt scintillation signal (S1) and secondary scintillation signal (S2). S1 light is the result of both nuclear excitation and recombination of initial electrons and ions, while S2 light is the result of those electrons from event site that are drifted to a top extraction region under an applied electric field and undergo scintillation in the gaseous xenon extraction region [63].

of energy lost to heat in nuclear recoils as compared to electron recoils, section (5.1.3).

In LUX, both the S1 and S2 signals are detected by two arrays of photomultiplier tubes (PMTs), one situated at the bottom of the active liquid target region and one at the top above the gaseous S2 generation region. From the time separation between the S1 and the S2, the drift time, we reconstruct the depth of the given interaction. To do this we make use of historical measurements of electron drift velocities as a function of applied field [64] or by observing the drift time associated with a detector feature at known depth, such as the bottom of the active region. It is this use of electron drift time to construct the depth of the interaction from which time-projection chambers derive their name. To reconstruct the two-dimensional lateral position, the localization of the S2 light in the upper PMT array is used, resulting from the localization of the electron cloud from the event site and the geometry of the top PMT array, positioned within a few centimeters of the liquid surface. As all three dimensions can be reconstructed, TPCs give accurate position reconstruction in 3D on an event-by-event level, allowing for the creation of a fiducial volume at the center of the detector.

As the observation of S1 and S2 sets our ability to reconstruct position, energy, and interaction type, the collection and reconstruction of both the S1 and S2 signals for any event is critical in the use of a TPC. For this reason, and reasons discussed further in chapter 6, the selection of materials must be optimized to ensure that reflectivity to 178 nm xenon scintillation light is as high as possible in the active region while maintaining strict limits on both radioactive contaminants and the presence of any chemical contaminants that could affect the S2 size. Reflectivity is achieved through the use of Teflon reflector panels, historically observed to be highly reflective to Vacuum Ultraviolet (VUV) light in liquid xenon, section (3.1). One major hurdle to the development of large-scale detectors (>100 kg) has been the effort required to remove electro-negative impurities, which affect the S2 size as a function of event depth, the removal of which LUX tackled via its use of a xenon circulation system with multiple heat-exchangers, chapter 4.

2.3.3 Nuclear and electron recoil discrimination

To reject background events in a xenon TPC, the logarithm of the ratio of S2 to S1 signal is used, which historically has shown discrimination power between nuclear and electron recoils over the energy range of interest for WIMP interactions [60]. In chapter 6 we will examine what sets this discrimination power as a function of energy, relating it to fluctuations in the signal measurement process and fluctuations at the event site. Making use of the non-linear response of the xenon media with respect to nuclear and electron recoils of different energies, TPCs obtain rejection power of electron recoils at the $> 99\%$ level while maintaining at least 50% nuclear recoil acceptance, figure (2.5).

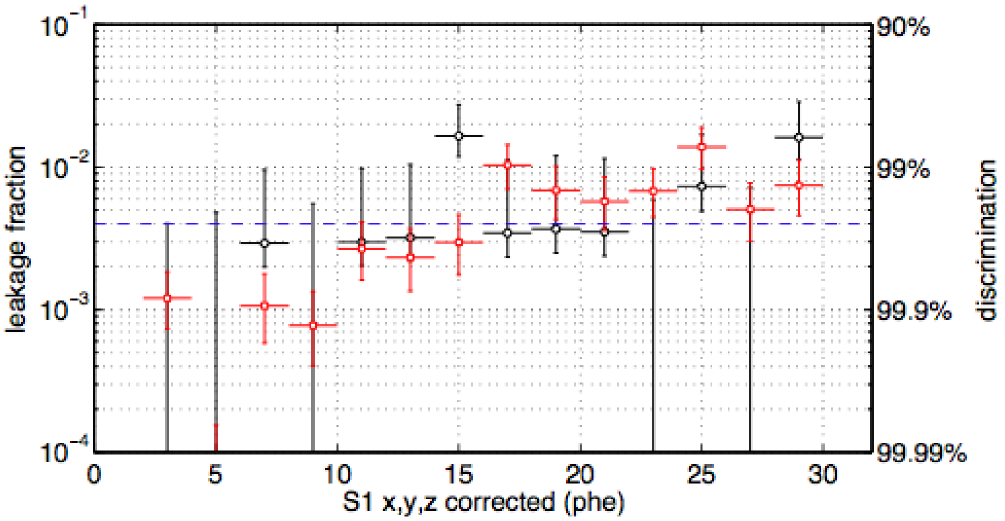

FIGURE 2.5: Leakage fraction (right axis) and discrimination (left axis) measured between electron and nuclear recoil populations as a function of S1 area. All data is at 50% nuclear recoil acceptance as calculated from simulations. Data are from both direct measurement using tritium [black] as well as from Gaussian fits to the electron recoil population [red] and bins with no events show upper limits. Mean discrimination (99.6%) across 2-30 photoelectrons (phe) is shown in dashed-blue. Data was taken at 181 V/cm. Figure reproduced from [47].

It is the combination of 3D position reconstruction;,strong self-shielding, nuclear and electron recoil discrimination, the ability to look for annual modulation, and the ability to select targets with low or no radioactive backgrounds that make xenon TPCs the world's leading dark matter searches. As scaling of this class of detector involves building larger containers to hold larger target masses, and self-shielding means the fiducial volume grows faster than simply scaling with volume, TPCs are expected to remain the most sensitive detectors for the next generation of experiments. The future of the TPC may well depend on whether high discrimination fractions can be obtained, with the general consensus from experimental data being the need for better light collection and higher applied electric fields in the xenon target region [65].

In the next chapter we move to an examination of the design of the Large Underground Xenon (LUX) experiment, a dual-phase liquid xenon TPC of the class just described. We focus on the physical design before moving to detector performance in chapter 4. We then discuss the energy reconstruction used, chapter 5, and go on to examine fundamental event level variations, chapter 6, which allow us to understand the discrimination power described above in greater detail. Having completed these studies, outlining methods for use in future runs of LUX and other experiments, we finish with an examination of the first WIMP search results from the LUX experiment.

Chapter 3

The LUX Detector

The LUX 1.0 detector currently holds the "world-leading" dark matter limit, the result of careful design work to create a detector finely tuned for looking for rare low-energy interactions while maintaining stable operational conditions on the timescales of years. This chapter introduces the LUX detector, also referred to historically as LUX 1.0, providing a picture of its internal structure.

As the successor to the LUX0.1 prototype [66], the LUX detector is a ∼350 kg (∼250 kg active) dual-phase xenon time-projection-chamber (TPC) of the class described in Chapter 2. After depicting the design of the LUX detector here, we move to an examination of the LUX detector performance as related to observed detector stability and the use of a heat exchange system to achieve multi-meter electron drift-lengths essential to a dark matter searches using liquid-noble TPCs.

3.1 The LUX Detector: Physical Structure

Figure (3.1), shows a schematic representation of the LUX detector. the LUX inner cryostat and outer vacuum vessel are made of titanium, screened and selected for its low intrinsic radioactivity [67]. To provide thermal insulation for the cryogenic inner vessel, operating at 173 K during running, an outer vacuum vessel is used. The outer vessel has a volume of ~ 0.87 m^3 and is maintained at pressure $<$

$70 * 10^{-6}$ Torr during running to limit convective heat transfer via a Varian TV-301 navigator turbo-pump backed by a Bluffton Scroll pump. Further thermal insulation is provided by interleaved sheets of super-insulation surrounding the inner cryostat. To ensure thermal uniformity across the space, the outer vacuum vessel is monitored by 23 platinum resistance temperature detectors (RTDs).

The inner cryostat has a volume of ~ 0.36 m^3, excluding the breakout cart and conduits, and houses the internal components and xenon target itself. Surrounding the inner cryostat is a copper shell, to help maintain a uniform thermal profile around the detector, nested inside a plastic shell for further thermal insulation and to slow the boil-off rate in catastrophic failure modes involving water from the water tank entering the outer vacuum jacket. Inside the inner cryostat, suspended via 6 titanium straps from the inner cryostat top flange, are a series of large copper pieces which make up the bulk of the detector structure. From the top down they are the top gamma shield, the top PMT holder, the bottom PMT holder, and the filler-chiller-shield (FCS). These copper pieces form the remaining structure from which the rest of the detector hangs and is supported, as show in figure (3.2).

The active region itself is surrounded by an inner layer of Polytetrafluoroethylene (PTFE) panels used due to its high reflectivity, $> 95\%$ to xenon scintillation light when immersed in liquid xenon [68]. Forming the inner upright-dodecagonal prism of the active region, these PTFE panels are supported by a larger set of outer panels constructed of ultra-high-molecular-weight polyethylene (UHMWPE) which mount directly to the top PMT holder, with a slotted mount to the bottom PMT holder to allow for thermal contraction. Between the two panels, a series of 47 field-shaping copper dodecagon rings are used to ensure electric field uniformity as a function of depth, with the rings being connected through a parallel pair of 1 $G\Omega$ resistors and biased through voltage division from the biases applied to the grids which set the main electric fields inside the detector.

As the application of electric fields while maintaining transparency for scintillation light is essential in the operation of a low-energy threshold dual-phase xenon TPC (2.3), LUX uses a series of wire grids (cathode and gate) and a wire mesh (anode) to apply electric-fields over the drift and extraction regions while blocking the least amount of light. Of these grids, the cathode grid, made of 0.0206 cm ultra-finish

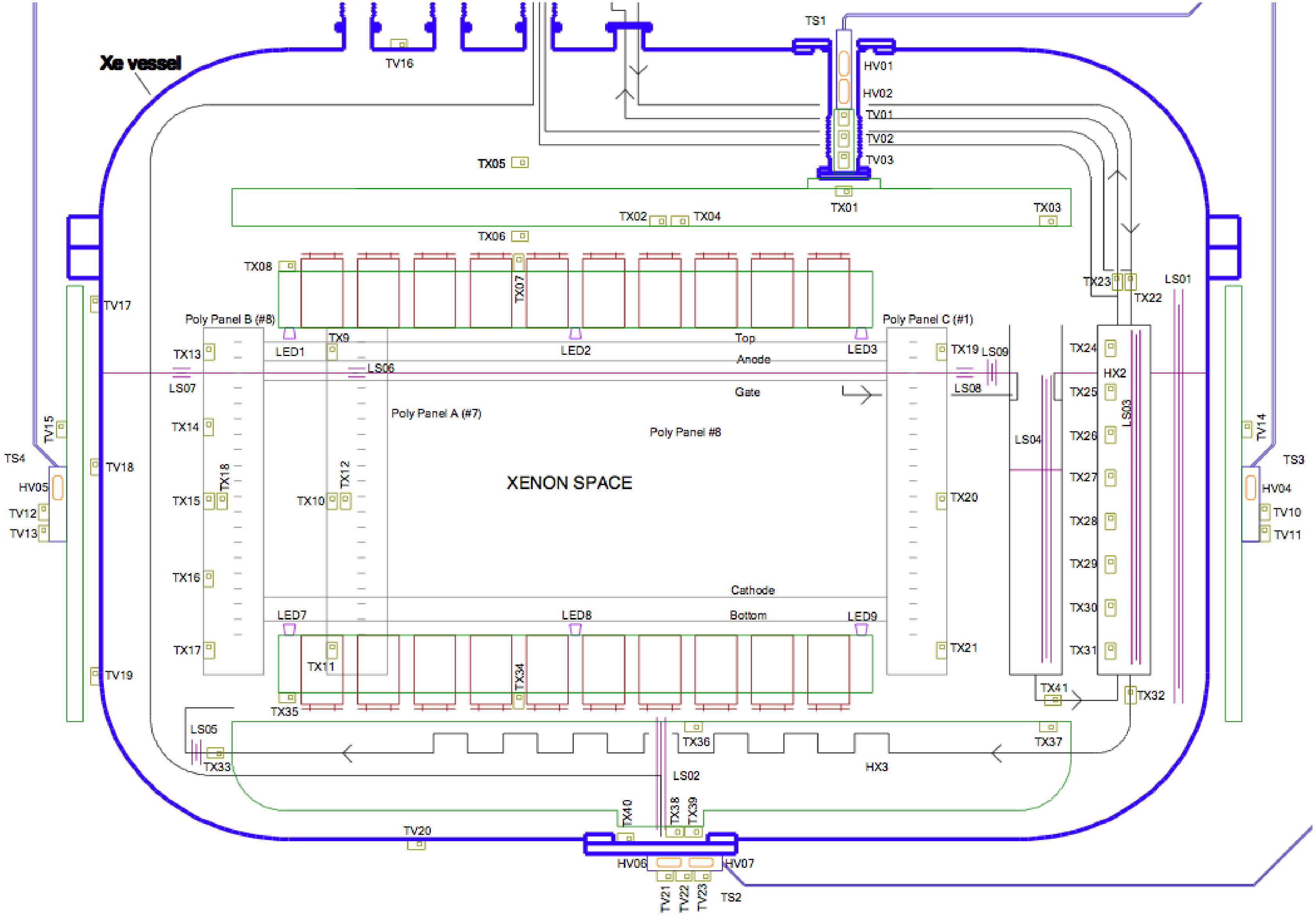

FIGURE 3.1: Schematic diagram of the LUX detector. The diagram portrays the inner cryostat (blue), locations of thermometry (hello) and level sensors (purple) and the grids (gray lines). Copper pieces are displayed as green outlines, and are, from top-to-bottom, the top gamma shield, the top PMT holder, the bottom PMT holder, and the FCS. Also illustrated are the thermosyphon cooling systems (navy), three of the plastic panels (gray) (those instrumented with thermometry), the weir, and HX2 (discussed in detail in chapter 4.

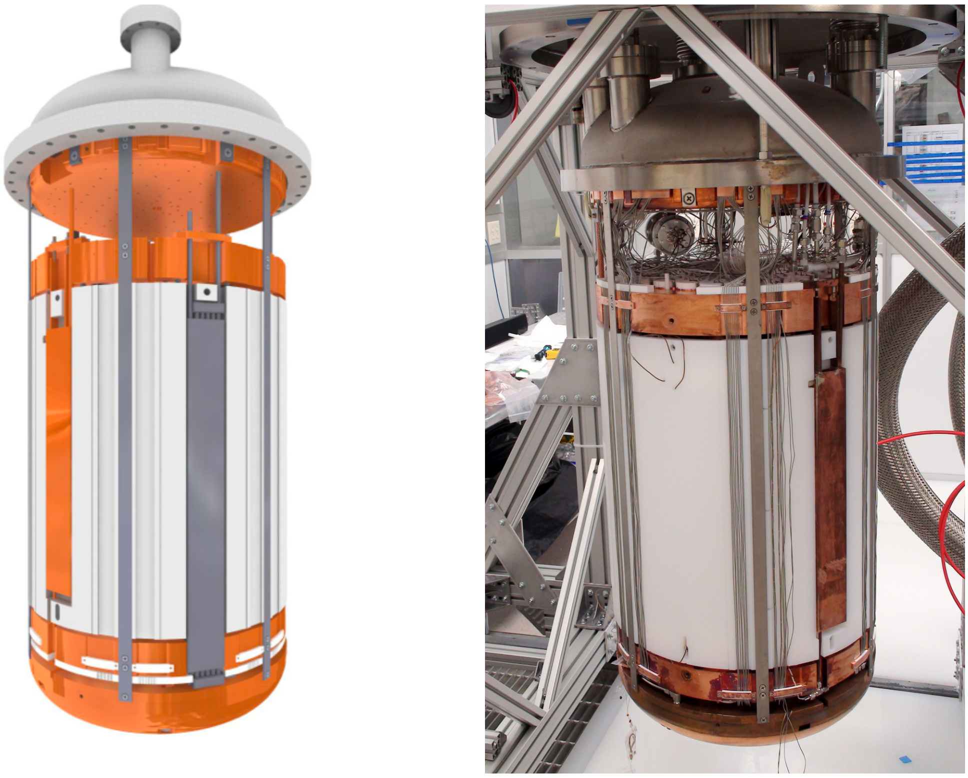

FIGURE 3.2: [Left]: A 3D model of the LUX detector showing the dual-phase heat exchanger discussed in chapter 4, the weir, and the large copper pieces described in the text. [Right]: A photo showing the LUX detector as assembled prior to installation in the inner cryostat vessel. Photograph was taken prior to the beginning of the second run of the LUX experiment.

302 SS wire with a pitch of 0.5 cm, is designed for the greatest applied bias, -100 kV (2.06 kV/cm), but, due to light production observed *in situ* (4.1), is biased to -10 kV (181 kV/cm) during the first science run. The gate grid is constructed of 0.01016 cm 304 SS wire with a pitch of 0.500 cm and situated 48.32 ± 0.34 cm above the cathode and 1 ± 0.1 cm below the anode while cold. The gate grid is biased at -1.5 kV throughout the WIMP search, and the volume between the gate and cathode grids define the active or drift region of the detector, as compared to the extraction region defined by the volume between the gate and anode. The anode, a 316 SS wire mesh with 0.025 cm between wires and wire diameter of 0.003048 cm, is biased to +3.5 kV during running.

In addition to the grids for the application of fields, LUX uses two additional grids, referred to simply as the top grid and bottom grid that shield the respective PMT arrays from encroaching fields in the drift and extraction regions that might affect the PMT response. During operations, such as during the first WIMP search, discussed in chapter 7, the top and bottom grids are biased to -1 kV and -2 kV respectively. With these two grids the full ordering of the grids from the top of the detector to its bottom is: top, anode, gate, cathode, bottom.

The active region of LUX, while cold, is measured as an upright-regular-dodecagon measuring 48.32 ± 0.34 cm vertically between its gate and cathode grids and 47.3 ± 0.1 cm face-to-face between opposite PTFE panels. The liquid xenon level is maintained between the gate and anode by the presence of a liquid spill-over set 4 ± 1 mm above the gate wire plain. The liquid level between the gate and anode is monitored with a set of four capacitive level-sensors, discussed in more detail in section (3.5). To avoid modulation of signal due to thermal fluctuations and to monitor thermal gradients, which could result in structural warping, during the cool down from room temperature to 170 K, the interior of the LUX experiment is also monitored internally by an array of 40 thermometers and 7 pressure sensors.

The complications arising from cabling this instrumentation as well as the the signal readout for the PMTs, and the cables for the grids within the required geometry of the LUX detector, which dictated the detector to be placed in a large water tank for shielding, required a novel system for the "break out" of these cables from the detector volume, the breakout cart. All cables from the inside of the detector emerge via a set of three flexible, 16 foot conduits, which permanently connect the LUX detector to the breakout cart, which couples to the LUX detector during all phases of transport and deployment, providing a mobile platform for all system read-out into the laboratory. A design goal is to minimize inaccessible connectors, a classic failure point, all cables are contiguous from their respective instrument up the sixteen feet and through the breakout cart to the readout location. This design provides several key advantages, including the ability to do the wiring once despite the three runs and subsequent repairs of the LUX detector, but necessitates that the breakout cart be linked to the xenon space of the inner vessel. While the detector volume is cooled to allow condensation of the xenon target, the breakout cart remains at room temperature. To mitigate possible contamination arising from outgassing of the room temperature plastics internal to the breakout cart, a system of four purge flows are used, with flow-rates between 0.25 and 1 standard liter per minute.

3.2 Signal Readout

Event signal readout in LUX is done via one-hundred and twenty-two 5.6 cm diameter Hammamatsu R8778 PMTs. The PMTs have an as measured average quantum efficiency of 33% and collection efficiency of 90% at the 178 nm peak (VUV light) in the xenon scintillation spectrum [69]. The PMTs were arranged into two arrays, with 61 PMTs in an upper array, above the S2 scintillation region, and 61 PMTs below the cathode grid at the bottom of the liquid target. PMTs are read out using Gore coaxial cables which directly connect from the PMT base to the breakout cart readouts.

Once read out, signals are sent through a preamplifier mounted directly on the breakout cart feedthrough before being transmitted to a post-amplifier in the data-acquisition (DAQ) and trigger systems. The DAQ and trigger systems are designed to handle a dynamic range large enough that the limiting factor in LUX is an expected 2% nonlinearity in the PMTs at an instantaneous current draw of 13 mA, $\sim$ 120 keV$_{ee}$, while still maintaining greater than 95% of single photo-electrons (phe) pulses being distinguishablable, at 5σ, from baseline noise fluctuations [70].

The trigger and DAQ system are also designed to perform baseline data suppression, operating in a pulse-only-digitization (POD) mode over the course of the science run discussed in chapter 7. POD mode was designed as a data compression step in which, due to the relative quiet of the LUX detector, only pulses above baseline are saved, while comparatively long periods of recording empty baseline are not. Trigger channels are paired such that either channel going above a valid pulse detect threshold results in both channels being saved, independent of what is recorded by the second channel [70].

3.3 Xenon target

LUX is designed to be filled with $\sim$ 350 kg of xenon, accounting for the total xenon volume in gas and liquid. Actual fill masses, as estimated via the use of the gross weight of the xenon storage bottles and the final internal pressure of the bottles once filling was complete, were 365 ± 3 kg in Run 3 and 368 ± 2 kg in Run 2. Of this $\sim$ 350 kg, $\sim$ 250 kg of xenon were active target, between the cathode and gate grids, where the exact mass in the active region depends on the run temperature and pressure. This $\sim$ 250 kg was estimated based on the known internal volume of the active region while cold and the xenon density as given by the xenon liquid-gas equilibrium curve.

The LUX xenon came from a variety of sources before undergoing an extensive program at Case Western Reserve University (CWRU) to lower its ^{85}Kr concentration. ^{85}Kr is a long-lived radioactive isotope (half-life 10.756 years) present primarily from nuclear fission contamination of the atmosphere and thus present in xenon when it is refined [71]. As ^{85}Kr is a noble dissolved in the xenon, it is not removed by the regular purification system on the LUX detector and, if untreated, would present an intrinsic background, uniform through the active volume. Natural xenon contains 130 ppb gram-per-gram krypton from its production, with the program at CWRU reducing this to a level of 4 ppt gram-per-gram using chromatographic separation [47]. Of this natural krypton we infer a relative concentration of $\sim 2 \cdot 10^{-11}$ is ^{85}Kr from atmospheric measurements of the relative concentration of ^{85}Kr. Reduction of the overall concentration was largely successful, leading to an expected background rate of $0.17 \pm 0.10_{sys}$ counts/keVee/kg/day (DRU) within the LUX fiducial volume over the energy range of interest, 0.9 to 5.3 keV$_{ee}$ (energy scale as discussed in chapter 5) [43].

3.4 Cryogenics

LUX operates cryogenically through the use of a remote dewar containing liquid nitrogen (LN) with cooling power directed to five separate points within the outer vacuum jacket via thermosyphon technology. Though in use extensively in other fields, from engine to computer cooling, [72],[73], LUX is the first to use this technology as a way to deliver stable cryogenic cooling power to a shielded TPC at a distance of several meters [74]. The LUX experiment thermosyphons operate using a passive closed loop system. Once filled beyond atmospheric pressure with dry nitrogen gas, condensation occurs in the upper region, which is in thermal contact with the LN bath. Gravity then forces the condensed nitrogen droplets downwards where, assuming good insulation over the length of transport tube, they come in thermal contact with a copper cooling head coupled to the object to be cooled. Once in contact with the thermal head, the liquid droplets evaporate due to the thermal load of whatever the thermosyphon is attached to, cooling the cold head. This process continues in a cyclic way until either the cooling head and the LN dewar reach thermal equilibrium or nitrogen gas is added or removed to/from the thermosyphon line, adjusting its cooling power.

LUX contains five thermosyphons, two high-power thermosyphons, for maintaining cryogenic stability and cooling the detector from room temperature, are mounted to the top copper gamma shield and bottom FCS, with designation TS1 and TS2, respectively. Both TS1 and TS2 are double-tube thermosyphons, having separate lines line for liquid and gas fluid flows. In addition to TS1 and TS2, LUX has a pair of single-tube thermsyphons, TS3 and TS4, mounted to the copper shield external to the LUX inner cryostat. These two thermosyphons are designed to combat temperature gradients that might develop during operation [75]. Finally, LUX employs a final thermosyphon as a prototype cryogenic pump, installed remotely in the outer vacuum space as a backup in case of turbo or roughing pump failure. Though a thermosyphon at its core, as described above, the cryogenic pump was surrounded by zeolite with an attached heater. Operation consists of a bake-out period at 290 K and then a running period where the head is cooled to 80 K. Once baked-out and cooled the zeolite provides a trapping surface for gas in the vacuum insulation jacket, acting as a pump, with the ability to maintain the cryostat vacuum for $\sim$4 hours during pump failure such as occurred on 11-01-2013, and up to $\sim$4 days during normal operations, figure (3.3).

One discovery with the LUX thermosyphons, made during the LUX0.1 program, is the existence of two operational modes. In the first mode, called the low-power mode, the thermosyphon's response is directly related to the nitrogen mass internal to the thermosyphon. The second mode, called high-power mode, is distinctive as it provides both much larger cooling power than the tunable low-power mode but also losses the tunablilty discussed previously. LUX is primarily operated with the thermosyphons in the low-power mode, with high-power mode being reserved for the condensation of the xenon target. In low-power mode cooling power supplied

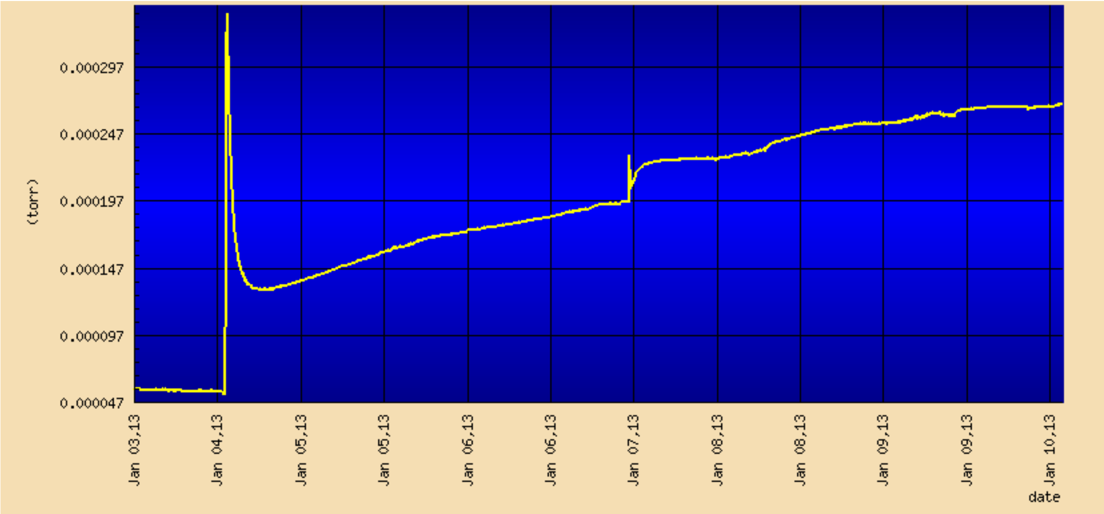

FIGURE 3.3: Outer vessel pressure as a function of time comparing the use of the normal pumping configuration (turbo pump + roughing pump) to the use of the prototype cryopump. The sharp spike on Jan. 4 is the transition from the normal pumping configuration to the cryopump configuration. The cryopump is able to maintain vacuum pressures < 250 μTorr over a period of four days with slowly increasing pressure for the duration of its use. The cryopump is also sensitive to the times of the thermosyphon LN dewar being filled, such as just before Jan. 7. For these reasons the system is used primarily as a backup to the normal pumping configuration, acting as a buffer during power-outages or other failure modes.

via TS1 and TS2 is temperature controlled with a pair of proportional-integral-derivative (PID) heaters coupled to the cold heads. Temperatures of the cold head are monitored by a pair of four-wire thermometers used to regulate any temperature fluctuations.

Figure (3.4) shows the condensation of the xenon target for the LUX experiment prior to run 3 as measured by three parallel-wire level sensors, LS01, LS02, and LS04, described in more detail in the next section. Condensation is completed in ~3 days with previous cool down from room temperature taking a period of nine days, figure (4.3).

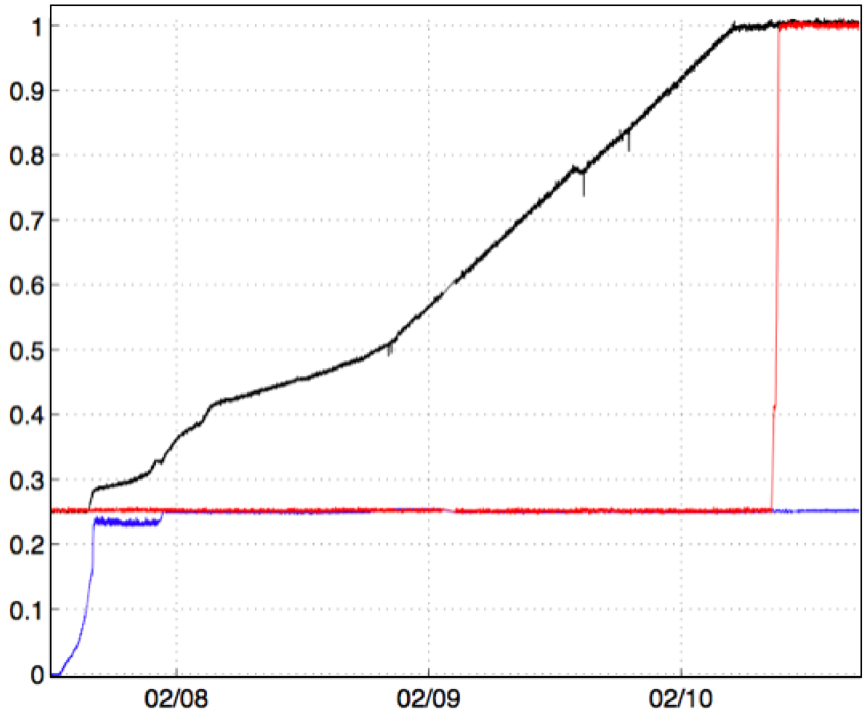

FIGURE 3.4: Normalized liquid xenon level as measured by LS01 [black], LS02 [blue], and LS04 [red], the main active region parallel-wire, the bottom region parallel-wire, and the weir parallel-wire level sensor respectively. Data is presented in a normalized form with 0 corresponding to 1 bar xenon gas, no liquid, and 1 corresponding to full target condensation with liquid at the weir spill-over in the S2 extraction region. Filling is stopped when the weir was observed to respond. The entire xenon payload is estimated to be 365 ± 3 kg. As filling was done at a constant rate, as set by a mass-flow-controller, he changes in slope observed in LS01 correspond to changes in the physical structures surrounding the active region as a function of height.

3.5 LUX instrumentation

As mentioned previously, LUX is instrumented with an array of 63 thermometers (40 internal to the cryostat and 23 external in the vacuum space) as well as 10 pressure sensors (7 internal, 3 vacuum space) and 9 capacitive-liquid-level sensors, all internal to the xenon volume. Thermometers were Omega 100 Ohm platinum resistance-temperature-detectors (RTDs) read-out with three or four phosphor bronze wire leads twisted as either triplets or twisted-pairs, for three and four-wire readout, respectively. Thermometers were readout using ADAM 6015 units.

All wire leads for thermometers were protected along the length of the flexible conduits to the breakout cart by being sheaved with protective virgin-polyethylene tubing. Calibration of thermometers was done prior to installation via emersion in a bath of dry-ice and alcohol and *in situ* via comparison of all thermometer read-outs at room-temperature during stable conditions prior to the beginning of the WIMP search, the later accounting for offsets resulting from the three-wire measurement system of the ADAM 6015 units.

Pressure read-out of the inner cryostat consists of three Ashcroft AST4900 sensors used by the automated recovery system, described in section (3.6), an InstruTech Hornet ion and convection gauge pair for vacuum readout, a Swagelok PGU-50-PC100-L4FSF manual pressure gauge, and a Setra model 759 capacitance manometer customized with range 0-5000 Torr rated at ±0.15% of readout.

Detection of the xenon liquid level in various locations is important both to maintain a stable S2 signal size, section (4.5) and for the monitoring of the long term stability of the xenon-circulation system, section (3.7). Measurement is achieved using two technologies. The first, described previously, are the parallel-plate style capacitors that provide sensitive read-out of any fluctuations in liquid level at the liquid xenon surface. While more sensitive then the parallel-wire design described below, these three sensors experience non-linear effects at their boundaries due to their geometry. The second style of level sensor are in-house-designed parallel-wire capacitive level sensors shielded with metal tubing, figure (3.5). These level sensors were developed as part of the LUX0.1 program, and have linear response over their sensing range. Parallel-wire level sensors are used in six locations in LUX, figure (3.1), to monitor the bath liquid level (LS01, LS02, LS09) and specific components of the xenon circulation system (LS03, LS04, LS05).

All sensors are read out into a unified slow control system. Slow control readout is accomplished using off-the-shelf hardware to convert various signal readouts to ethernet, which are then read into a MySQL database using custom built dæmon code written in C. All dæmons run on a single computer, called the master, located in the underground laboratory which also ran a master dæmon process called the Watchdog. This Watchdog program has sole direct control of which other dæmons are running or terminated based on inputs from users via a front-end system but

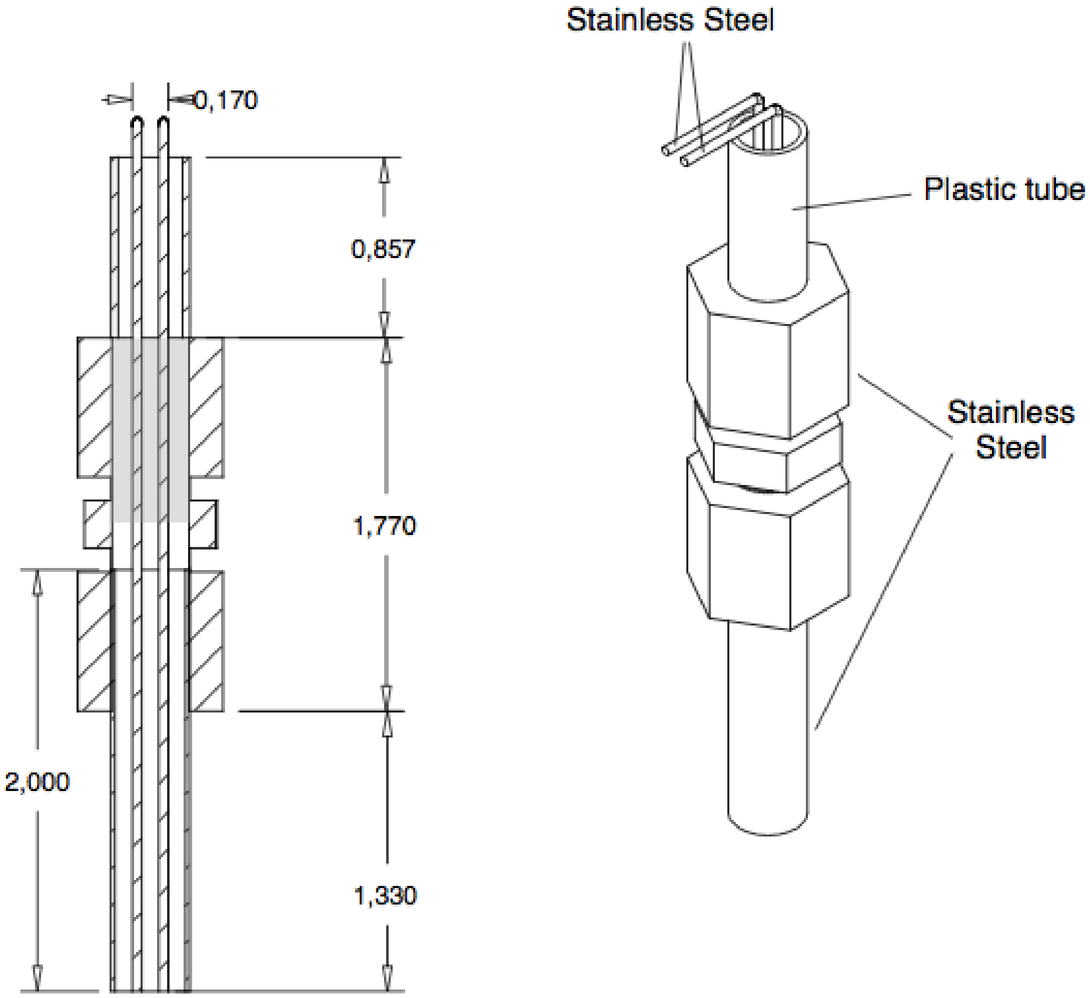

FIGURE 3.5: Design of LS09, a sample parallel wire level sensor, used in the LUX detector to monitor the liquid level in a region around the S2 extraction region (between the gate and anode grids). All labeled dimensions are in inches. Calibration of level sensors is done *in situ* by using known physical heights such as the reading when empty of liquid xenon as compared to the reading when the detector was filled with liquid xenon to the weir spill-over height. Parallel wire level sensors were found to be extremely convenient for their linear capacitance and compact geometry and easily deployed using custom PEEK plugs (shaded gray) designed to fit into Swagelok or VCR fittings.

also responds to required actions from the automated recovery system, discussed below. The slow control is designed to host numerous users at any time, allowing each to examine different sets of instruments over different time periods. The back-end is designed so users could program and use any graphical-user-interface (GUI) in any programming language desired, with the limitation of being able to talk to MySQL via php or other APIs. During the course of the first WIMP search the primary interface is via an html based web-page which allowed direct control of various physical sensor readouts, instruments, and individual sensors attached to each instrument, eg., an Advantech ADAM I/O module and its associated eight thermometers. In addition to physical instruments the slow control system also runs a series of alarm dæmons controling a siren and alarm in the laboratory itself, as well as a text-message based user alert system, and a module for constant communication to a backup watchdog. The second watchdog is located off-site and is in constant contact with the primary watchdog to monitor for network failure.

By design, the slow control framework is written to be extensible and during the course of the first LUX WIMP search showed great flexibility in being adapted to various systems including the sampling system and the krypton removal system.

3.6 The Automated Controlled Recovery System

Early in design it was recognized that prolonged power loss and access loss could result in eventual failure of the LN system and detector warming. In this scenario all safety risk is mitigated by completely passive systems: burst-disks, rated to 45 psig that vent to a Seaman 8130 XR-5 polyester geomembrane inflatable vessel with volume sufficient to store all xenon inventory at room temperature. In addition to this safety system, a secondary system, the automated-controlled-recovery system (ACRS), is the used for both xenon recovery and experimental risk management.

The primary goal of the ACRS is to initiate a controlled recovery of xenon to the storage-and-recovery vessel (SRV), a cryogenic, pressure-rated vessel for long term xenon storage, prior to reaching the burst disk pressure of the safety system described in the previous paragraph. It contains several separate logic loops to handle normal controlled xenon recovery, detector overpressure conditions, power outages, and prolonged network loss. Each loop's basic goal is to push the detector into the situation with the minimal risk, given likely possibilities that could cause one of the previously listed conditions. The ACRS consists of a series of software programs run continuously on a MOXA UC7112+ low-power computer. These modules communicate with the LN system, the detector instrumentation, the circulation mass flow controllers and valves, the thermosyphons, the slow control, and an automated-transfer switch to monitor for laboratory power loss.

The most commonly used mode of the ACRS is normal recovery, often referred to as forced recovery. In this operation an expert user requests, via the slow control front end, that the ACRS recover some of the xenon mass from the LUX detector to the SRV. In this mode the ACRS closes all paths leading into the detector before opening a single, pre-determined, path from the bottom of the detector to the SRV. As the SRV is maintained well below the freezing point of xenon, its pressure, checked before the ACRS triggered, will be significantly lower than the operational range of the LUX detector, resulting in liquid from the detector bottom being extracted into the SRV. This path is chosen to include one of the primary flow mass-flow controllers so flow rate is monitored and controlled. Heat load associated with moving $\sim$ 173 K liquid xenon to room temperature plumbing is mitigated through the use of a heat exchanger to ensure no ice build up on valves. This forced-recovery mode is also triggered if the ACRS detects that the LN stock underground has gone below 30% capacity, the ACRS has detected a laboratory power-outage for a prolonged time period, or if the ACRS is unable to communicate with the slow control database for a continuous period greater than 72 hours.

The second mode of the ACRS is a pressure reduction loop, triggered whenever the ACRS detects a pressure in the detector higher than 30 psig, including during use of the forced-recovery mode. To insulate against sensor failure the ACRS monitors three independent pressure transducers which vote on the detector pressure, protecting against single-point failures. As in the previous mode, the ACRS monitors the SRV pressure to ensure recovery is possible prior to triggering this mode. While the maximum detector pressure to trigger recovery is tunable, 30 psig is a hard-coded upper limit, and the limit used through the duration of the first WIMP search. Pressure reduction is dynamic, triggering to vent excess gas pressure until the pressure is at least 10% below the set trigger pressure prior to returning to the quiescent monitoring mode.

In addition to the primary two modes discussed above, the ACRS features an automated thermosyphon venting logic tree in the case of power loss. This prevents problems that would arise following power-outage and the loss of heater power because the thermosyphons could freeze the xenon target, possibly resulting in damage to delicate internal structures such as the grid wires. This mode is set to trigger after 50 minutes of power-outage to ensure remaining UPS power necessary for all valve triggers.

As one of the primary purposes of the ACRS and its associated hardware is to mitigate risk in the case of a power loss the entire system is insulated via a backup battery drive UPS and fuel-cell combination, specified for a duration of 7-10 days of full ACRS operation after laboratory power loss.

3.7 Xenon circulation and purification

Section (2.3) mentioned the importance of controlling the concentration of electronegative impurities within the liquid xenon volume. To manage this process LUX makes use of a SAES PS4-MT15-R-1 MonoTorr getter to remove non-noble impurities from the xenon. As the getter is a heated zirconium alloy, it requires that the xenon fluid stream be both in the gas phase and, for maximal effectiveness, room temperature.

To handle these constraints LUX continuously circulates the active xenon volume, evaporating outgoing liquid using a circulation pump to push through the getter before condensing it back into the active liquid volume. Liquid was pulled from the top of the active region and returned at the bottom to ensure effective turnover of the xenon. One problem with this system of purification is that in order to purify quickly, and achieve electron drift-lengths greater than 1 meter, continuous xenon turnover is necessary with maximal flow desired. The original design goal was to circulate at greater than 50 standard-liters-per-minute (slpm) gas. However, during system diagnostics it was discovered that the maximal sustainable circulation flow rate is 27 slpm resulting from constraints on the output pressure of the circulation pumps. This 27 slpm flow is further divided between two sources, 25 slpm gas flow from the detector active region via the main circulation path, and the four purge flows described previously. Three of these purges are connected to the long-flexible conduits that connect the breakout cart with the main volume, and the fourth is directly coupled to the tubing used for the plastic thermometry shielding, described in section (3.5). During the run, each of these mass-flow controllers (MFCs) is set between 0.2-0.7 slpm gas flow, pulling gas from the detector.

To manage the heat load resulting from circulation through gas and liquid phases, the LUX detector makes use of a series of heat exchangers, schematically shown in figure (3.6), placing the outgoing liquid/gas stream in thermal contact with the incoming gas/liquid stream. This contact is done to allow heat transfer between the two streams, resulting in efficient heat-exchange and an overall reduction in heat load of 90% as compared to the equivalent heat load at 27 slpm with no heat exchange, section (4.3). Two heat exchangers are used in LUX in succession to ensure maximal heat transfer, as was done in LUX0.1 [66].

The first heat exchanger is made of two concentric tubes spiraled into a coil. This heat exchanger, HX1, is installed in the vacuum jacket, external to the detector, and provides heat exchange between the outgoing cold gas stream and incoming warm gas stream. Internal to the xenon volume, a second heat exchanger, HX2, is used for heat transfer during the phase change of the outgoing liquid and incoming gas. The heat exchangers used in LUX were originally prototyped in the LUX0.1 detector [66], where tests demonstrated efficient heat exchange using a series of parallel condenser tubes, figure (3.7), resulting in a similar design for use in LUX, figure (4.4).

After the two heat exchangers the incoming liquid is routed through a channel in the FCS, providing a location where it can come into full thermal equilibrium before being introduced to the active region. As the FCS is directly coupled to TS2

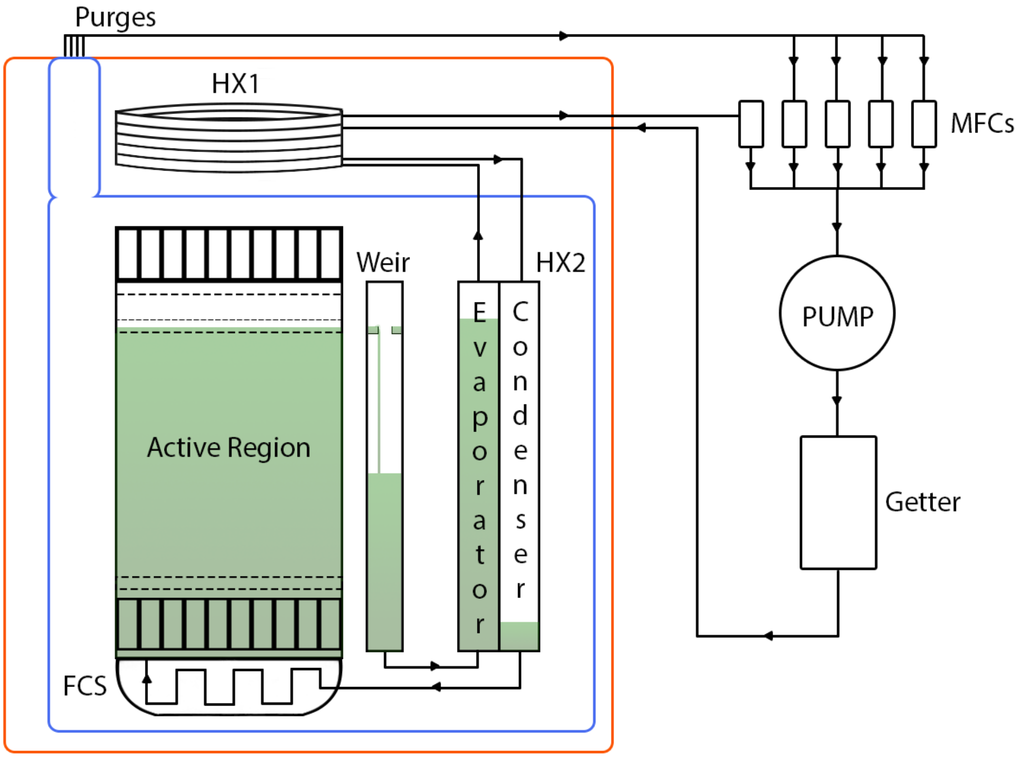

Figure 3.6: Diagram of the LUX circulation system. Liquid xenon (green shaded regions) is drawn from the active region via a spillover in the weir. From the weir, the xenon is drawn into the liquid column of the evaporator due to the pressure difference produced by the pump. Evaporating in a dual-phase heat exchanger, HX2, the xenon gas flows through the plumbing, leaving the inner xenon volume (blue) and entering the vacuum insulated space (red). Here it passes through a gas phase heat exchanger, HX1, before being routed through an MFC into the pump and then the getter for purification. The purified gas is returned to HX1 where it condenses in the condenser side of HX2 before being routed through the FCS at the bottom of the active region and returning to the active region. In addition to this main circulation loop, the LUX detector uses four low-flow purges to mitigate plastic outgassing in the breakout area, illustrated exiting the top of the xenon volume. These purges are controlled with four independent MFCs before mixing with the main fluid stream. Arrows show direction of fluid flow internal to system piping.

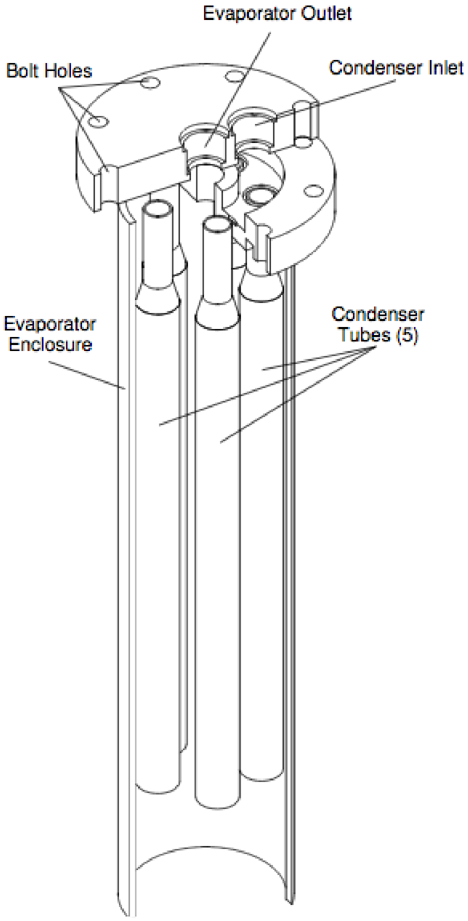

Figure 3.7: Design of the LUX 0.1 dual-phase heat exchanger. The core design consists of multiple tubes for condensation placed inside an evaporator chamber. The evaporator chamber is physically insulated via plastic sheathing from the surrounding bath to encourage heat transfer only between the incoming and outgoing fluid streams. Compare to figure (4.4) to see the evolution of the design for LUX. Reproduced from [66].

this also allows the use of TS2 to mitigate any residual heat load. The circulation system also contains a weir, which directly couples to the top of the active region, setting the active region liquid height via a spill-over. This ensures slow variation of the dynamical system pressure and temperature woll not affect the liquid level seen in the S2 signal generation region. Once liquid spills over the weir lip it enters a separate reservoir space which then feeds directly into the evaporator of HX2.

In addition to measuring electron lifetime directly from data as an indirect measure of impurity concentration, figure (4.9), the LUX experiment also makes use of an online gas sampling system, section 3.8, capable of independently measuring concentrations of nitrogen, hydrogen, argon, oxygen, and krypton, to measure *in situ* impurity concentrations in four locations in the circulation system.

3.8 Online Sampling System

The online sampling system provides a real-time measurement of impurity concentrations in the gas stream at various points in the circulation system through the use of a residual gas analyzer, a SRS-RGA200. Four locations are chosen based on strategic importance: the detector gas stream from HX2 to the main MFC, the conduit purge from the conduit that housed the PMT cables to the gas system, the gas stream output from the circulation pump prior to input to the getter, and the gas stream output from the getter back to the detector. At each point, sampling is done throughout the run period to examine for air-leaks, pump failure, getter weakening, and both outgoing gas streams from the detector.

In order to separate extremely low concentrations of impurities from the xenon, the sampling system makes use of a cryogenic cold trap to perform distillation. During use, a xenon sample enters the system, is frozen through contact with an LN bath, and then pumped on by an external pump. The frozen xenon at 77 K sets the vapor pressure in the system, 1.8 mbar, while the pumping then draws more volatile impurities from the cold trap to the RGA. This freezing process thus reduces the bulk xenon presence in the sample as compared to the impurity concentration, allowing for greater sensitivity measurements.

While analog scans over all atomic masses between 0.1 and 200 amu are taken, the system is designed to examine the concentrations of nitrogen, oxygen, methane, krypton, hydrogen, helium, and argon in real-time. Calibration is done by routinely sampling off a prepared gas cylinder with a known concentration of the various impurities, except methane. Added after the first WIMP search, methane concentration monitoring is used to monitor residual tritiated methane levels after calibration injections [47]. Like all other instrumentation, sampling data is output to the LUX slow control MySQL database for correlation studies with other effects, such as detector temperature, pressure, and electron-lifetime.

3.9 Liquid nitrogen system

The LN system used in LUX is automated for full underground operation and designed to account for possible loss of underground access or loss of power. It primarily consists of a liquid nitrogen reserve, four 450 liter dewars, and an automated logic system which dispenses LN to various subsystems, such as the thermosyphon LN dewar, the SRV and the sampling system. LN fills for both the thermosyphon LN dewar and the SRV are fully automated based on capacitive level sensor readout, an AMI model 286 liquid level controller for the thermosyphon and a GLK 300 system for the SRV. In addition to automated filling the system maintains the option of a manual interface to initiate or stop a fill from one of three underground control panels. The sampling system is maintained using only the manual fill system at the present time as a safety protocol, requiring underground access to use.

3.10 Water Tank Shield/Veto/Source Deployment System

Surrounding the vacuum insulation vessel, the LUX detector is deployed in an 8 ton cylindrical water tank, with a diameter of 7.6 meters and a height of 6.1 meters. During the initial WIMP search, described here, the water tank was operated only in a passive mode, acting as a large water shield, creating an expected reduction in γ-ray rate from the surrounding cavern rock by a factor of $8 \cdot 10^{-9}$. Water from the tank is circulated and purified to reduce backgrounds from impurities in the water with a maximum acceptable level of U/Th/K impurities in the water being set at 2 ppt/3 ppt/4 ppb, which is about 6 orders of magnitude lower than their concentration in the surrounding rock [75]. Though only used passively in the first WIMP search, the water tank is instrumented with 20 Hammamatsu R7081 PMTs to act as an active veto for muons and other particles during the 300 day-blind WIMP search which will enhance background rejection capabilities.

Suspended in the water, next to the detector are a set of six radioactive-source deployment tubes made of acrylic. Leaks in these source tubes resulted in them being filled with water during the course of the first WIMP search but they are still used for the deployment of external sources for calibration, most importantly ^{137}Cs which we will use for a high energy spectrum of Compton scatters in our examination of fundamental event level fluctuations in chapter 6.

3.11 Conclusion

Having now reviewed the physical structure and design of the LUX detector, we turn in the next chapter to examining aspects of its performance to provide a stable and successful operational platform on which to perform a dark matter search, such as is discussed in chapter 7. Before returning to the WIMP search in chapter 7 however, we will digress to examine energy reconstruction and fundamental event level fluctuations as measured *in situ* in LUX in chapters 5 and 6.

Chapter 4

LUX Heat Exchanger Performance and Detector Stability

This chapter focuses on the performance of the LUX detector platform described in chapter 3 in each of its three completed runs, introducing the heat exchange system which is responsible for continuous cryogenic stability for the DM search discussed in chapters (5), (6), and (7). We begin with an overview of the timeline of the LUX program as divided into the three runs before moving on to details on detector stability, heat exchanger performance, and detector quality control over the course of the WIMP search.

A large part of a prolonged WIMP search, such as the first 118 day WIMP search with the LUX detector, or the planned 300 day search period, is the maintenance of extremely stable detector conditions, resulting in strict performance criteria for the experiment. The LUX experiment met its performance goals in several ways. At the most basic level these consisted of having long-term reliable subsystems with available backups as well as pre-emptive plans for problems that arose, as described in 3. In addition, detailed online measurements are performed for a large number of sensors internal and external to the xenon volume, section (3.5), to facilitate proactive responses to developing problems via the slow-control system. The final stage in this process is post-search corrections and cutting based on examination of all relevant slow-control parameters combined with *in situ* real-time measurement of detector response and event reconstruction over the course of the WIMP search.

4.1 LUX Timeline

As of the time of this writing, LUX has performed three major "runs", a loose term, describing physically distinct periods of detector activity, often following a return to room temperature and/or *in situ* upgrades. LUX plans a fourth run, a 300 day WIMP search set to complete in 2014/2015, after a planned series of calibrations and high-voltage tests. This section identifies the timeline of each run along with major milestones achieved and problems discovered and resolved.

4.1.1 Run 1 - Initial cryogenic test

The first run of LUX lasted between May 12^{th} and June 2^{nd}, 2011. The run was performed on the surface, with the primary goal of a cryogenic test. Only one sextant of PMTs were used to test PMT response to thermal stress. No Xenon was used due to a leak identified between the inner cryostat and its vacuum jacket at the bottom thermosyphon cold head identified late in construction. The cryostat was filled instead with 653.2 Torr (stp) of argon/nitrogen mixture, 10% N2/Ar, chosen both for scintillation purposes and limited to less than 1 bar absolute as full pressure testing of the assembled system had yet to commence. No gas circulation was used.

Run 1 identified several early stage problems in LUX, related to the assembly process and provided early input on subsystem improvements needed. Run 1 also allowed for the first *in situ* examination of the Radon-222 levels within the internal structure.

4.1.2 Run 2 - Surface running and system checkout

The second run, a full cryogenic run with all components installed and a full xenon payload of 370 kg, was carried out on the surface between September 1^{st}, 2011 and February 14^{th}, 2012. Run goals included full checkout of all subsystems prior to transport to the underground laboratory. Xenon circulation was tested in this run through a variety of modes, leading to the identification and diagnosis of a break in the xenon plumbing, internal to the detector volume, figure (4.1). This break was discovered during condensation when the condenser side of the dual-phase heat exchanger did not empty despite significant flow-rates. Combined with a flow impedance from the gas-phase heat exchanger, this break resulted in much slower purification of the xenon target then desired.

To achieve desired electron mean-free paths in the active region, a special form of circulation was used in which xenon was pulled directly from the bottom of the detector instead of via the normal circulation loop described in section (3.7). This allowed for faster purification by bypassing the gas-phase heat exchanger, but displayed interesting behavior such as the development of discontinuous electron lifetime as a function of depth, figure (4.2).

Run 2 measured the excellent light collection of the LUX detector, finding 8.4 photoelectrons per keV for 662 keV electron recoils from ^{137}Cs at zero applied electric field, as measured in the center of the active region. Run 2 was also the first observation of the electroluminescent phenomena emanating from the cathode grid when biased past -10 kV, resulting in running at a much lower field 62 V/cm during this run [76]. This problem was improved in the first WIMP search by replacing the cathode grid after Run 2 as described in the next section.

4.1.3 Run 3 - Underground preliminary WIMP search

Run 3 consists of the first unblinded WIMP search period, which includes $\sim$85 live days of data taken between April and August, 2013, as well as cooldown, condensation, calibrations, and xenon purification prior to the start of the WIMP search. This run sets the worlds-leading spin-independent limit on the WIMP-nucleon cross section, chapter 7. All systems performed well with the exception of

FIGURE 4.1: Picture of broken circulation connection due to failed PEEK thermometry mount. Found at the completion of run 2, this broken connection resulted in an inability to test the HX system during the surface campaign. The break was originally noticed during condensation when the condenser volume of HX2 did not empty as the break was directly prior to this volume.

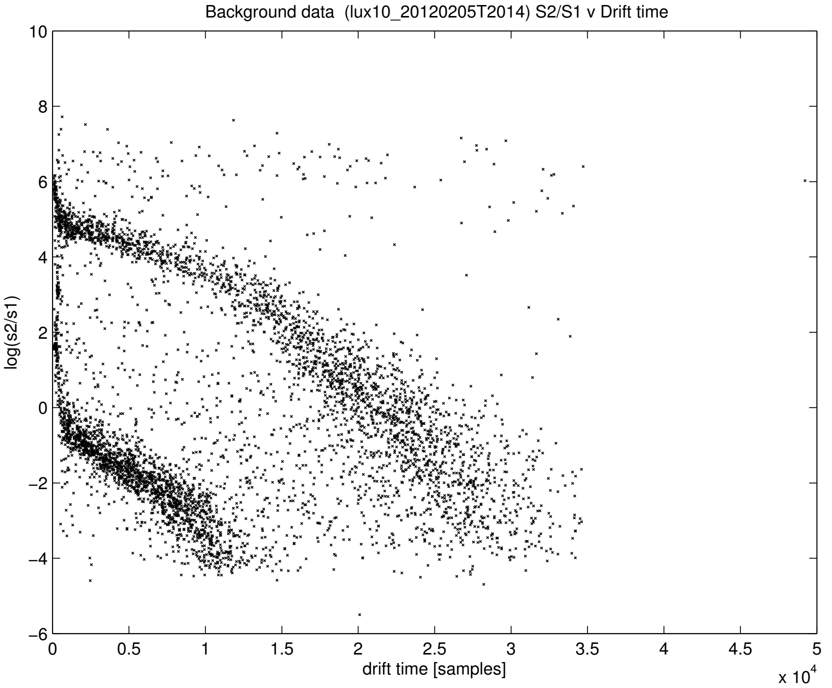

FIGURE 4.2: Log(S2/S1) versus event depth from ^{137}Cs. The x-axis is event drift-time, the time between the S1 and S2 signals, in samples with 1 sample being 10 ns. Two populations can be observed, the upper population is from γ-rays from the cesium source while the lower population is due to alpha events inside the detector. The "kink" in the measured electron lifetime at $1.5 \cdot 10^4$ samples (150 μs) is a result of the unusual flow mode used in Run 2, in which xenon was both removed and returned from near the bottom of the detector, resulting in poor mixing of the active region, as compared to figure (4.8) taken during run 3. The kink was observed to slowly evolve to deeper depths (longer drift times) as purification was continued until establishment of a single electron lifetime across the active region.

the grid high-voltage, with "glow" being observed from both the cathode and gate grids prior to the run and continuing over the course of the run when biased above certain voltages, limiting the possible high voltage, section (3.1). This limited voltage limited the electron extraction efficiency obtainable for events, with the glow being theorized to be due to debris on the grid wires likely produced during construction. Despite these limitation, LUX is able to demonstrate greater than 95% discrimination between electron recoil backgrounds and nuclear recoil events, as discussed in chapter (7).

4.2 LUX Detector Performance and Stability

4.2.1 Cryogenics

As discussed in chapter 3, to support the goal of stable WIMP search running, long term stability in cryogenic performance is required. To reach a state of readiness to begin detector operations the inner cryostat is first cooled to a temperature < 180 K then filled with liquid xenon, pumped in as gas and condensed internally. Cooling of the detector is accomplished using the two high-power thermosyphons at top and bottom of the internals with careful monitoring and adjustment of the thermosyphon power via the addition and removal of dry N2 gas as described in section 3.4.

The cooling rate is set to be slow enough, ~ 0.8 K/hr, to ensure control of thermal gradients is maintained within the specifications given for the plastics to remain free of warping due to differential contraction. This requires control of the vertical temperature profile along the length of the panel to ensure gradients no larger than 10K developed during cool down, condensation, or detector operations. Radial gradients, or gradients between the panel's outer surface and inner surface, with respect to the active region, are also controlled and kept below 5 K. Thermometry is instrumented on three panels, two adjacent to each other, labeled A and B, and one radially opposite across the detector active region, labeled C. Panels A and C are instrumented with three surface thermometers, one near the top, one at the middle and one near the bottom. Panel B is instrumented with five thermometers, three mirroring the positions as described for panels A and C, and two additional thermometers spaced equidistantly between the middle and top/bottom thermometer placements of panels A and C. In addition, two embedded thermometers, mounted via custom UHMWPE mounting screws, penetrate the panels outer surface to a depth of 1.9 cm (0.75 inches), and are placed in the middle of panels A and B for measurement of any developing radial gradients. All temperature sensors were of the type describe in section 3.5. As the internal components of LUX all hang from the top cryostat dome via titanium straps, instrumented panels were selected to ensure both panels with titanium straps (A) and without titanium straps (B and C) are monitored.

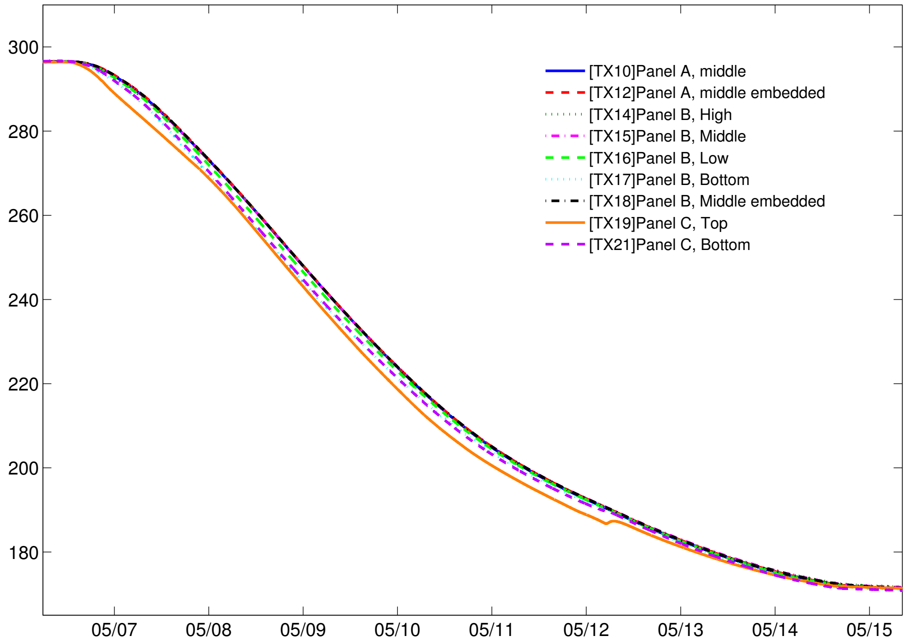

Figure 4.3: Measured temperatures of thermometry in the UHMWPE panels surrounding the active region during cool down prior to run 3. Vertical gradients are well controlled below the desired 5 K vertical spread and radial gradients are well controlled below the 2.5 K upper limit. Cooldown is completed over a period of nine days.

Construction and subsequent running prior to the first underground WIMP search resulted in the loss of the middle thermometer from panel C and the bottom thermometer from panel A, both during movement of the inner cryostat. Figure (4.3) shows data from the panel thermometry during the cool down of the LUX detector prior to Run 3. More conservative bounds of 5K vertically and 2.5K radially were imposed to compensate for lost thermometers vertically and to compensate for the embedded thermometers being at half the radial thickness of the panels, but resulted in no significant reduction in cooling rate.

Following cool down of the internal components condensation of the xenon target is accomplished through the use of the gas system and thermosyphons, TS1 and TS2, in high power mode, over a period of three days. Monitoring of thermal gradients is done at this stage as well, in addition to monitoring of capacitively measured liquid level across the nine level sensors. Figure (3.4) shows the liquid level as monitored during the condensation process, with normalization done between completely empty of liquid xenon and liquid xenon at the level of the weir spillover (full). During the main condensation period a constant mass flow rate is set using the mass-flow controllers, observed changes in slope of the change of the liquid level with respect to time resulting from changes in the detector's inner structure. Further condensation is done past the weir spill over point to partially fill the weir reservoir prior to beginning circulation to avoid emptying the weir reservoir during circulation startup, section 4.3.

4.3 Heat Exchanger System Performance

After condensation, circulation for purification is begun with the detector being monitored for continued thermal stability. As discussed in section (3.7), the large expected heat load from circulation is mitigated via a series of heat exchangers to ensure stability of the internal xenon target.

Figure 4.4 shows the design of the dual-phase heat exchanger used in LUX, based on work from the LUX prototype, [66]. As described in chapter 3, the two-phase heat exchanger, HX2, is designed in a rectangular configuration to match detector space constraints, and constructed from stainless steel to minimize heat transfer from the outer evaporator container to the surrounding liquid xenon bath. Further insulation is done by surrounding HX2 in UHMWPE sheeting prior to installation in the detector. The second heat exchanger, HX1, used for single-phase gas-gas heat exchange, consisting of a pair of concentric tubes, with an inner tube diameter of 3/8" and an outer tube diameter of 5/8", is coiled into a spiral with a total overlap length of 20.3 feet.

Both heat exchangers are instrumented with a set of thermometers, two for incoming fluid streams and two for outgoing fluid streams. Additional thermometry is instrumented on the FCS and the returning liquid stream prior to injection into the active region. Surrounding the active region at various locations, a set of twenty thermometers are used to monitor temperatures of various components and to provide a thermal picture during the heat exchanger characterization process.

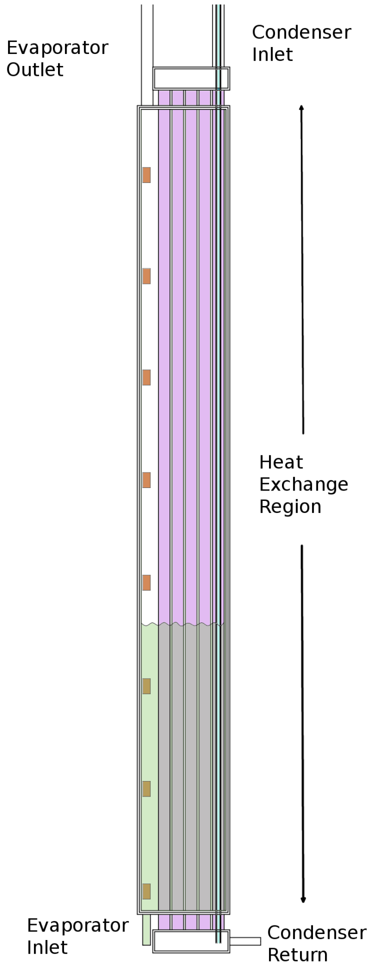

FIGURE 4.4: Dual-phase heat exchanger, HX2. Five parallel tubes for condensation are routed through an external rectangular shell where the outgoing evaporating fluid stream is located. A total of eight thermometers, equally spaced along the vertical dimension of the heat exchanger, are shown as small orange rectangles on the left-hand side. The five condenser tubes are shown to the right of the thermometers. A capacitance level sensor of the parallel wire type is installed, and is shown on the right-hand side of the heat exchanger, but failed during detector cool down, and is un-used in this measurement. Reproduced from [75]

The main goal of characterizing the HX system is to demonstrate efficient heat exchange, creating run conditions with simplified logistics, manageable supply costs, and detector active region stability, limiting bubbling. In this section we describe the calculation of HX system efficiency, which is based on comparing the calculated theoretical heat load, assuming no heat exchange at a given circulation gas flow-rate, to the observed heat load applied to the detector at that flow-rate. Determination of applied heat load is done using a differential method to account for uncertainties in the applied parasitic and thermosyphon cooling power loads on the system.

4.3.1 Applied load estimation

To determine the applied heat load as a function of circulation rate, we note that if the sum of powers on the system is non-zero we expect the temperature of the various components to warm or cool until a steady state is reached,

$$\sum_k P_k = \sum_i C_i(T)\dot{T}_i. \tag{4.3.1}$$

Where k runs over all sources of power into or out of the system, and i runs over all thermal masses of the system, with C_i being the heat capacity of the i^{th} component. In the LUX detector sources and sinks of power are the power load applied via circulation, the parasitic load, the cooling power applied by the thermosyphons, and the heating power provided by the PID controlled 50-W heaters. As equation (4.3.1) requires knowledge of $\dot{T}_i$ for all components, all major thermal masses in LUX are instrumented as summarized in table 4.1.

To compute the specific heats, $C_i(T)$ we use the data available from NIST [77] over the temperature range of interest, figure 4.5.

The parasitic load consists of a term from physical linkages between the detector and room temperature surfaces, the black body radiative power from the surrounding environment, and the power transferred by any residual gas in the outer vacuum insulating jacket. The cooling power is controlled by the amount

Component	**Material type**	**Mass [kg]**	**Thermometers Used**
FCS	OFHC	293.6	TX36,TX33
Top gamma shield	OFHC	121.21	TX01,TX03,TX02
Xenon Can Flange	Titanium	35.30	TV17
Xenon Can	Titanium	88.11	TV19,TV17
Lower PMT Holder	OFHC	169.16	TX34
Upper PMT Holder	OFHC	169.16	TX07,TX08
Field Shapping Rings	OFHC	28.15	TX12,TX18
Structural Panels	UHMWPE	15.5	TX12,'TX14,TX10, TX20,TX17,TX19
Teflon Reflector Panels	HDPE	18	TX12,TX14
Liquid Xenon	Xenon	370	TX06
Copper Radiation Shield	OFHC	59.68	TV14,TV15

TABLE 4.1: Table of detector components, materials, masses, and thermometers used for readout treated in calculation of applied heat-load to determine heat exchanger system efficiency.

of nitrogen gas inside the thermosyphon lines, held constant throughout the measurement period. Heating power is provided by the PID temperature controllers and is directly read out during measurements. Finally, the applied heat load from the circulation of the xenon, which will vary with flow rate, is the parameter of interest.

Taking equation 4.3.1 we obtain the applied power as a function of flow rate:

$$P_{circulation}(f) = \sum_i C_i(T)\dot{T}_i - P_{cooling} - P_{parasitic} - P_{heaters}. \tag{4.3.2}$$

As equation 4.3.1 contains the difficult-to-determine parasitic heat load and applied cooling from the thermosyphons, we employ a differential technique to obtain the applied heat load. Comparing measured heat load at a flow rate to a long duration stability point, taken at zero flow-rate, directly prior to the measurement and assume $\Delta P_{cooling} = \Delta P_{parasitic} = 0$. This second constraint is much easier to enforce then our absolute calibration as variation in parasitic power is only expected from the term related to vacuum jacket pressure, and thermosyphon cooling power variation is only expected with variation in thermosyphon line pressure, both directly monitored and controlled over the full duration of this test.

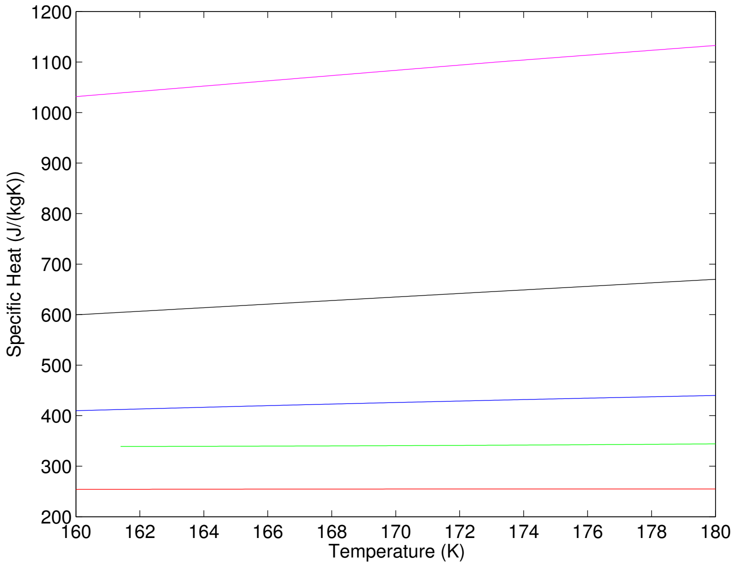

FIGURE 4.5: Specific heat curves used in the calculation of measured heat load versus circulation rate. Data are from NIST [77]. Materials are: OFHC (Red), PTFE (black), Titanium (blue), Liquid Xenon (green), HDPE (magenta). Gaseous xenon is not included as the effect is expected to be negligible based on relative mass compared to liquid xenon.

Using our differential method with these assumptions we simplify equation 4.3.2 to:

$$P_{circulation}(f) = \Delta \sum_i C_i(T)\dot{T}_i(f) - \Delta P_{heaters}, \tag{4.3.3}$$

where all differentials are taken with respect to the previously stated zero-flow stability point. The uncertainty in the thermal profile at zero-flow directly translates into uncertainty in the applied circulation power. This uncertainty is mitigated by allowing for a 3.5 day period of equilibration prior to the start of the measurement, taken between 12:00, Feb-14-2013 and 21:23, Feb-15-2013. For this zero-flow point, and all data taken afterwards, no adjustments are made to the underlying thermosyphon line N2 mass to ensure a system with constant cooling power.

4.3.2 Estimation of expected thermal load

To compute the efficiency of the heat exchange system from the measurements, we examine the expected power load for circulating xenon gas at a flow-rate, f. We start by decomposing the expected load into two terms, the first from the required enthalpy change for the xenon condensation/evaporation process, and the second from the required cooling from room temperature to the measured gas temperature at the inlet of HX2, as monitored by a calibrated RTD directly prior in the flow path to HX2. We state both terms as powers, by factoring in the flow rate:

$$P_{expected} = P_{condensation} + P_{cooling}. \tag{4.3.4}$$

To determine the power load for cooling the gas, we directly apply the molar heat capacity of xenon given the flow rate and change in temperature, ΔT, between room temperature and the temperature as measured prior to condensation. To extract the expected condensation head load, we translate the enthalpy change required for evaporation from the xenon standard-temperature and pressure boiling point to our actual incoming gas stream temperature at the inlet to HX2's condenser, using:

$$\Delta H_{vap}(T) = \Delta H^0_{vap} + \int_{T_0}^{T_{measured}} (C_{p,vapor} - C_{p,liquid}) dT, \tag{4.3.5}$$

where ΔH^0_{vap} is the enthalpy change of the phase-change at STP (at temperature $T = T_0$), $T_{measured}$ is the measured condensation temperatures at the inlet of HX2, and $C_{p,j}$ is the specific heat as a function of temperature for the j^{th} phase. Combining equations 4.3.4 and 4.3.5 with our knowledge of P$_{cooling}$ we compute the efficiency of the HX system as a function of flow by comparing the expected power load, equation 4.3.4 and the measured thermal power load, determined in section 4.3.1, for each tested flow rate:

$$\epsilon = 1 - \frac{P_{measured}(f)}{P_{expected}(f)}. \tag{4.3.6}$$

4.4 Heat Exchanger System Performance

Figure 4.6 shows the derived heat exchange system efficiency versus flow (top) and applied heater power (bottom). Overall the design performs within operational specifications for the duration of the testing, with efficiency greater than 90% at the sustainable long-term circulation rate of 27 slpm. To test for consistency the result at 10 slpm is taken twice, separated by a three-day period to ensure hysteresis effects are mitigated by the above method. The cyan point at 27 slpm comes form a second test at this flow-rate, in which we did not allow enough time for the heater system to settle to stable output power, as is done in all other points below 30 slpm. Due to circulation pump output pressure limitations the point at 38 slpm is also taken without allowing full equilibration to a steady-state. The lower measured efficiency during the test without waiting for stability indicates the estimates are conservative despite not waiting for full thermodynamic equilibrium in which all component temperatures are constant, a process that would have taken an unfeasible amount of time given the size and scale of the LUX detector.

Error bars in figure 4.6 are dominated by uncertainty in the MFC calibration, here assumed to be a flat 5% after calibration, not shown on the x-axis for clarity. Error bars also account for statistical uncertainties from fitting of temperature curves of all components, the PID heater powers step size of 2.5W, and uncertainties from the initial stable zero-flow state used in differential comparison.

Examining figure 4.6 we observe that at 5 slpm the HX system fails to provide efficient heat exchange before becoming efficient at higher flows. This is presumably caused by some condensation happening prior to HX2, likely in a long run of UHMWPE tubing that coils around the top copper gamma shield. This coil of tubing is present to allow the system flexibility during movements of the conduits, such as during detector installation. This idea is supported by the fact that the majority of the heat load from 5 slpm circulation appears on the top heater, resulting in the PID loop outputting lower power. At higher flowrates residual heat load appears on the bottom heater, as designed. As previously described, the output fluid from HX2 is routed through a channel in the FCS prior to entering the active region. With the FCS being directly coupled to the bottom thermosyphon. We

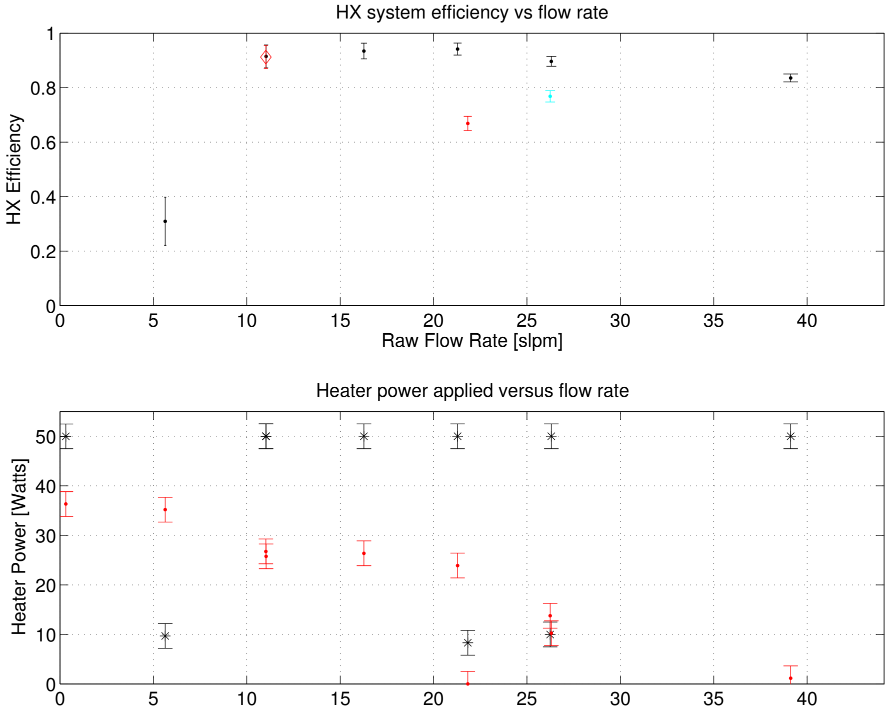

FIGURE 4.6: [Top]: Calculated HX system efficiency versus flow rate (black points). Error bars include statistical error from fitting to component temperature slopes, PID heater step size, and mass-flow-controller flow-rate uncertainty, not shown on the x-axis for clarity. Applying the outlined method without waiting for stabilization of the heater powers resulted in an estimated lower efficiency at a given flow rate (cyan) and is used only for comparison to the datum at 38 slpm, where full stabilization is not possible, due to pump output pressure limitations. Hysteresis tests were performed at 10 slpm [red diamond] and found to be of minimal effect. Purge flow effects were also tested at 22.75 slpm [red dot] with 1.75 slpm flow via the purges to duplicate normal running conditions. Purge flows do not use the HX system for evaporation and so result in a loss of thermodynamic efficiency. [Bottom]: Top and bottom PID output powers versus flow rate. At 5 slpm the top heater power observes more thermal load, postulated to be the result of some condensation happening prior to HX2 due to the low flow rate, explaining the lack of efficient heat-exchange at this flow.

thus expect variation output power of the bottom heater, which is directly coupled to the residual heat load from the fluid stream when the system is operating normally.

As described previously, the detector makes use of a set of four low-flow purges to mitigate outgassing contamination. We observe the effects of these purges in the red data point at 22.75 slpm, as compared to the black data point at 21 slpm. Purges were set to 1.75 slpm (total), duplicating settings used for full system running. Purge flows do not use HX1/HX2 for evaporation or outgoing heat exchange, but do enter the main gas stream in the external piping before returning through HX1 and the condenser side of HX2. A loss of efficiency is expected as this configuration creates unbalanced flow between the sides of the two heat-exchangers.

In addition to efficiency measurements, differential pressure measurements between the HX2 evaporator/condenser and active region pressure are measured and are shown in figure 4.7. Measurements have been converted to a liquid column height in centimeters using $\Delta P = \rho g h$. All height measurements are displayed relative to the liquid surface of the active region. For reference purposes the figure also labels the length of the condenser below the active region liquid level and the length of evaporator above the active region liquid level. As observed in [66] the inferred condenser liquid level hovers around the output level of the condenser chamber, presumably because the differential pressure measurement is sensitive to where an effective liquid column surface would be, with condensation happening on the condenser tube walls and dripping down before forming a surface.

Error bars account for uncertainties in the liquid xenon density, noise variance in the differential pressure sensor, and any drift observed in sensor calibration using *in situ* calibration. For the evaporator, uncertainty in calibration of the weir level sensor, used to cross calibrate from the weir liquid surface to the active region liquid surface, is also included. Above 20 slpm we observe the evaporator column height approaching the top of HX2, but this offers an incomplete picture as these measurements fail to describe the non-uniform evaporation region. It is well known that evaporation processes in vertical tube heat exchangers do not produce well constrained transition points but instead turbulently transition over

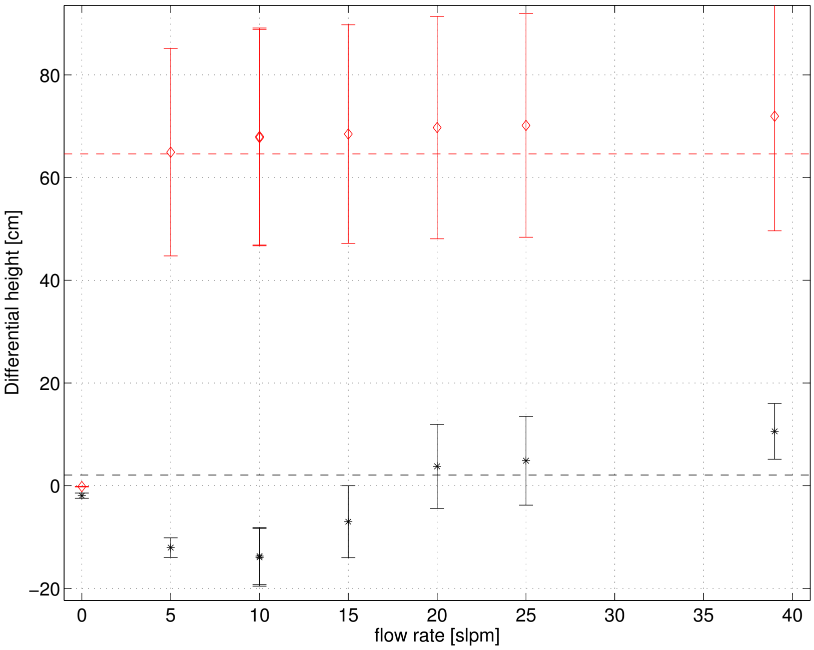

Figure 4.7: Calculated effective column offsets (in cm) as measured from the active region xenon liquid level for HX2 condenser (red) and evaporator (black) versus flow rate in slpm. Also shown are effective physical size limits of HX2 regions for condenser (dashed-red) and evaporator (dashed-black) relative to the active region liquid level. Error bars account for uncertainties on liquid density, noise in the differential pressure sensor, and any drift observed in sensor calibration using *in situ* calibration. Evaporator liquid column uncertainties also account for uncertainty on the calibration of the weir level sensor, used to cross calibrate from the weir liquid surface height to active region liquid level. No treatment of the evaporation liquid level to account for the expected turbulent phase change region is done, possibly contributing an increased systematic error to the evaporator differential height with increased flow.

some extended region from pure liquid to gas through a variety of possible flow configurations observed experimentally: bubbly, slug, churn, annular, and mist-flow [78]. As no treatment of the turbulent nature of the height measurement is done, we defer to the measured HX efficiency, which effectively integrates over these effects through the process of measurement.

4.4.1 Purification of the Xenon Target

Purification of the LUX detector active region is monitored by measuring the electron-lifetime during ^{83m}Kr injections as well as directly during WIMP search data taking using high energy background gammas and alphas. Electron lifetime, τ, is defined by:

$$S2(dT) = S2(T=0) \cdot e^{-t/\tau}, \tag{4.4.1}$$

where dT is the drift time of an observed event and S2(T=0) is the size of S2 events observed at the liquid surface, and τ is the electron lifetime. Measurement is done using the relative fall off in the observed S2 size versus depth, figure 4.8, by linear fitting to expectation values in binned regions of data, where the expectation values come from gaussian fits within each bin.

The measured electron lifetime is used to re-normalize events below the liquid surface as a multiplicative constant to increase the event area, adjusting for this effect in the WIMP search data.

By measuring the field dependent electron drift velocity, found to be 1.51 ± 0.01 mm/μs, using measurements of the location of the cathode grid in drift-time space, conversion to electron drift length is also possible, figure 4.9. WIMP search data is corrected for electron lifetime calibration during the science run. Blue dashed lines in figure 4.9 represent the start and end times of the first 85.3 live-day science run of LUX.

LUX was purified from initial xenon condensation to an, as measured, electron lifetime of $\tau = 575\mu$s, suitable for the beginning of dark matter search data acquisition, in a period of $\sim$2 months, as compared to Xenon100 achieving 154 μs drift length after $\sim$ 4 months purification prior to their initial science run. We also note the xenon mass used in Xenon100 of 161 kg, as compared to the 370 kg used in LUX [46][79].

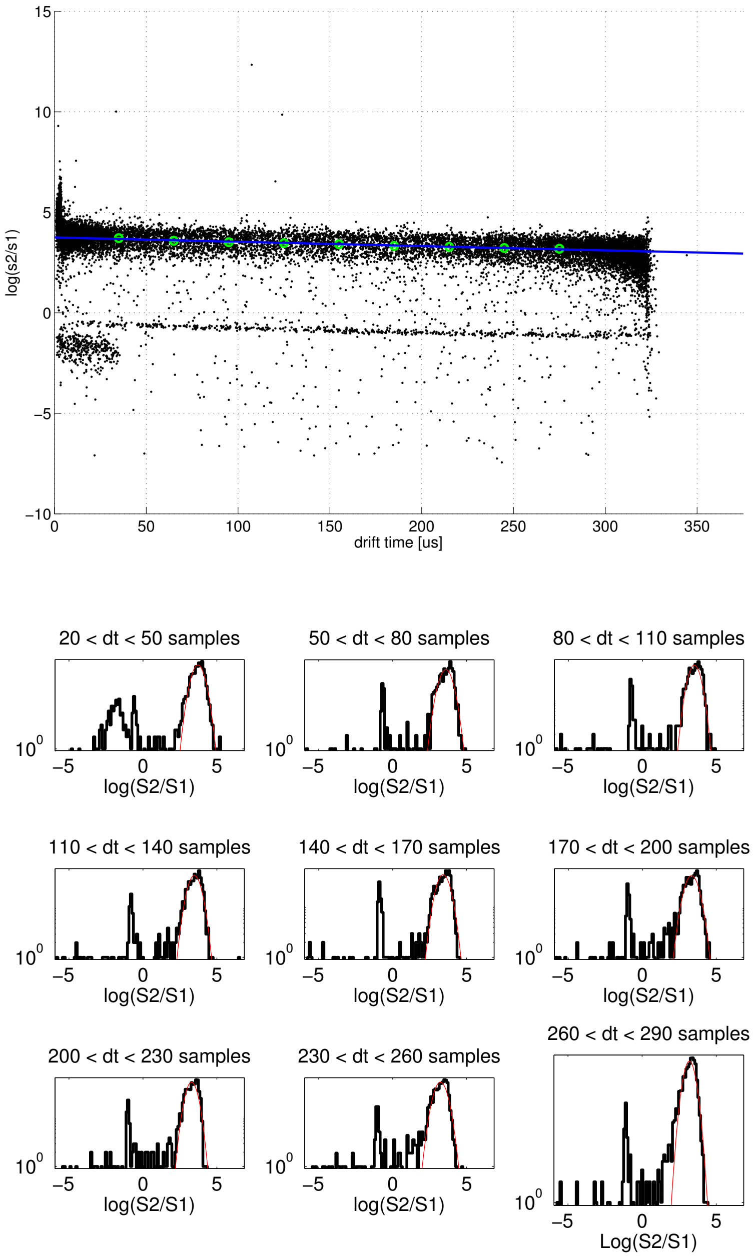

FIGURE 4.8: [Top]: Example fit to determine electron lifetime in log(S2/S1) vs drift-time (blue). Data (black) are background events, with the main population being from high-energy gammas. A second population of alphas appears below with smaller population density, and as a population between 0 and 40 us, from the walls and gate/grid, respectively. Alphas are determined to be from ^{222}Rn and its progeny. Linear fit (green line) is done to expectation value in each bin (green points) from underlying an gaussian fit to data in each bin of drift-time; errors are the size of the points. Fitting is only done between 20 and 290 samples to avoid effects from the grids. The cathode grid is between 318-320 μs in this figure. Here we find $\tau = 464.7\pm^{11}_{10}$ μs. [Bottom]: Binned histograms of log(S2/S1) (black) cut in time bins of 30 samples (300 ns), as used in the fit above. Also shown are the gaussian fits in each time bin (red), which determine the mean and error on the mean for the above green points.

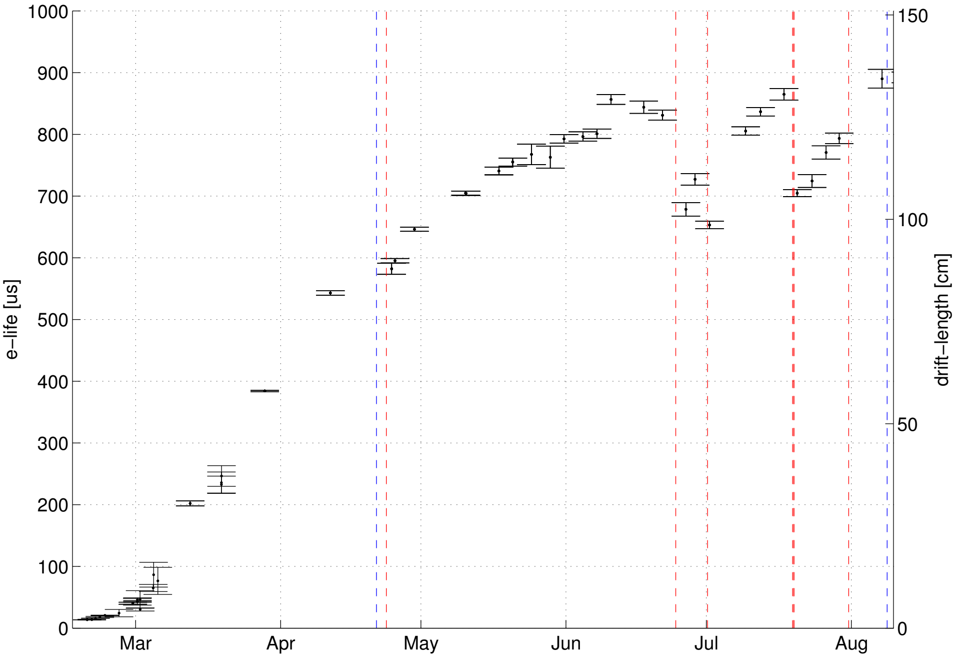

FIGURE 4.9: Measured electron lifetime, and drift-length versus date (black points). Purification, and corresponding increase in measured electron lifetime, is accomplished via circulation through a heated getter at 26.75 slpm, of which 25 slpm is active region turnover and 1.75 slpm is purge flows. Vertical blue dashed lines represent the boundaries of the WIMP search data-taking, while vertical red dashed lines represent circulation loss due to power outages in the laboratory. Purity loss after circulation loss is expected as impurity concentrations will rise during such times, under the assumption of a diffusive source such as the plastics in the LUX detector, which contribute a continuous outgassing profile. The drift-length calculation is based on measured mean electron drift velocity of 1.51 ± 0.01 mm/μs. The LUX detector internal active region height is 48 cm (cathode-to-gate).

4.4.2 LUX Run Stability and Performance

Success of the LUX heat exchanger system is also judged by its ability to maintain cryogenic stability over time periods at the level of hundreds of days. To determine the overall system stability we examine the detector pressure using a Setra 759 capacitance manometer, range 0-5000 Torr, with an accuracy of 0.1 Torr. Figure 4.10 shows the overall calibrated capacitance manometer measurement of detector pressure for the duration of the first WIMP search, down-sampled to one minute readout. Red lines depict 1% pressure variation outside which data is not used.

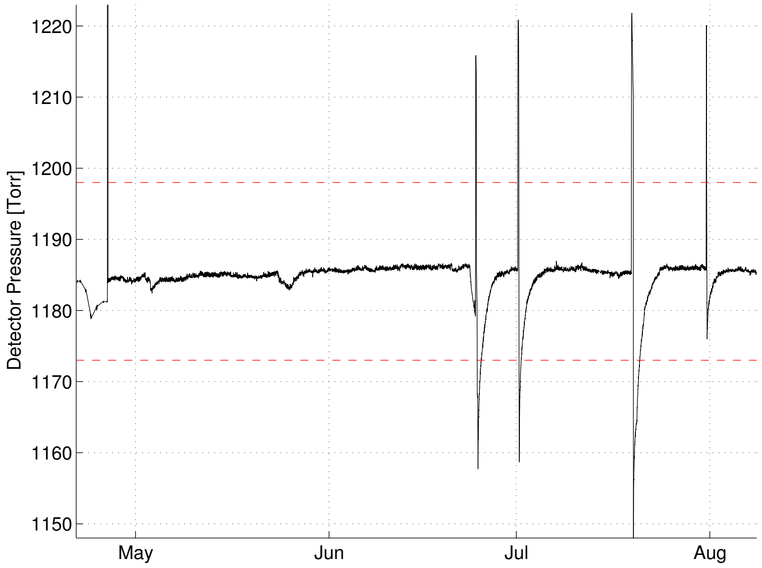

FIGURE 4.10: Detector pressure versus time over the duration of the WIMP search [black]. Readout is done using a calibrated capacitance manometer. Horizontal lines [red] are 1% variation on the mean pressure as measured over the course of the run. Sharp spikes observed in the data correspond to power outages in the laboratory and resulting loss of circulation. The first LUX result discarded periods of data with deviation in pressure > 1%.

Sharp spike features are circulation loss periods resulting from power outages, during which the system is observed to leave its equilibrium state and data is discarded.

Conversion from pressure to inferred temperature variation is done using the xenon liquid-vapor equilibrium curve [77], figure 4.11. The HX system provided platform stability of $\Delta T < 0.2$ K throughout the WIMP search. Measurements of active region liquid-level change were also performed, with variation on the mean S2 extraction region liquid level maintained below 0.2 mm over the course of the WIMP search, section (4.5). Lifetime lost to various detector related effects, including all periods due to change in active region liquid level, detector pressure, or grid voltage account for 0.8% dead-time during the first WIMP search [47] as discussed in section (4.6).

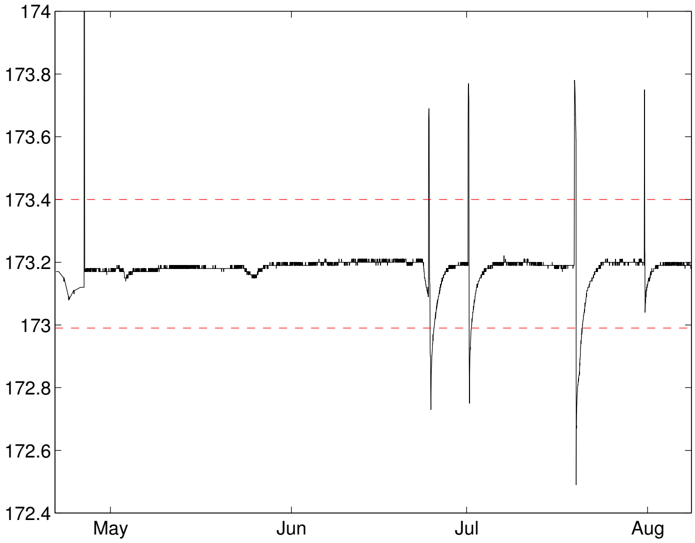

FIGURE 4.11: Conversion from detector pressure to temperature using xenon equilibrium curve [black]. Corollary to figure 4.10. Horizontal lines denote 1% variation in detector pressure converted into Kelvin. Variation over the entire run is < 0.2 K barring power outage spikes during which loss of circulation cause the system to leave thermal equilibrium.

4.5 LUX Liquid Xenon Level from Single Electron Size and Residual Variations

We examine observed fluctuations in the mean single electron size $\langle 1eS2 \rangle$ in photoelectrons over the course of the WIMP search to estimate the underlying variation in the S2 region liquid level.

Figure (4.12) shows the as measured full-array mean single electron size over the course of the WIMP search as used in the first WIMP limit. Systematic jumps in the data were found to correlate with DAQ event rate, caused by a bias in how events were selected. Here, all single electron pulses were used, resulting in a bias towards larger single electron sizes, events of which display greater trigger efficiency. This bias is more pronounced during WIMP search data taking as the lack of frequent additional triggers lead to a skewed sampling of the underlying population. This bias is mitigated during high event rate datasets, such as ^{83m}Kr

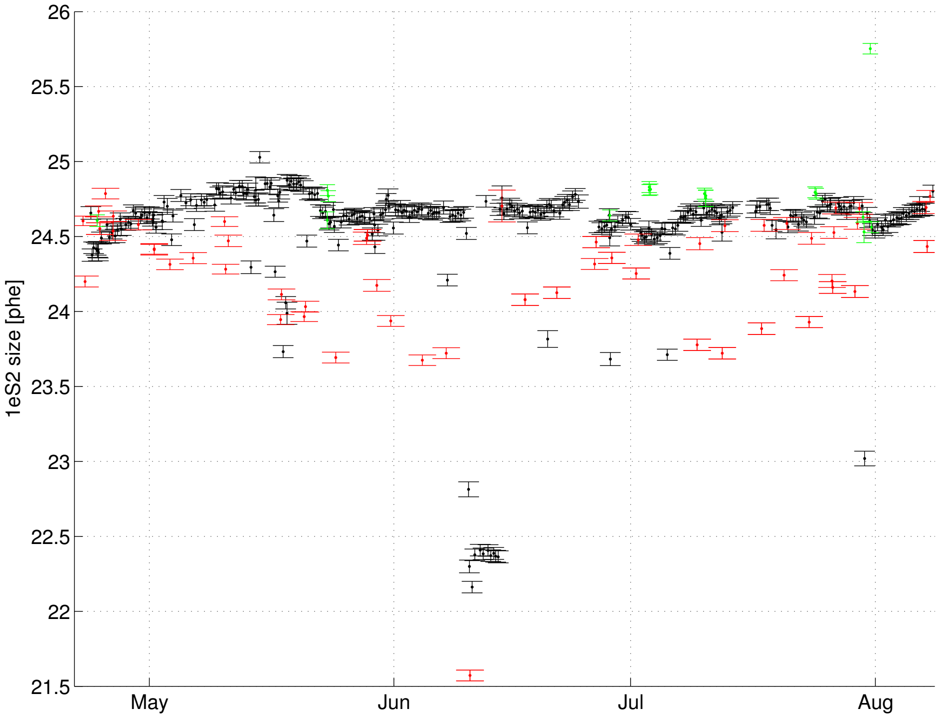

FIGURE 4.12: Mean single electron size in photoelectrons,$\langle 1eS2 \rangle$, across both arrays as determined *in situ* by gaussian fitting population in every recorded dataset over the 85.3 live-day WIMP search. Variation observed is found to correlate with DAQ event rate, due to a bias introduced through the use of all single electrons, biasing towards large single electrons that were more likely to trigger the DAQ during sparse data such as AmBe [green] and WIMP search [black] data as compared to high event rate data such as ^{83m}Kr [red].

injection datasets, as the additional triggers due to the source event-rate result in a better sampling of the true underlying single electron distribution.

Computing the Pearson product-moment correlation coefficient shows clear correlation between the DAQ rate and DAQ temperature, as higher event rates directly raised the temperature as measured in the DAQ rack,as well as correlation with physical liquid levels and temperatures, figure (4.13).

To correct for this bias, a reanalysis in which only single electrons that were between already triggering S1 and S2 pulses is done, figure (4.14).

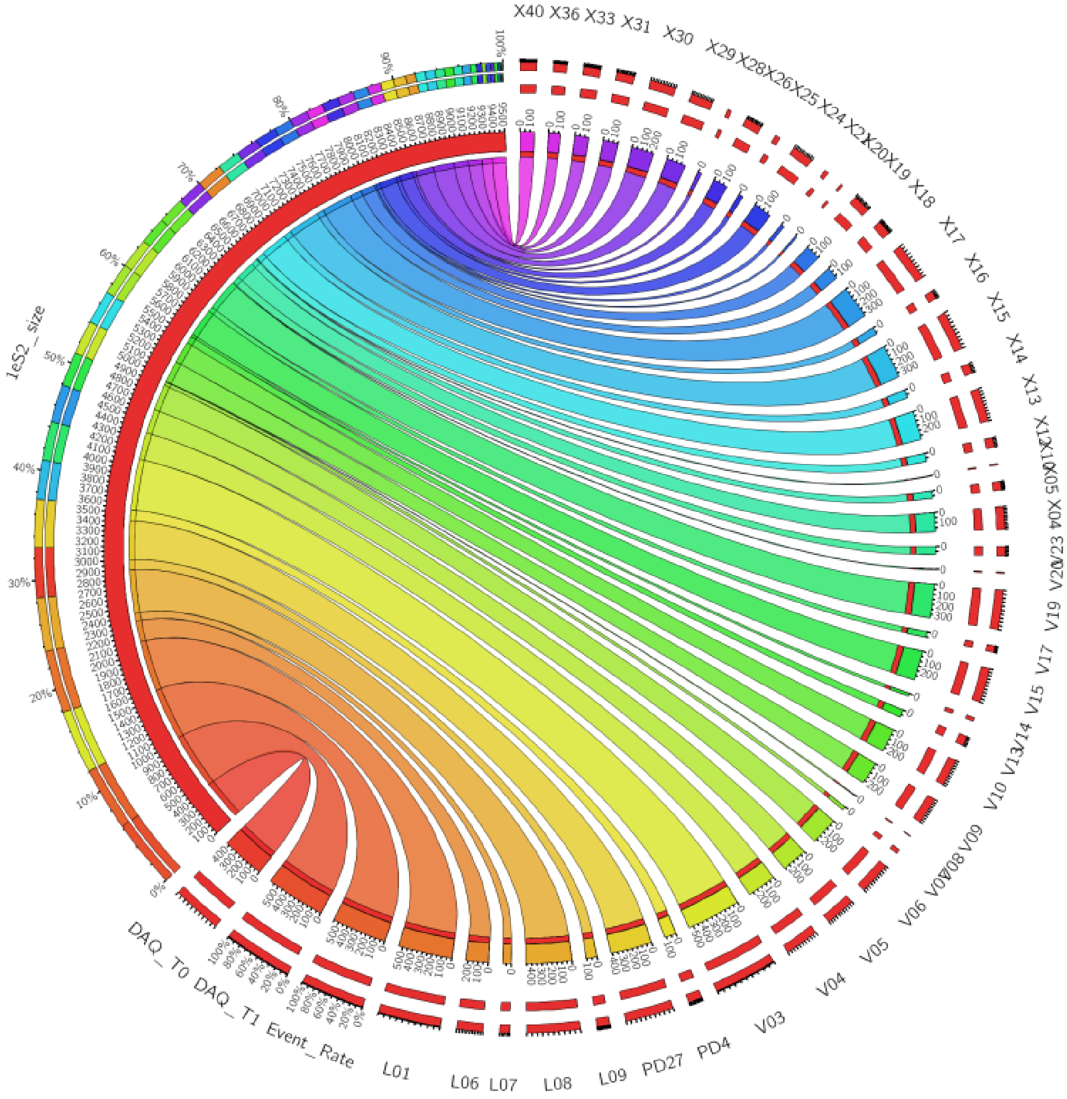

Figure 4.13: Circos diagram of the absolute value of the Pierson Correlation Coefficient (x1000) as measured between mean single electron size in photoelectrons,$\langle 1eS2 \rangle$, and detector parameters. Plot is read by comparing fractional arc-length on the left arc labeled (1eS2_size) to the various connected right-side arcs, which are grouped by subsystem type. L liquid levels [L-], detector pressures [P-], detector temperatures [X- for xenon volume, V- for vacuum jacket.], and DAQ event rate and temperature. Correlation found between DAQ rate and temperatures are due to the described bias in event selection criteria.

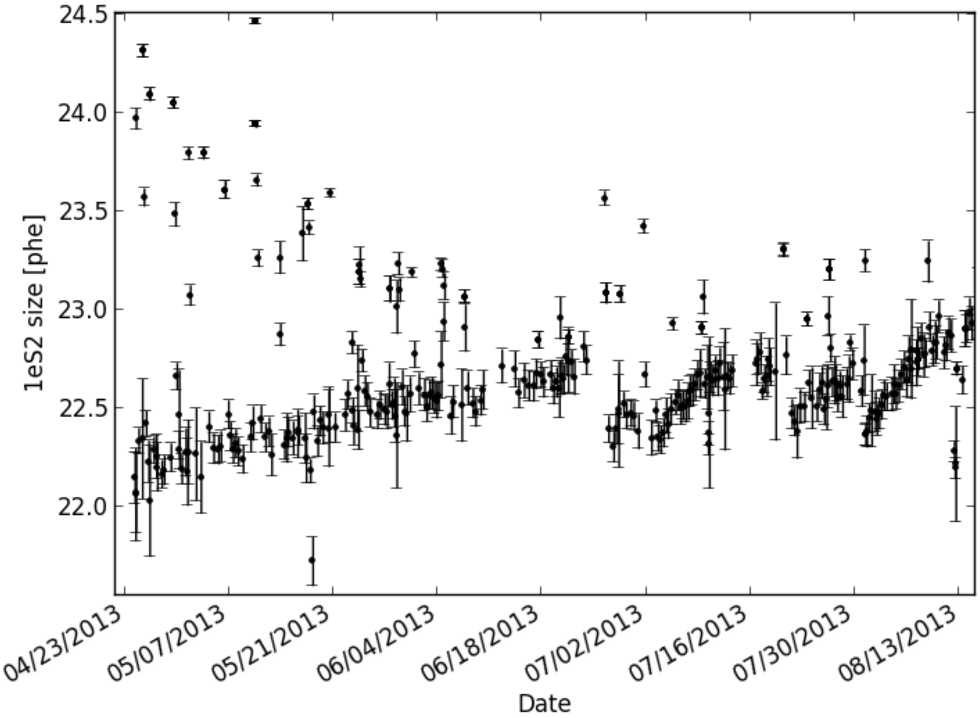

FIGURE 4.14: Mean single electron size as a function of time estimated from data taken during the WIMP search. Data presented here were processed using only single electron pulses occurring between a valid S1 and S2 pulse, eliminating trigger bias. Selection criteria require at least 100 electron pulses to be calculated.

Taking the the observed variation in the mean single electron S2 size as a function of time during the run, figure (4.14), we conservatively attribute all observed variation to potential changes in the liquid level, setting a maximum size of 24.5 phe and minimum size of 21.5 phe. We compute the resulting variation in the S2 region liquid level, following the empirical formula [80]:

$$N_{\gamma,scintillation} = \alpha N_e (E/p - 1) p d. \tag{4.5.1}$$

Equation (4.5.1) gives the expected the number of scintillation photons produced, $N_{\gamma,scintillation}$, in an S2 event relative to p, the gas pressure [in bar], E, the extraction field in the gas [in kV cm^{-1}], d, the distance traveled by the extracted electrons [in cm], $\alpha \sim 70$ the amplification factor, and N_e the number of electrons extracted from liquid to gas phase, here taken to be one. From equation (4.5.1), and taking $E = 6.6$ kV/cm [81] and pressure of $P = 1.58$ bar, from figure (4.10) we compute our sample as having $\Delta d < 0.01$ mm liquid level variation.

4.6 Detector stability Cuts for the first WIMP search

Despite achieving broad level system stability using the heat exchanger system discussed above, some quality cutting of data is necessary during the first WIMP search. Quality cuts are required due to laboratory wide power outages and resulting system restart. This section details the algorithm for these quality cuts, a subsection of which are used for the first WIMP search result.

To flag periods of detector instability, variation from mean run values are measured for the liquid level in the S2 extraction region, monitored grid bias voltages and currents, outer vacuum vessel pressure, purge and circulation flow rates, and detector pressure. We apply a rolling box filter algorithm to each sensor to identify periods where the sensor is out-of-bounds with respect to pre-selected allowable ranges of variation, chosen so variation for the sensor is contained at the less than 2% level or so the bounds contained two step sizes of the read-out unit. The rolling-box filter merges all out-of-bounds periods that occur in a 5 minute sliding window that resets upon each out-of-bound entry. This algorithm merges periods of frequent sensor fluctuations into unified time windows where data could contain anomalous detector-related effects. For example, if sensor 1 went out of bounds four times in a fifteen minute window, at times 0, 2, 7 and 15 mins the algorithm would find two outages, the first from 0-7 minutes, and another at 15 minutes. Once all outage periods have been identified, the algorithm then re-orders outages based on outage type as described in table 4.2.

Outages are then checked to determine if an outage is characterized as a “zero-length” event. Zero-length outages are defined as a sensor going out of bounds for a single read-out period. As these outages have effective length of zero, we assign to them length based on the sensor’s average update period in a 10 minute

Outage type	**Related Sensors**
S2 level	LS06, LS07, LS08
Grids	Top Voltage, Anode Voltage, Gate Voltage, Cathode Voltage, Cathode Current, Bottom Voltage
Outer Vacuum (OV)	PT-D6
Purge	MFC3, MFC4, MFC5, MFC6
Circulation	MFC1, MFC2
Pressure	PT-D3

Table 4.2: Table of Sensors by Subsystem as Used for the Data-Quality Cuts

window surrounding the zero-length outage, extending the zero-length outage by one update period before and after the read-out point. This approach ensures that any periods of possible instability are flagged, and is especially important for slowly updating sensors, which may only refresh every two to three minutes. Though these outages are generally electronics noise, each is flagged as a possible real system failure for further analysis. As a final step, circulation outages are adjusted as follows. Normally, a sensor outage is considered over as soon as the affected sensor comes back into its pre-defined bounded region, however for sensor outages related to circulation we apply a more conservative constraint, extending the found period until the next ^{83m}Kr dataset is taken, to ensure that any effects on electron lifetime are correctly measured.

Results of these quality cuts were written to the collaboration database and stored by outage type, including a flag for all zero-length outages of a specific type, allowing for the direct application of pertinent combinations of various cuts to individual data-analyses as appropriate. Figure 4.15 indicates the cumulative effect of the algorithm described, broken down by major subsystem category. We observe that while the outer vacuum flag is the most common outage, the vast majority of its outages are of the class previously described as zero-length, and are the result of electronics noise. For the first WIMP result the full set of detector quality cuts used is given in section (4.7).

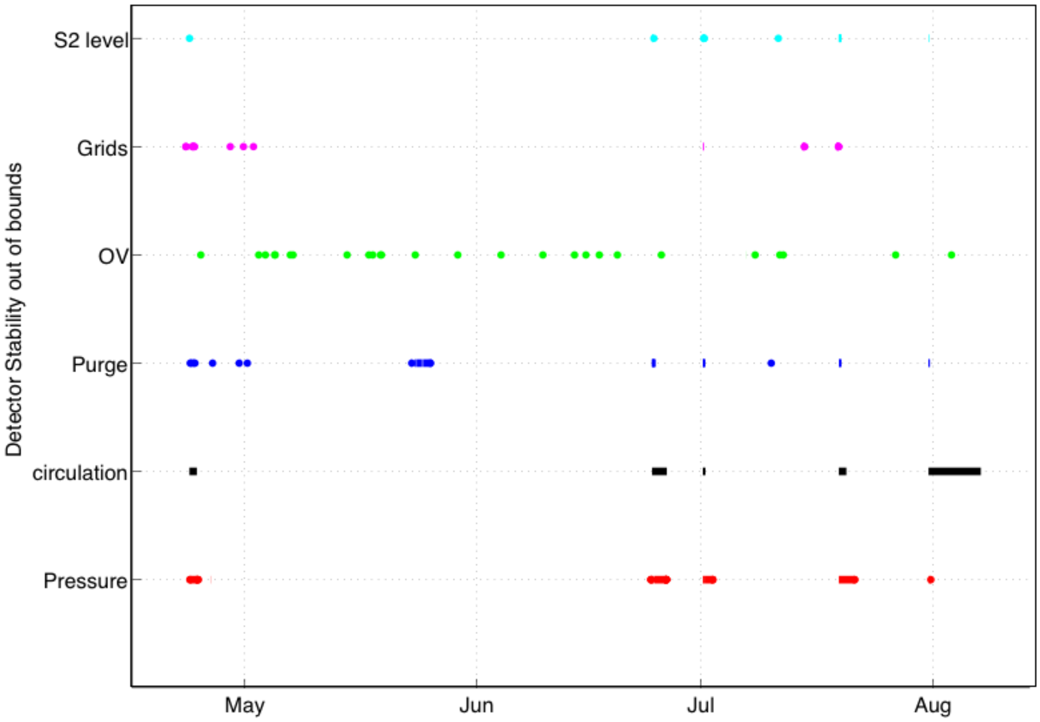

Figure 4.15: Detector stability results over the duration of Run3 divided by subsystem. Colored periods are periods where at least one sensor in the associated subsystem is outside of pre-defined limits. Rounded circles are zero-length outages, set to have a duration of 2 update periods centered on the out-of-bounds time, while squared edges are the result of non-zero length outages.

4.7 WIMP Search Detector Stability Cuts

For the WIMP search, cuts on purge-flow were found to be redundant with monitoring of electron-lifetime and no periods of outer-vacuum pressure outages were observed to cause significant thermal effects resulting in a $> 1\%$ $\Delta P/P$ rise in the detector pressure, which is directly monitored. Circulation cuts were found to be entirely redundant with cuts to detector pressure except for a single outage in late July, where, due to a failure to reset the ^{83m}Kr source injection MFC resulted in a failed injection, with no rectifying action taken for several days. Handling of this circulation outage is discussed in the following section.

The full set of detector stability quality cuts used in the first WIMP search are:

- Any variation on the capacitively measured S2 region liquid level outside accepted bounds of 1 % variation on the measured mean liquid level over the course of the run.
- Any variation on grid voltages or currents outside accepted bounds of two digital step-sizes of the monitoring unit.
- Any variation on detector pressure outside accepted bounds of 1 % variation on the measured mean detector pressure over the course of the run.

Overall the detector provided a very stable platform upon which to conduct the WIMP search, with only 0.8% data live-time loss due to all detector stability quality cuts [47].

4.7.1 Circulation loss July 31st, 2013

This section describes attempts to correct for the loss of circulation beginning July 31st, 2013 at 10:34:30 MST following a power outage in the laboratory, which resulted in xenon circulation loss. The circulation loss lasted two hours and 51 seconds, ending at 12:35:21. After the circulation loss, the on-site crew attempted to perform a ^{83m}Kr injection, as is standard procedure, but failed to observe any ^{83m}Kr events inside the LUX active region. This was later diagnosed by off-site experts as being due to the ^{83m}Kr injection system mass-flow controller not being reset properly following the power outage. A ^{83m}Kr injection was successfully performed on August 7th, 2013 at 14:02:58 MST. As described in the previous section, this would normally result in a data-quality cut over the corresponding period of approximately 8 days, which would have corresponded to $\sim 7-9\%$ loss of live-time during the first WIMP search.

The basic criteria for the data-quality cut on circulation, as described in section (4.6), is that following circulation loss, the detector may experience a decrease in electron lifetime resulting from the outgassing of electro-negative impurities from various components. As this outage was not discovered until the end of the WIMP search period, recovery of this data period is done by reconstructing the e-lifetime

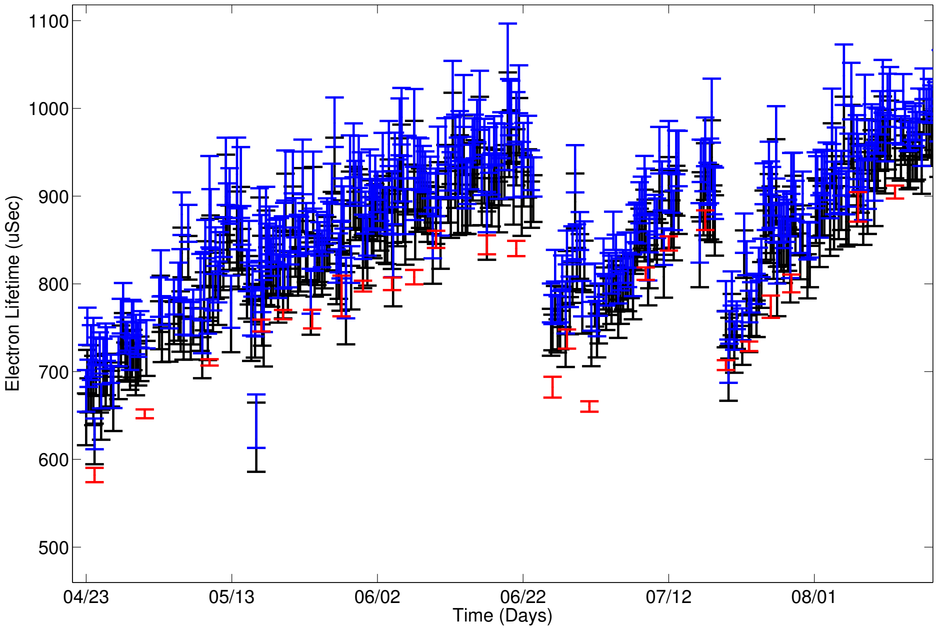

FIGURE 4.16: Electron lifetime as measured by three different methods. Red points are from direct ^{83m}Kr e-lifetime measurement as shown previously in figure (4.9). Blue points are from a maximum likelihood reconstruction of lifetime through the application of a gaussian constraint on the depth-corrected alpha populations resulting from radon progeny. Blue points are the application of an attenuated gaussian constraint to the same radon progeny alpha populations used in Blue but uncorrected for depth. Difference between data in black and blue gives estimation of the systematic error in these estimates. As there is some systematic offset between the direct measurement data from ^{83m}Kr and the likelihood approaches, estimation is done of overall possible effects of e-lifetime loss on the WIMP search following the July 31st outage. Figure reproduced from [82].

using alpha data via a maximum likelihood technique, figure (4.16) [82], resulting in its inclusion in the first WIMP search result as presented in chapter 7.

As the three estimators of electron lifetime show some systematic offset over the WIMP search we conservatively estimated the possible bias introduced by using the incorrect electron lifetime, figure (4.17). Though we know that any loss of circulation can only decrease the electron lifetime, we model effects from possible electron lifetimes between 500 μs and 900 μs, estimating the difference in log(S2), to mirror the choice of log(S2/S1) used in the WIMP search. Here the magnitude of the effect is measured between S2 event area if corrected with a flat selected

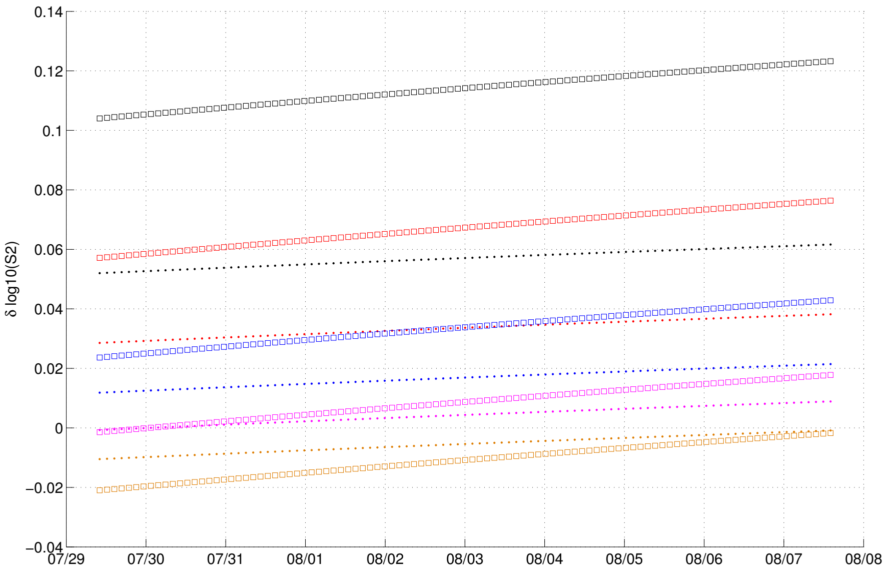

FIGURE 4.17: Examination of the overall shift in $\log_{10}$(S2), as used in the LUX for nuclear and electron recoils, chapter 7, resulting from application of possibly incorrect electron lifetime. Estimator is made by comparing the difference in corrected S2 event area if corrected with a flat selected electron lifetime, representing possible conservative estimate for effects of circulation loss and the electron lifetime as used in the WIMP search analysis, a linear interpolation between the closest ^{83m}Kr datasets. Black - 500 μs electron lifetime, Red - 600 μs electron lifetime, Blue - 700 μs electron lifetime, Purple - 800 μs electron lifetime, and Orange - 900 μs electron lifetime. Positive values of δ indicate shifts in which the S2 event area would be smaller than estimated from the WIMP search data. Shifts in event size are presented both for events from the bottom of the detector [squares], where the effect is greatest, and from middle of detector active region [dots].

value for the electron lifetime over the period of circulation loss as compared to the electron lifetime as used in the WIMP search data processing, a linear interpolation between the closest ^{83m}Kr datasets.

Using possibly incorrect higher lifetime results in a shift in log(S2) to smaller values for events below the liquid surface. This shift is because the XYZ correction, which normalizes S2 event areas to match those from the surface, would have underestimated the amount of increase to give these events, equation (4.4.1). The net effect is that events during this period would be shifted towards the nuclear recoil band, weakening possible limit results.

From this analysis we find the inclusion of this data is conservative. First, our estimates of the electron lifetime from an examination of alpha backgrounds shows no significant decrease in measured electron lifetime across this time period. Second, modeling possible effects due to reduction of electron lifetime up to 500 μs show only small possible effects on event location with respect to the WIMP search discussed in chapter 7. Finally, bias in S2 size resulting from incorrect application of electron lifetime over this period shift events towards the nuclear recoil band. Thus, any possible bias would result in a weaker limit curve being produced by the final profile likelihood fit. With these conservative estimates, data following the July circulation outage are included in the first WIMP search result discussed in chapter (7).

4.8 Summary

Having examined the LUX heat exchanger system and the rapid purification and stable detector platform provided by its successful implementation, we now turn to detector energy calibration in the next chapter. Once we have developed an understanding of the methods of calibration we finally turn to event site physics before applying them to the LUX experiment's first WIMP search analysis in Chapter 7.

Chapter 5

LUX Energy Reconstruction

Having now described the detector systems and detector performance leading to the first WIMP search, in chapters 3 and 4, we diverge slightly to examine energy reconstruction for events in the LUX detector. This is of obvious importance in a WIMP search as the ability to accurately reconstruct energy directly maps to a quantitative understanding of WIMP sensitivity, as it determines how sensitive the experiment is to the fall off in the spectrum WIMP events with respect to energy, given experimental thresholds.

We begin by reviewing the formulation of the framework of "combined energy," a physical energy scale based on the observation of both the primary scintillation, S1, and secondary scintillation, S2, signals. Here we will follow the work of [65],[83], and [84]. After reviewing the framework we examine the determination of the "unified-gain" parameters, mappings from observed S1 and S2 signals to numbers of quanta, electrons and photons, at the event site. Here we compare several methods eventually settling on a "data-centric" model to treat systematic errors. With an energy calibration in hand we move to the deconvolution of event-level fluctuations into three constituent pieces in chapter 6, which addresses intrinsic discrimination power of this class of detectors. Finally in chapter 7 we will return to the first WIMP search result.

5.1 The Combined Energy Framework

The idea of an accurate reconstruction of event energy is of importance to a WIMP search. We expect the WIMP signal to deposit only small amounts of energy, and to have an exponentially falling differential rate with respect to energy. To determine the detector WIMP sensitivity LUX makes use of comparison to simulated signal for halo models with WIMPs of different mass. These models tell us the WIMP signal as function of energy, and our energy reconstruction then provides the mapping that tells us our intrinsic sensitivity to these signals. Combined energy seeks to break down the relationship between energy deposited, in some highly localized track of ionization and excitation, and the number of quanta produced at that event site. Here we will review the fundamentals before moving on to calibrations in the LUX detector.

5.1.1 Microphysical model for Interactions in Liquid Xenon

Interactions in liquid xenon produce tracks of excited xenon atoms (excitons), ionized xenon atoms (ions), and “soft” elastic recoils with xenon atoms (which eventually thermalize as heat). Interactions can be characterized by their type, either an electron recoil, in which the incoming radiation interacts with the electron cloud of the xenon atom, or a nuclear recoil in which the radiation interacts with the nucleus of the xenon atom. For electron recoils, ~90-95% of the energy is distributed in the ionization channel and only a very small amount of energy is lost to heat. For nuclear recoils, significantly more energy is produced in the heat channel and an almost even split between ion and exciton production is observed [59]. Excitons can be produced both directly at the interaction site or when a freed electron from the event track recombines with a freed ion through a process called recombination. Excitons decay via the formation of an excited xenon dimer, Xe_2^*, which emits a 178 nm (VUV) photon as it decays back to two ground state xenon atoms, figure (2.3). The total number of produced VUV photons from the event site is then:

$$N_{ph} = a \cdot N_{ex} + b \cdot r \cdot N_i, \tag{5.1.1}$$

where N_{ph} is the number of produced scintillation photons, N_{ex} is the number of produced excitons in the track not produced by recombination, r is the recombination fraction, the fraction of ions that recombine, and N_i is the number of ions produced in the track. Here, the efficiencies for recombined ions and direct excitons to produce scintillation photons are b and a respectively, with the expectation that $a \approx b \approx 1$ [65]. Under an applied electric field, electrons that do not recombine can be extracted from the event site with the amount of extracted charge being:

$$N_q = (1 - r)N_i. \tag{5.1.2}$$

5.1.2 Electronic Recoils

We define a new parameter, W_{ph}, as an energy calibration factor in an event with full recombination, $\mathrm{N}_q = 0$.

$$\frac{E}{W_{ph}} = a \cdot N_{ex} + b \cdot N_i \tag{5.1.3}$$

where for future convenience we will rename our parameters $\mathrm{W}=\mathrm{W}_{ph}\cdot\mathrm{b}$, $n_e = \mathrm{N}_q$, and $n_\gamma = \mathrm{N}_{ph}/\mathrm{b}$ resulting in three new equations:

$$E = (n_e + n_\gamma) \cdot W, \tag{5.1.4}$$

$$n_e = (1 - r) \cdot N_i, \tag{5.1.5}$$

and

$$n_\gamma = \left(\frac{a \cdot N_{ex}}{b \cdot N_i} + r\right) \cdot N_i. \tag{5.1.6}$$

Here, the fundamental property of our model is that energy reconstructed by equation (5.1.4) is insensitive to the number of electrons that undergo recombination, as recombination provides a one-to-one mapping of n_e to n_γ while our energy is only dependent on the sum in the two channels. With a value of W, 13.7 ± 0.3 eV, from the average over all available data [65], [83], we have then defined our complete model for electron recoils. We note that n_γ is not the true number of recombining electrons, but rather an effective number of recombining electrons that would have been required to produce an equivalent signal in the absence of direct exciton production. Here we treat $\frac{aN_{ex}}{bN_i}$ as a constant under the expectation that the ratio of direct excitation to ionization is energy independent [59].

5.1.3 Nuclear Recoils

While for electron recoils, energy is lost almost exclusively through ionization, for nuclear recoils a much more significant fraction of energy is deposited via elastic collisions with nuclei, the heat term described in section (5.1.1). This relative loss of observable energy, as compared to an electron recoil of equivalent initial energy, is parameterized via an energy dependent scaling, the Lindhard Factor, $\mathcal{L}(\mathcal{E})$ [50]. The material dependent parameter $\mathcal{L}(\mathcal{E})$ estimates the amount of energy from a nuclear recoil available for signal production, energy that produces ionization or excitation in xenon. We take the standard approximation for the Lindhard factor:

$$\mathcal{L} = \frac{kg(\epsilon)}{1 + kg(\epsilon)}, \tag{5.1.7}$$

following [41], with

$$k = 0.133 \cdot Z^{2/3} \cdot A^{-1/2}, \tag{5.1.8}$$

$$g(\epsilon) = 3\epsilon^{0.15} + 0.7\epsilon^{0.6} + \epsilon, \text{and} \tag{5.1.9}$$

$$\epsilon = 11.5(E_{nr}/keV) \cdot Z^{-7/3}. \tag{5.1.10}$$

We define E_{nr} as the energy of the nuclear recoil, A as the atomic mass of xenon, and Z as the atomic number. Due to this energy loss to the heat channel, relative to electron recoils, we modify our combined energy relation to

$$E_{nr} = \mathcal{L}^{-1} \cdot (n_e + n_\gamma) \cdot W. \tag{5.1.11}$$

Further, since for real events we will be uncertain of the true recoil type, we are required to keep track of two energies. For events known to be electron recoils, e.g. gamma calibration data, we work in units of kilo electron-volts electron-equivalent (keVee). For events we know are nuclear recoils, e.g. neutron calibration data, we work in reconstructed energy in kilo electron-volts nuclear recoils equivalent (keVnr). As the results discussed below are for calibration with respect to electron recoils, betas and gammas, we will work in keVee in this chapter. When nuclear recoil energies are needed, such as in chapter 7 when discussing observed events of unknown origin, we will use the NEST library to calculate the Lindhard factor from historical measurements [83], [85] and label contours in both keVee and keVnr.

5.2 Calibrating Energy reconstruction in the LUX Experiment

Equation (5.1.4) provides a treatment for constructing an energy-scale insensitive to recombination effects, given the fundamental energy per quanta, W and the number of quanta in the ionization and scintillation channels. We must still examine how to reconstruct n_e and n_γ from actual raw data, which we accomplish by defining the overall, position-independent, measurement gains g_1 and g_2 where:

$$S1 = g_1 \cdot n_\gamma, \text{and} \tag{5.2.1}$$

$$S2 = g_2 \cdot n_e. \tag{5.2.2}$$

Here we work with S1 and S2 signals after x,y,z position-correction. We note that for all measurements described here, and in chapters 6 and 7, only the bottom PMT array is used to reconstruct the S2 signal due to a pair of shorted PMTs in the top array. As the S2 light is well localized in the top array, the effect of events occurring below these PMTs could systematically affect reconstruction using the full array. Therefore, all results for g_2 values are relative to signal observed only in the bottom array, to provide the calibration factor most useful during the first WIMP search.

Combining equations (5.2.1) and (5.2.2), with equation (5.1.4) we rewrite the combined energy equation for electronic recoils as

$$E = \left(\frac{S1}{g_1} + \frac{S2}{g_2} \right) \cdot W, \tag{5.2.3}$$

and for nuclear recoils as

$$E = \frac{1}{\mathcal{L}(E)} \cdot \left(\frac{S1}{g_1} + \frac{S2}{g_2} \right) \cdot W. \tag{5.2.4}$$

As W and the Lindhard factor are expected to be intrinsic properties of xenon, we reduce the problem to one of calibrating our detector through the determination of g_1 and g_2. Given fundamental fluctuations at the event level described in section (6.1) we can only find estimators for the true gains, and will take the means extracted from a population of mono-energetic features, $\langle g_1 \rangle$ and $\langle g_2 \rangle$, as there estimators, presenting and comparing three different methods for estimating these quantities.

5.2.1 Energy Resolution Based Determination of g_1 and g_2

As a first method for constructing estimators of the unified gains we create a method of tuning g_1 and g_2 for the best energy resolution possible in some range of energy given constant values of g_1 and g_2. We begin with this treatment both to illuminate why the physical energy may not be the model with the best energy resolution and because this "best resolution" model is of use for identifying subpopulations in the data for the next two methods presented. Therefore, this method is biased and does not construct the physical g_1 and g_2 unless measurement fluctuations in the two signal channels, S1 and S2, are equal and subdominant to recombination fluctuations, as described in chapter 6. As we know these underlying fluctuations change as a function of energy we should expect this method to only provide improved energy resolution in some range of energies and tune our reconstruction to the energy populations from activated xenon.

To understand why the physically based energy reconstruction may not provide the best energy resolution, we present the argument first geometrically, and then algebraically. For the geometric argument we think of a population of events from a monoenergetic source in the space of $\log(n_e/n_\gamma)$ versus our calculated combined energy, where we have chosen $\log(n_e/n_\gamma)$ as it represents the LUX discrimination parameter up to a constant. Our events form some ellipsoid feature in this space, the shape of which is determined by the fundamental fluctuations in S1 signal, S2 signal, and recombination. If we vary our chosen values of g_1 and g_2 we effectively rotate the population. Optimal resolution is achieved when the populations semi-major axis is perpendicular to the energy axis, for which the population will have the best fractional resolution in energy, a one-dimensional projection of the population onto the energy axis. Our choice of g_1 and g_2 determines the angle of the event population with respect to vertical in this space, and we seek values for g_1 and g_2 that minimize this angle. If, as expected, our S1 and S2 signals have different levels of uncorrelated noise from detector effects such as PMT response variation or ripples in the liquid surface, this choice of g_1 and g_2 will de-weight the statistically noisier channel, improving resolution but failing to find the physical values of g_1 and g_2.

Algebraically, we follow the work of [86], and consider a population of monoenergetic events with perfectly anti-correlated numbers of quanta leaving the event site, arising from recombination effects, with some additional uncorrelated noise terms on the S1 and S2 signals related to the measurement process. We seek the factor k, such that $E = S1 + kS2$ has the minimal fractional resolution, where we write the square of this fractional resolution as:

$$\left(\frac{\sigma_E}{\langle E\rangle}\right)^2 = \frac{Var(S1) + k^2\ Var(S2) + 2k\ Cov(S1, S2)}{\langle S1 + kS2\rangle^2}. \tag{5.2.5}$$

We have constructed our model such that

$$S_{i=1,2} \sim g_i n_i + u_i, \tag{5.2.6}$$

where these u_i are the uncorrelated measurement noises for S1 and S2 signals respectively. To introduce recombination fluctuations we construct our distribution of primary quanta, $n_{i=1,2}$, as some mean value, ν_i, related to the energy of the source, plus some anti-correlated distribution of fluctuations f,

$$n_{i=1,2} \sim \nu_i + f. \tag{5.2.7}$$

To find the minima in equation (5.2.5) we take its derivative and set it equal to zero,

$$\frac{\left(2k\sigma_2^2 + 2c\right)\left(\mu_1 + k\mu_2\right)^2 - 2\mu_2\left(\sigma_1^2 + k^2\sigma_2^2 + 2kc\right)\left(\mu_1 + k\mu_2\right)}{\left(\mu_1 + k\mu 2\right)^4} = 0, \tag{5.2.8}$$

where $c \equiv Cov(S1, S2)$, $\sigma_i^2 \equiv Var(S_i)$, and $\mu_i \equiv g_i\nu_i$. We then find the optimal value of k to be

$$k_{opt} = \frac{\sigma_1^2\mu_2 - c\mu_1}{\sigma_2^2\mu_1 - c\mu_2}. \tag{5.2.9}$$

Assuming our uncorrelated fluctuations depend on the number of produced quanta in each channel, as we shall observe in chapter 6, we find

$$\sigma_i^2 = g_i^2\sigma_n^2 + Var\left(u_i|n_i\right), \tag{5.2.10}$$

where $\sigma_n = \mathrm{Var}(f)$. In the limit that no measurement fluctuations are present, $u_i = 0$, combining equations (5.2.9) and (5.2.10) we recover the optimal k as

$$k = \frac{g_1\left(g_1\mu_2 + g_2\mu_1\right)}{g_2\left(g_2\mu_1 + g_1\mu_2\right)} = \frac{g_1}{g_2}. \tag{5.2.11}$$

Or stated equivalently, if there were not measurement fluctuations, or they were much smaller than recombination fluctuations, we would expect to find optimal resolution corresponding to the physical values of g_1 and g_2. However, in the presence of non-negligible uncorrelated fluctuations, such as we observe in chapter 6, this reconstruction fails to produce the best unbiased estimators of g_1 and g_2.

Constructing g_1 and g_2 in this manner is then mainly of service to provide the best resolution reconstruction in some range of energies, extremely useful for identifying event populations in sections (5.2.2) and (5.2.3).

To calculate these optimal resolution values, we use events produced from the decay of cosmogenically activated xenon, short-lived radioactive isotopes of xenon, observable in LUX as a result of activation of the xenon target from surface exposure to neutrons.

Here we identify energy peaks from ^{129m}Xe, ^{131m}Xe, and ^{127}Xe and raster over possible values of g_1 and g_2. For each pair of possible values we estimate the angle of the ellipsoidal distributions with respect to a line of constant energy in the space of $\log(n_e/n_\gamma)$ versus event energy. Summing the angles for the features at 163.9 keV and 236.8 keV, from ^{131m}Xe and the combination of ^{129m}Xe and ^{127}Xe, respectively. Having done this we create a smoothed, interpolated mesh of this sum between the features at 163.9 keV and 236.8 keV and find the minima, figure (5.1).

Unfortunately, the angular offset displays some degeneracy along a line of roughly constant ratio of g_1 to g_2, as would be naively expected given the proceeding algebraic argument. To break this degeneracy we convolve this measure with an estimate of how accurately a given choice of g_1 and g_2 results in the means of our populations being at their true, known energy values, figure (5.2). We have

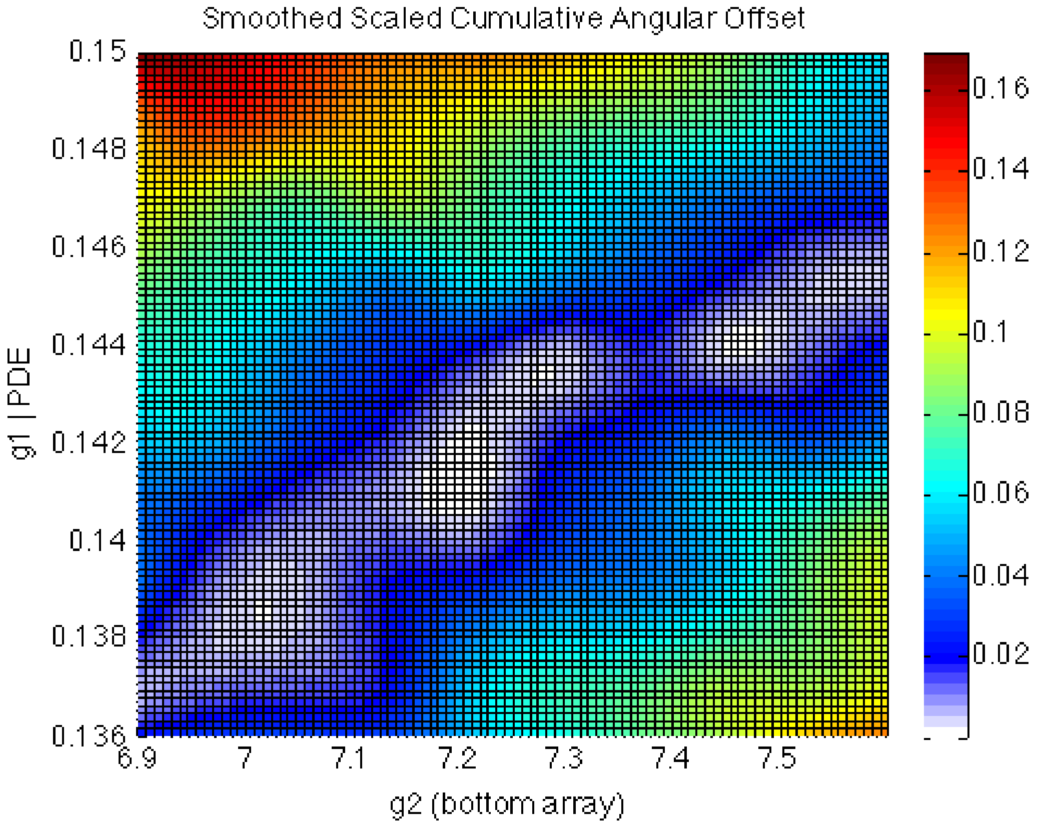

FIGURE 5.1: Measure of the cumulative angular offset (in radians) between a line of constant energy and the semi-major axis of populations of events from ^{129m}Xe, ^{131m}Xe, and ^{127}Xe. Best Energy resolution occurs where this measure is minimum.

normalized both the measured angular offset and the measured offset from known energy by their observed maximums in this space.

From this combined estimator we estimate the best g_1 and g_2 values for maximizing our fractional resolution,

$$g_1 = 0.14 \quad g_2 = 7.2. \tag{5.2.12}$$

We refer to the energies produced by this choice of g_1 and g_2 as primed energies (E') to note they are different from physical energy discussed in the next section. Here no estimate of the error bars on these values of g_1 and g_2 are calculated as they are only used to make cuts to identify event populations for methods discussed below and not for any actual energy reconstruction in LUX.

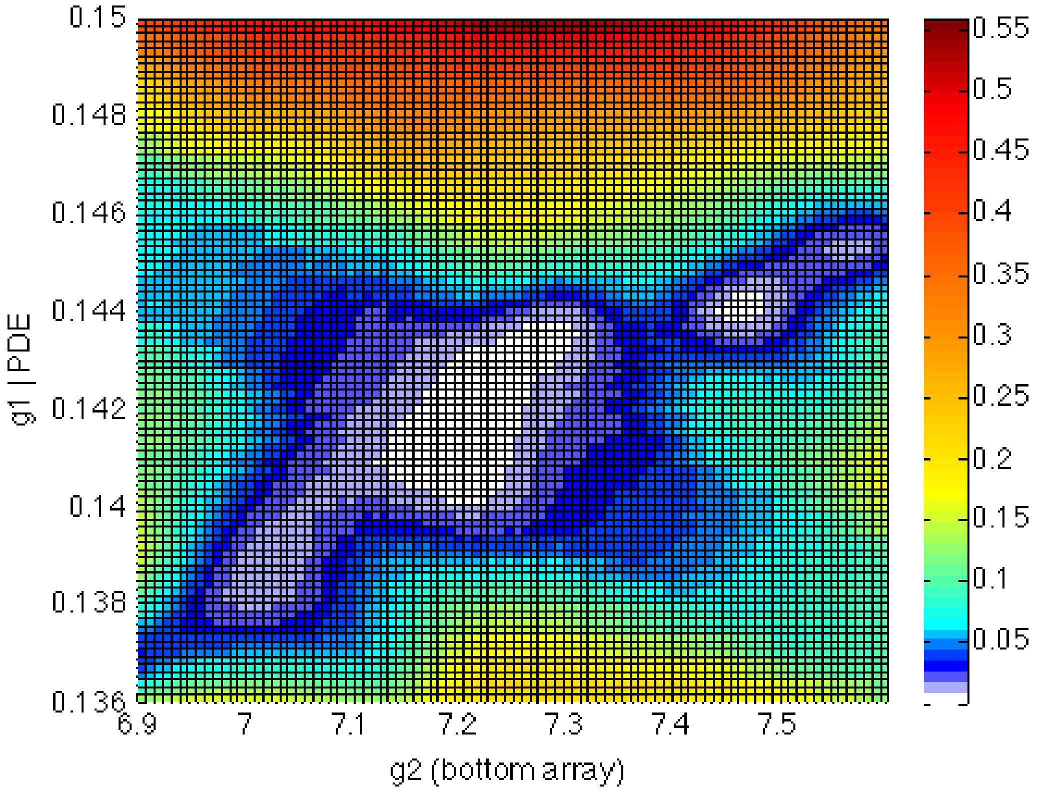

FIGURE 5.2: Normalized measure of the convolution of the cumulative angular offset between a line at a single energy value and the semi-major axis of populations of events, figure (5.1), and the normalized accuracy of the reconstructed mean energy of the event populations relative to their known, true energies. Best energy resolution occurs where this measure is minimum.

Using these values of g_1 and g_2 we make final versions of the underlying space diagram from fiducialized background events, $(E' > 7keVee)$, in the WIMP search data, figure (5.3). Having done this we clearly separate the populations of events from ^{131m}Xe at 163.9 keV and from the combination of lines at 236.8 keVee from ^{127}Xe and ^{129m}Xe, as well as identifying additional lines at 208.3 and 408 keV from ^{127}Xe.

Here the feature at 408 keV is the result of a 375 keV decay of the ^{127}I daughter of ^{127}Xe followed by a cascade of X-rays or Auger electrons. The initial capture electron that results in the production of the ^{127}I daughter comes from the K shell with 85% probability, resulting in 33 keV average additional observed energy from the Ka and Kb shell in combination, or the L shell with a 12% probability of a cascade of 5.2 keV averaged additional observed energy[87]. Note that the 208.3

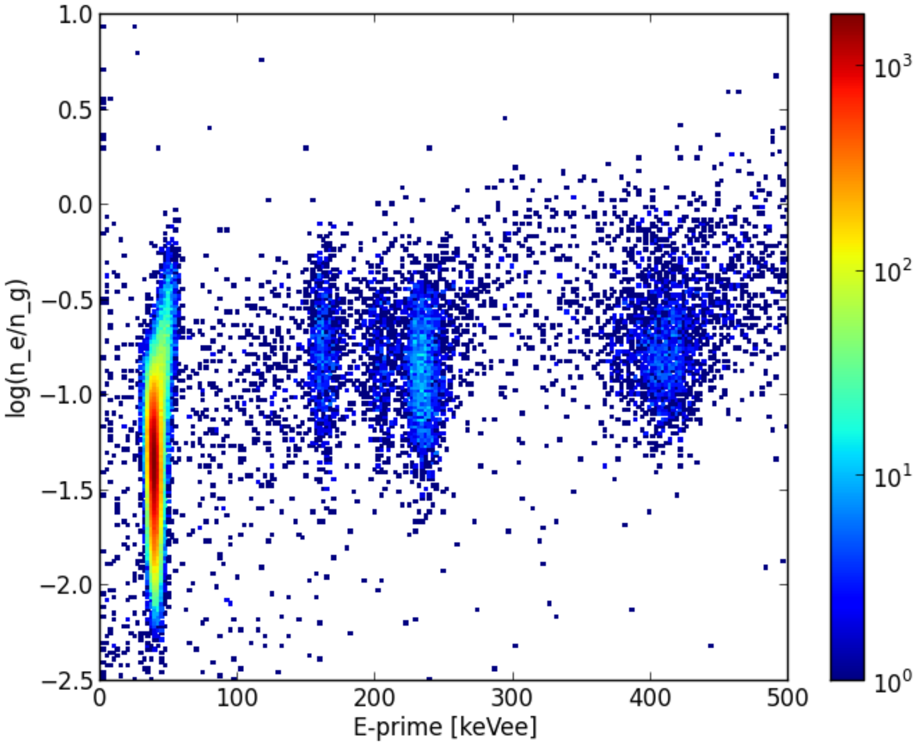

FIGURE 5.3: Density plot (log color scale) of event populations observed in the 85.3 live day data from ^{83m}Kr, ^{127}Xe, ^{129}Xe, and ^{131}Xe reconstructed with g_1=.142 and g_2 = 7.22 (bottom array only). Clear separation between populations of mean energy 163.9 keV, 208.3 keV, 236.8 keV, and 408 keV are resolved.

keV line is the result of a 203 keV decay followed by a 5.2 keV L shell cascade or higher shell cascades with E $\leq$ 1.2 keV. The corresponding decay followed by a K shell cascade is absorbed into the population of events at 236.8 keV, which is analyzed separately.

5.2.2 Simulation Based Determination of g_1 and g_2

The simplest approach to solving our problem of finding physical g_1 and g_2 for the LUX detector is to take a simulation package based on historical measurements in previous detectors to estimate the mean predicted number of photons and electrons, as a function of event energy. Comparison between these predictions and the measured S1 and S2 spectra resulting from a series of known mono-energetic lines in the detector allow us to directly estimate g_1 and g_2 using equations (5.2.1) and (5.2.2).

Such a simulation package was developed for LUX, called LUXSim, based upon GEANT4 and a series of published fundamental measurements of xenon response, the Noble Element Simulation Technique (NEST) library [88], [83], [85]. Using NEST, which gives predicted mean number of quanta produced at specific fields and energies, we compare the predicted number of quanta as a function of energy to the observed mean S1 and S2 signals generated, extracting g_1 and g_2 for each source before computing a mean expected value across all sources.

Source	**Energy [keV]**	**Decay Type**	**Fiducialization**
^{83m}Kr	41.5 [32.1 and 9.5]	Internal Conversion	$r < 15$ cm
^{131m}Xe	163.9	Internal Conversion	$r < 15$ cm
^{127}Xe	203 or 375	^{127}I daughter γ-emission	$r < 15$ cm
	33.8	Kb shell X-ray	
	5.3	L shell X-ray	
	≤ 1.2	Higher shell X-ray	
^{129m}Xe	236.1	Internal Conversion	$r < 15$ cm
^{137}Cs	661.6	Photo-absorption peak of ^{137m}Ba Internal Conversion from ^{137}Cs beta decay	$r < 20$ cm

Table 5.1: Table of sources, energies, decay types, and fiducialization used for the LUX experiment energy calibration. Variation in the fiducial cut used were required for external sources to preserve event populations with enough statistics for analysis. Data from [87] and [89].

Sources used are summarized in table (5.1). For each source, we use the resolution-weighted energy reconstruction discussed in section (5.2.1) to identify events from that sub-population within the data. We then perform a series of cuts for data cleanliness, requiring single scatter events for all sources. For uniform sources, events must also be reconstructed within a fiducial volume around the center of the detector, radius < 15 cm, and between 10 and 35 cm in depth, as we wish to examine the fiducial response. As the ^{137}Cs is an external source we use identical single-scatter and z-cuts but impose much weaker radial cuts, radius < 20 cm, to combat the self-shielding of the xenon and keep enough events in the population to make statistically significant measurements. From this sub-sample of events, we find the mean and standard deviation of the population numerically in S1 and

S2. We fit a normal distribution to the histogram of the S1 and S2 spectra, fitting only events that fall within two standard deviations of the computed mean, figures (5.4) and (5.5), respectively.

Having obtained a new mean and standard deviation for the population from the fitted gaussians, which mitigate outlier events that pass the previously listed, we then compare to the mean number of quanta for an event of the energy of interest using an interpolated NEST estimate of the number of produced quanta at the event site. Interpolation over the NEST library data is done using a two-dimensional cubic-spline across field and energy, to account for the LUX drift field (181 V/cm) and the energy of each source. Taking the ratio of the measured raw S1 and S2 signals in photoelectrons to these predictions we form estimators of g_1 and g_2 value at each energy, figure (5.6). Here the error bars include the statistical error on finding the mean S1 and S2 size in photoelectrons as well as the published 4% systematic error on the NEST estimates. No treatment of systematics that may result from interpolation to a field of 181 V/cm or to energies of the sources is done. Estimation of these systematics is challenging as no further data has been published near the LUX field. To avoid these systematics we instead seek a non-simulation backed method in section (5.2.3) to estimate the unified gains.

From this analysis we extract mean, energy-independent estimators of g_1 and g_2 of:

$$g_1 = 0.147 \pm 0.003 \quad g_2 = 6.2 \pm 0.1. \tag{5.2.13}$$

We compute the mean as a weighted average with weights, $w_i = \sqrt{1/\sigma_i^2}$, finding these values in good agreement with the g_1 from our resolution weighted energy reconstruction parameters, section (5.2.1) but find the estimator of the true g_2 to differ from what gives best resolution.

However, these simulation backed values are subject to several systematics. First, they rely heavily on the accuracy of interpolation over the historical data, mainly from [65], and so inherit any systematics inherent to that data. Of specific concern is the accuracy of the applied field under which the data were taken, especially at low fields, such as the LUX operational field, where fringe fields in the experimental

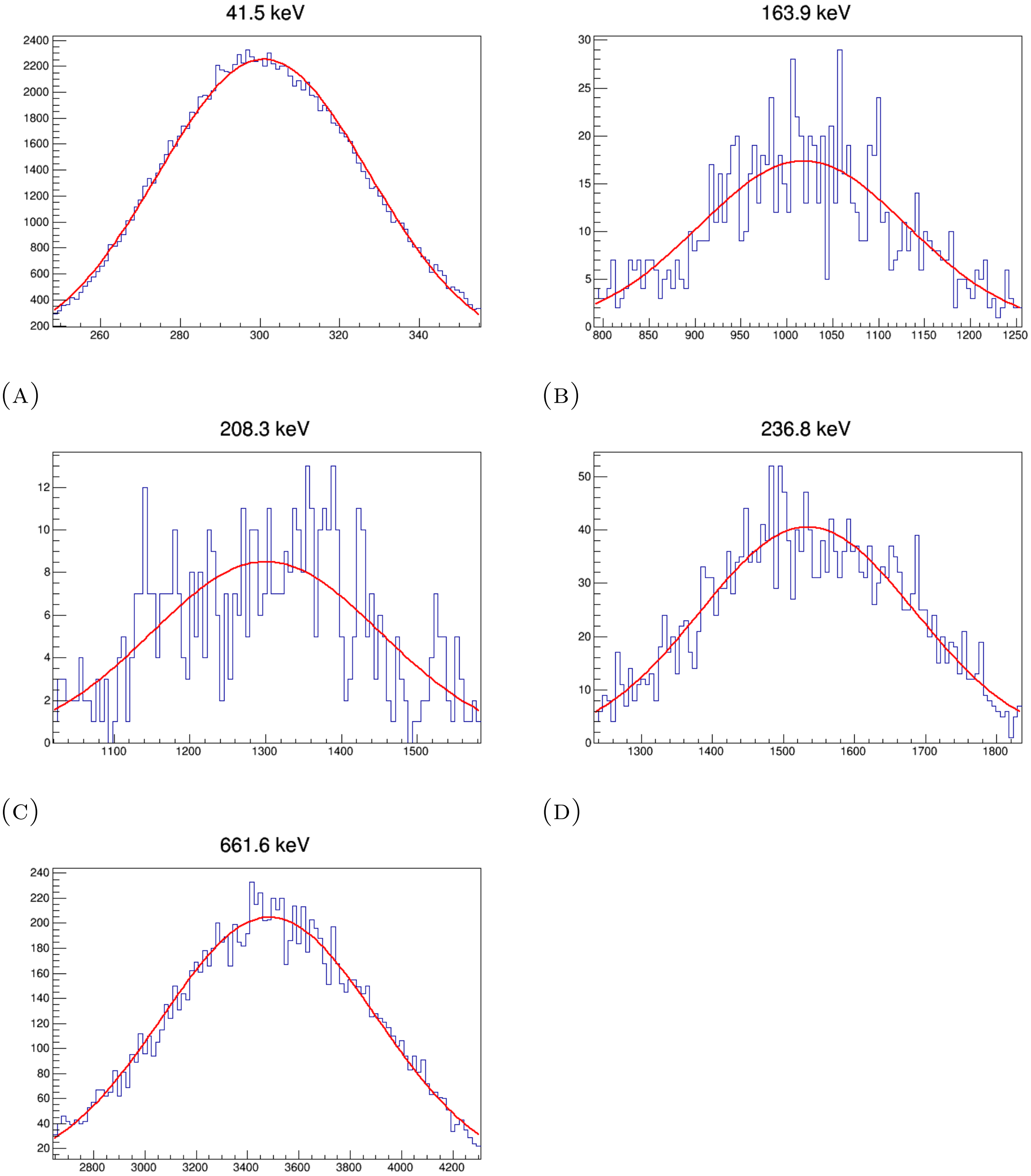

(A)

(B)

(C)

(D)

(E)

FIGURE 5.4: Gaussian Fits to histograms of S1 size [in photoelectrons] for events from [a] 41.5 keV ^{83m}Kr decay, [b] 163.9 keV ^{131m}Xe, [c] 208.3 keV ^{127}Xe (with L-shell X-ray cascade), [d] 236.8 keV from combination of ^{129m}Xe and ^{127}Xe (with k-shell X-ray cascade), [e] 661.6 keV photo-abosorption peak from ^{137}Cs. Gaussian fits are done to data passing the cuts outlined in the text and within two numerically computed standard deviations of the computed mean for each population.

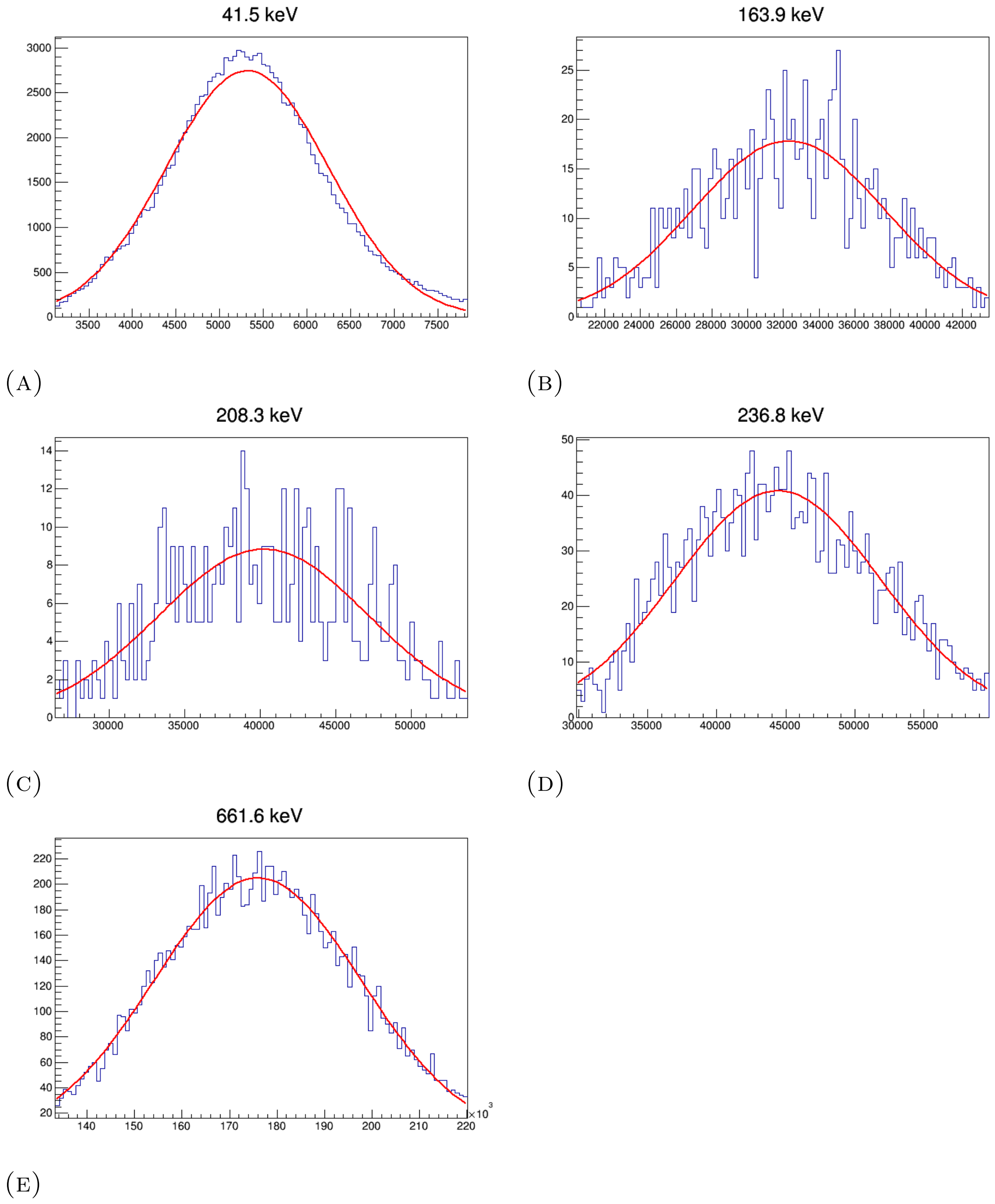

(A)

(B)

(C)

(D)

(E)

Figure 5.5: Gaussian Fits to histograms of S2 size [in photoelectrons] for events from [a] 41.5 keV ^{83m}Kr decay, [b] 163.9 keV ^{131m}Xe, [c] 208.3 keV ^{127}Xe (with L-shell X-ray cascade), [d] 236.8 keV from combination of ^{129m}Xe and ^{127}Xe (with k-shell X-ray cascade), [r] 661.6 keV photo-abosorption peak from ^{137}Cs. Gaussian fits are done to data passing the cuts outlined in the text and within two numerically computed standard deviations of the computed mean for each population.

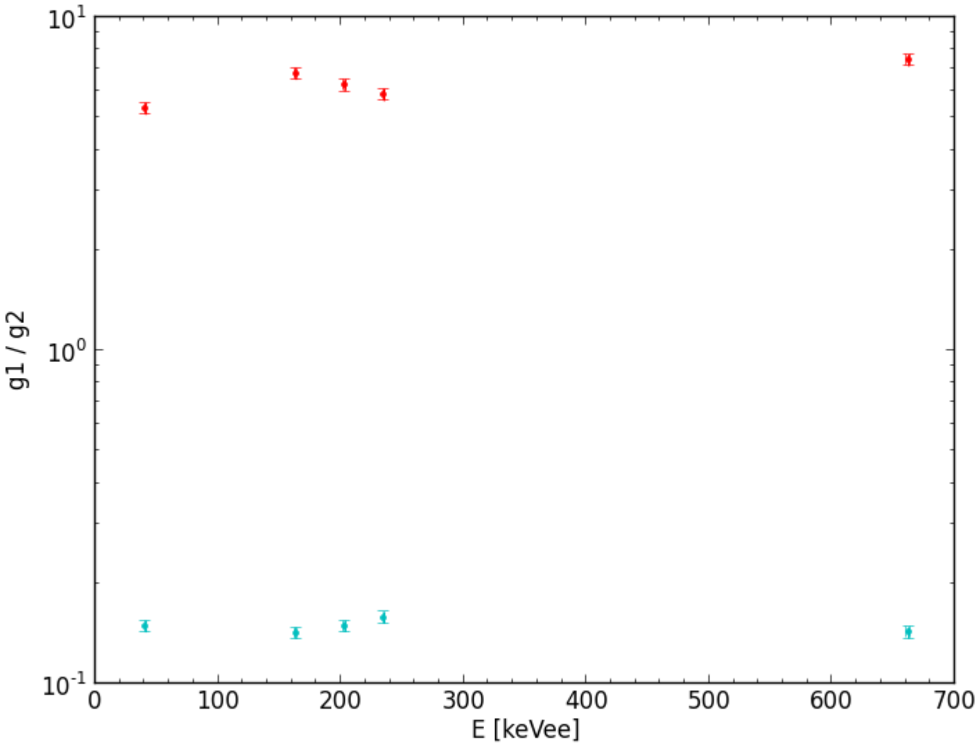

FIGURE 5.6: Estimates of g_1[cyan] and g_2[red] from comparison of ^{83m}Kr, ^{127}Xe, ^{129}Xe, and ^{131}Xe to an interpolation across historical data [83]. Error bars include statistical errors as well as reported 4% systematic error on NEST predictions but do not include systematics related to field or energy interpolation, which are instead treated by moving to a non-simulation backed estimation in section (5.2.3).

setup's extraction field may have had a large effect. Further, questions arising in section (7.8) related to the calibration of the single photo-electron size for VUV photons as compared to LED calibration present challenges that require retuning the NEST parameters. To partially mitigate these two systematics we now attempt to extract g_1 and g_2 from the raw data without simulation comparison.

5.2.3 Data Based Determination of g_1 and g_2

Having considered the previous two methods of estimating g_1 and g_2 from the LUX data, we present a third method, based on historical treatments but applied in a new way. This method will alleviate some of the systematics expected from the simulation based method, by avoiding interpolating drift field regions where xenon response has never been measured. To do this we use the combined energy relation, equation (5.2.3), along with our global estimator of the xenon work function, W = 13.7±0.3 eV, which should be robust against systematics due to its independent verification from multiple experiments [83], to extract values for g_1 and g_2 based on the combined energy equation, (5.1.4).

While historically, a similar method has been performed using a single mono-energetic source and varying the applied field to vary the scintillation and ionization response of the xenon media [84], [65], here we use the data from the mono-energetic sources of table (5.1) but at constant field. Using multiple sources at different energies, we probe different mean recombination fractions and thus different scintillation and ionization yields in the xenon media, substituting variation in applied field for variation in event energy. Using the non-linear response of the xenon versus energy allows us to extract g_1 and g_2 from the x and y intercepts of our data in the space of S1/E vs. S2/E, as these intercepts directly relate to g_2/W and g_1/W. This can bee seen most clearly from equation, (5.1.4), which we use to derive two new equations:

$$S2/E = \frac{n_e}{(n_e + n_\gamma)} \cdot \frac{g_2}{W} \text{ and} \tag{5.2.14}$$

$$S1/E = \frac{n_\gamma}{(n_e + n_\gamma)} \cdot \frac{g_1}{W}, \tag{5.2.15}$$

where $\frac{n_e}{(n_e+n_\gamma)}$ is the ionization yield of the xenon and $\frac{n_\gamma}{(n_e+n_\gamma)}$ is the scintillation yield. The y-intercept of a line in the space of S1/E vs S2/E corresponds to $n_e = 0 \rightarrow S2/E = g_2/W$, and correspondingly the x-intercept of our line corresponds to $n_\gamma = 0 \rightarrow S1/E = g_1/W$.

Having outlined our method, we now perform identical fitting as described in section (5.2.2) with all cuts held constant so that all event populations are identical. Plotting our mean S1 and S2 signals divided by the known energy of each feature, as shown in table (5.1), we first fit the data using orthogonal distance regression (odr). As there will be strong covariance among the slope and intercepts we

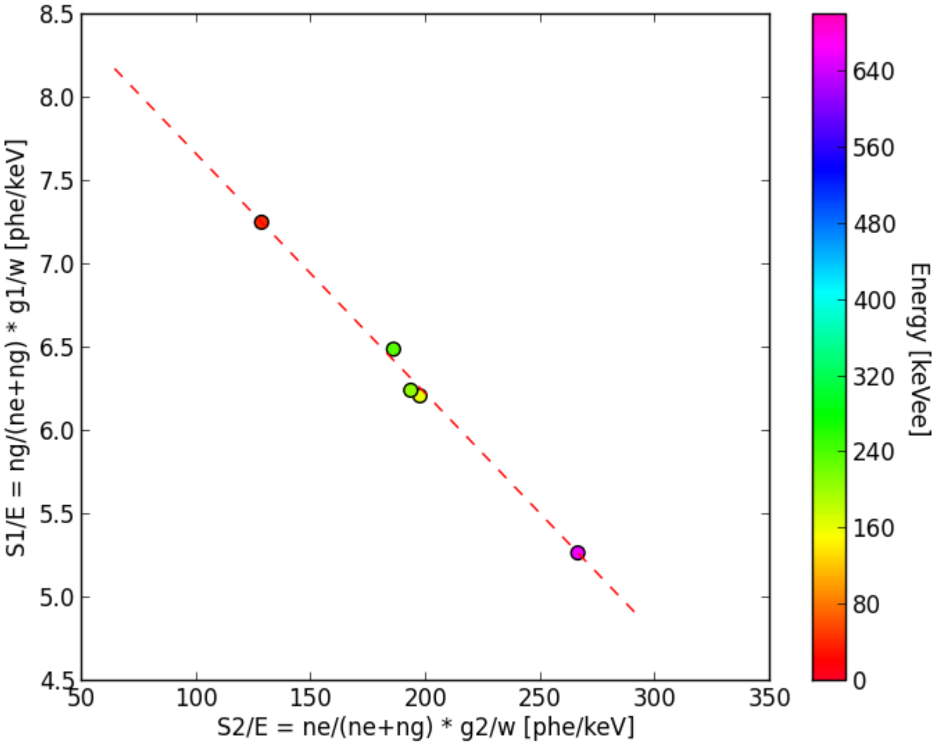

FIGURE 5.7: Ratio of mean S2 signal divided by true source energy [keV] versus S1 signal divided by true source energy [keV] for ^{83m}Kr, ^{127}Xe, ^{129}Xe, ^{131}Xe, and ^{137}Cs colored by reconstructed energy of the source in keVee. Errorbars are the size of the points. Best fit line from orthogonal distance regression is plotted [dashed-red] corresponding to $g_1 = 0.125 \pm 0.003$ and $g_2 = 8.7 \pm 0.2$.

then perform a Markov-Chain Monte-Carlo (MCMC) taking the odr estimators as initial seeds to the MCMC. Here the MCMC used an affine invariant walkers algorithm [90] with 100 walkers distributed in a small 2-D Gaussian ball around the initial solution parameters, figure (5.7). From this fit we then find best fit values of g_1 and g_2 to be:

$$g_1 = 0.125 \pm 0.003 \quad g_2 = 8.7 \pm 0.2. \tag{5.2.16}$$

The error bars reported are the result of MCMC, after allowing a burn in period of 50 steps, figure (5.8), taking into account the errors on the data as well as covariance in the fit, figure (5.9). We find clear discrepancy between the values of g_1 and g_2 found using this method and the previous simulation-based method. While the observed differences could be due to historical field uncertainty or systematic errors resulting from interpolation to unknown fields, it could also be the result of the photoelectron size bias which we discuss in chapter 7. We take these "data-centric" values of g_1 and g_2 as being less biased as they lack any systematic effects from field interpolation. We also note this method provides the most robust picture of g_1 and g_2 for work in the next chapter as it likely also partially mitigates effects of the single photoelectron size bias, as we use high-energy data to recalibrate, reconstructing high energy population energies accurately.

While changes in g_1 and g_2 after the data reprocessing discussed in section (7.8) will have some affect on the measured value of recombination fluctuations as a function of energy, we proceed with the methodology in chapter 6, with the intention of a paper describing the final results, [91], expected in Fall 2014, after a full reprocessing of the first WIMP search is completed.

5.3 Summary

Having now concluded our investigation into the energy calibration of LUX, in the next chapter we examine what causes the observed variation about the mean for events from mono-energetic sources and equivalently what sets the band-width in detectors of this class, outlining a method for deconvoling fundamental event site fluctuations from measurement fluctuations in S1 and S2 signals.

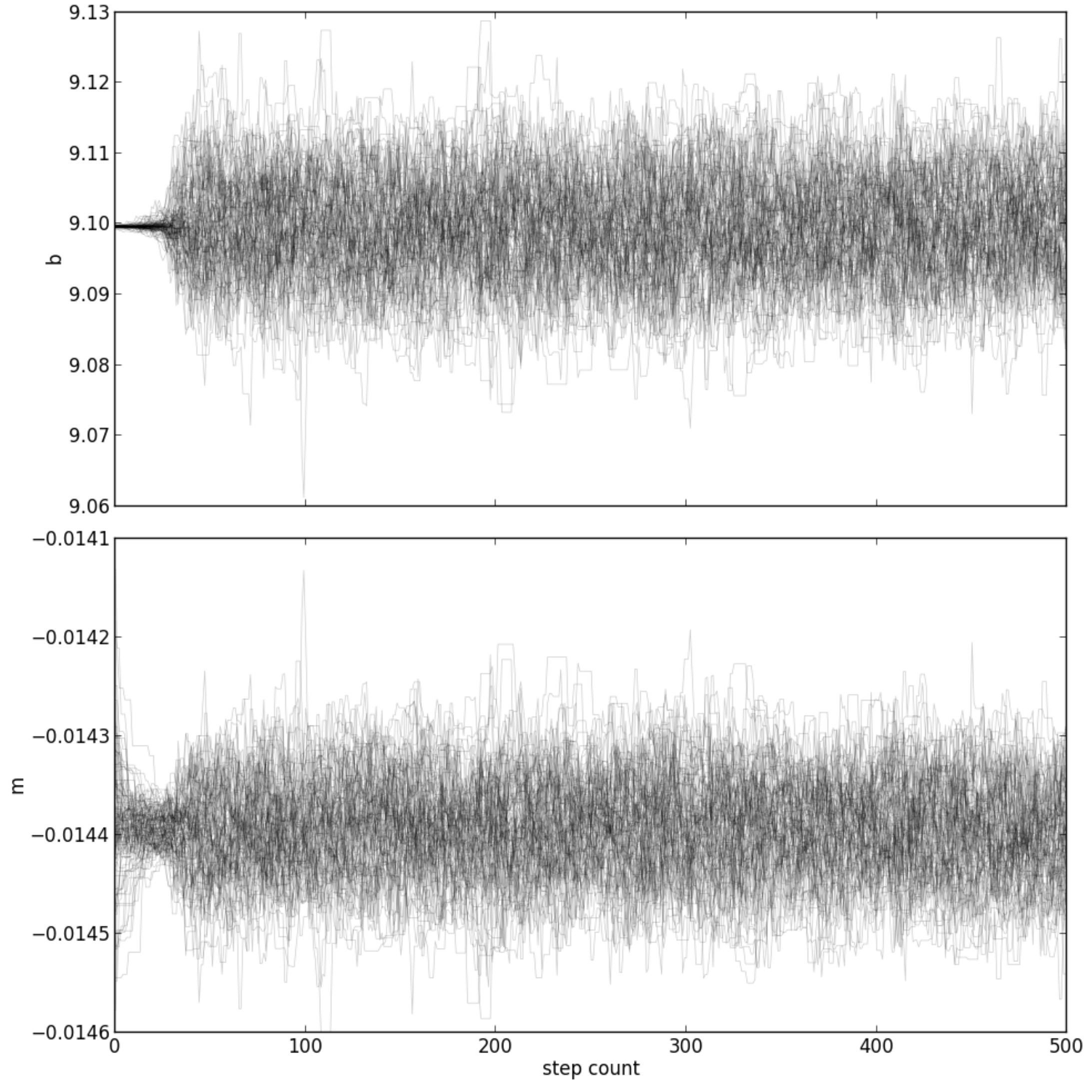

FIGURE 5.8: Markov-Chain Monte Carlo estimates of the values of the slope, m, and intercept, b, with respect to number of steps in the chain. Walkers were started in a small 2-D gaussian ball around initial parameter estimates obtained from an orthogonal-distance-regression estimation. Reported error bars are taken from positions after step 50, allowing initial "burn-in."

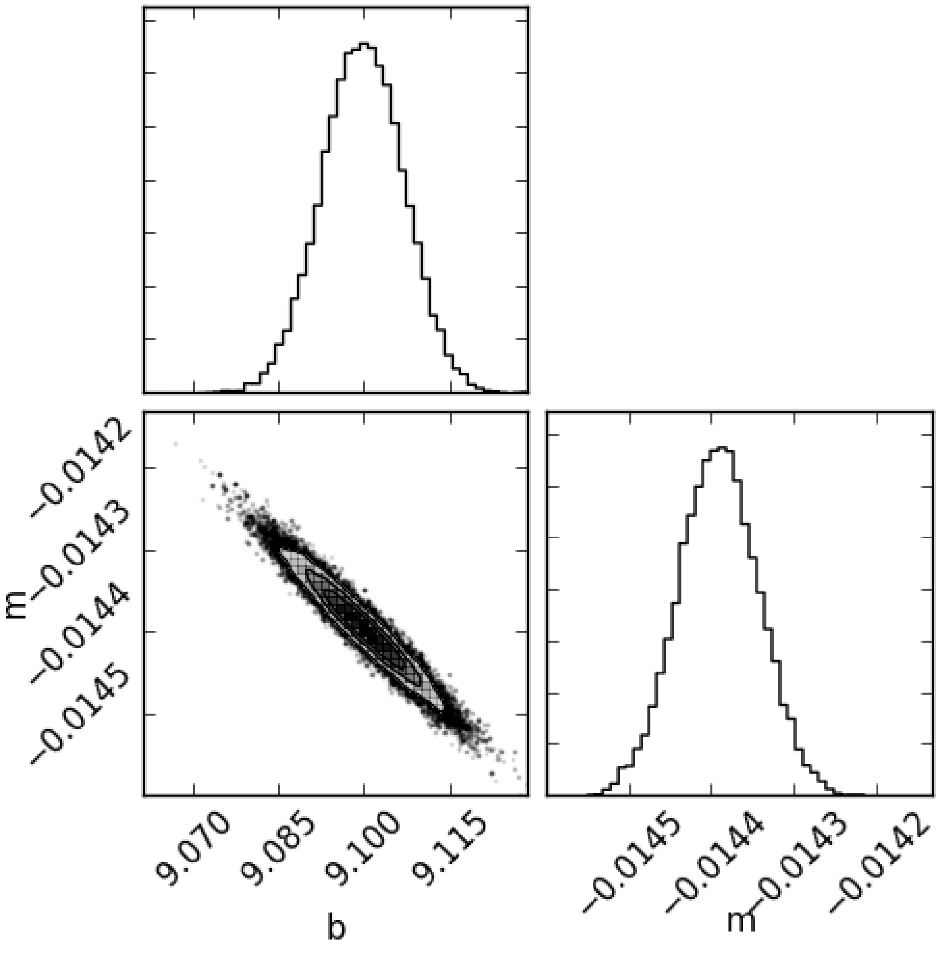

FIGURE 5.9: Observed variances and covariance for fit to data in figure (5.7). m is the slope of our estimated line and b is its y-intercept. Quantities are calculated after initial “burn-in” period show in figure (5.8).

Chapter 6

Event Level Fluctuations in LUX

We now turn to an examination of what underlies the discrimination power of liquid xenon TPCs or equivalently what sets our ability to discriminate WIMP candidate events from background events, by examining the width of the electron-recoil band in the LUX detector as a function of energy. A "band" being defined as the region of space populated by electron recoils in $\log(\mathrm{n}_e/\mathrm{n}_\gamma)$ or equivalently log(S2/S1). We take our g_1 and g_2 values from chapter 5 and examine event-site and detector measurement based fluctuations, where these fluctuations give rise to location of individual events away from the means of their distributions. We perform a deconvolution of broad-energy spectral data from a combination of tritiated-methane and ^{137}Cs sources from derived functional forms of S1 and S2 measurement fluctuations based upon mono-energetic high-energy ($E > 40$ keV) features. We conclude with a measurement of the fluctuations present at the event site as a result of event-by-event changes in the fraction of electrons that recombine, outlining a method to extract intrinsic xenon response as a function of energy. From this we determine that while at the lowest energies, measurement fluctuations dominate our discrimination abilities, at higher energies, recombination becomes the dominant fluctuation limiting electron recoil discrimination.

6.1 Fundamental Fluctuations

Having now outlined the determination of g_1 and g_2, the energy reconstruction parameters described in chapter 5, we examine the size and shape of event populations from both mono-energetic lines and broad spectrum data, deconvolving event fluctuations into three pieces: two pieces resulting from uncorrelated fluctuations in the S1 signal and S2 signal measurement process and a third piece from the amount of recombination that occurs at the event site. By fluctuation, we mean a measured difference between an individual event and the mean for events of its type. We expect S1 and S2 signal to vary on an event-by-event basis as different numbers of photons from the event site may be collected or uncorrected detector inhomogeneities might arise, ripples on the liquid xenon surface, for example. We also expect variations in the number of electrons that recombine as these are ruled by statistical processes, likely dependent on the exact track geometry at the event site. We expect S1 and S2 measurement fluctuations to be uncorrelated, with the two signals resulting from very different production mechanisms. For recombination fluctuations we expect perfect anti-correlation. recombination maps from one electron to one photon and our energy depends on the sum of the number of quanta, equation (5.1.4).

We begin by examining how uncorrelated fluctuations in measured S1 and S2 signal move an event from the mean of its event population in the space of $\log(\mathrm{n}_e/\mathrm{n}_\gamma)$ versus reconstructed energy. This space is chosen as it allows us to separate event populations that would be difficult to separate fully in 1-D. Work is done in terms of quanta from the event site, n_γ and n_e, for clarity on the micro-physics, as compared to S1 and S2 signals [in photoelectons] as used in chapter 7. Both quantities are equivalent up to a constant. We write the units of n_γ and n_e as $[\mathrm{n}_\gamma]$ and $[\mathrm{n}_e]$, respectively.

An event-level fluctuation in the measurement process of an S1 will result in larger or smaller S1 signal as compared to the mean of its population, resulting in a change in the measured $\log(\mathrm{n}_e/\mathrm{n}_\gamma)$ and the reconstructed energy for that event. For example, if, due to measurement fluctuations in event i, the loss of one $[\mathrm{n}_\gamma]$ occurred, we would expect the event to differ from the mean of its population in $\log(\mathrm{n}_e/\mathrm{n}_\gamma)$ by:

$$log(n_e/n_\gamma)_i = log\left(\frac{\langle n_e\rangle}{\langle n_\gamma\rangle - 1}\right) - log\left(\frac{\langle n_e\rangle}{\langle n_\gamma\rangle}\right), \tag{6.1.1}$$

and will result in a shift in reconstructed energy of:

$$E_{i,reconstructed} = \langle E\rangle - W. \tag{6.1.2}$$

Similarly, for an event in which the measured S2 signal fluctuated to less S2 signal, equivalent to one [n$_e$], we would observe a shift of

$$log(n_e/n_\gamma)_i = log\left(\frac{\langle n_e\rangle - 1}{\langle n_\gamma\rangle}\right) - log\left(\frac{\langle n_e\rangle}{\langle n_\gamma\rangle}\right), \tag{6.1.3}$$

and

$$E_{i,reconstructed} = \langle E\rangle - W. \tag{6.1.4}$$

Thus, in our chosen space, fluctuations in measured S1 and S2 signal both result in a shift in measured event location in both log(n$_e$/n$_\gamma$) and reconstructed energy. We contrast this to fluctuations at the event site in the amount of recombination, which map $n_e \rightarrow n_\gamma$ on a one-to-one basis as described in section (5.1.1). For a fluctuation of this type, where one extra electron recombines, as compared to the mean number of recombining electrons for the population, we expect to observe a difference of:

$$log(n_e/n_\gamma)_i = log\left(\frac{\langle n_e\rangle - 1}{\langle n_\gamma\rangle + 1}\right) - log\left(\frac{\langle n_e\rangle}{\langle n_\gamma\rangle}\right). \tag{6.1.5}$$

However, we expect to observe no corresponding shift in the reconstructed energy, as from equation (5.1.4) we observe the reconstructed energy of the event is only dependent on the sum of the number of quanta produced at the event site, not the number of electrons or photons independently. Thus, fluctuations in each of these three channels move events in three different directions; fluctuations in measured S1 signal moving events along lines of constant S2, and vice-versa, while fluctuations in the recombination fraction moving events along lines of constant energy.

Working in the space of $\log(\mathrm{n}_e/\mathrm{n}_\gamma)$ versus reconstructed energy, we deconvolve uncorrelated fluctuations in the measurement of S1 and S2 signals from intrinsic recombination fluctuations using our knowledge of the different effects of these fluctuations on the shape of the population. We do this work in two steps: first for a set of mono-energetic sources and then using broad spectrum data from tritium and cesium-137.

6.2 Mono-Energetic Source Measurement of S1 and S2 Fluctuations

Figure (6.1) shows events from mono-energetic energy depositions recorded during the first half of the 85.3 live-day WIMP search in a fiducial volume of radius 15 cm and between z of 10 and 35 cm. Event selection also required events to be single scatters with reconstructed energy between of 0 and 500 keVee and within the limit of $-2.5 < \log(\mathrm{n}_e/\mathrm{n}_\gamma) < 1$. Here, we reconstruct energy using the data-based g_1 and g_2 values found in section (5.2.3). Distinct populations resulting from the various decays of ^{83m}Kr, ^{129m}Xe, ^{131m}Xe, and ^{127}Xe, as described in table (5.1), are observed within the data. To deconvolve the three types of fluctuations described above, we fit to the populations centered around 41.5, 163.9, 208.3, and 236 keV using bivariate normal distributions. Fitting is done using maximum likelihood methods with populations identified using the resolution-based energy reconstruction described in section (5.2.12).

We seek a relation between the parameters defining a bivariate normal distribution,

$$P(\boldsymbol{x}) = \sqrt{\frac{1}{|2\pi\Sigma|}}e^{-\frac{1}{2}(\boldsymbol{x}-\boldsymbol{\mu})^{\dagger}\cdot\Sigma^{-1}\cdot(\boldsymbol{x}-\boldsymbol{\mu})}, \tag{6.2.1}$$

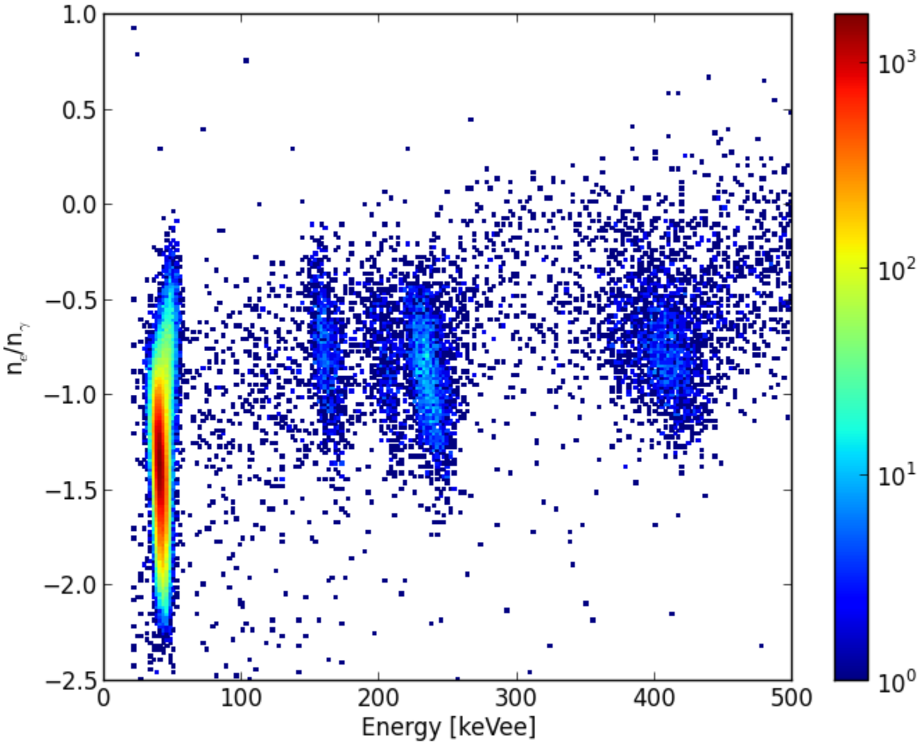

FIGURE 6.1: Density plot of event populations observed in the first half of the 85.3 live day data from ^{83m}Kr, ^{127}Xe, ^{129}Xe, and ^{131}Xe reconstructed with g_1 and g_2 described in section (5.2.3). Events are plotted in log($\mathrm{n}_e/\mathrm{n}_\gamma$) versus reconstructed recoil energy, in keVee as all events are either β's or γ's. Selection of events only identified single scatters within a fiducial volume of r $<$ 15 cm and 10 cm $<$z $<$ 35 cm.

and our three types of fluctuations. Given our combined energy relation we consider small fluctuations in δ_{S1}, δ_{S2}, and δ_R and compute their corresponding shifts in reconstructed energy and log($\mathrm{n}_e/\mathrm{n}_\gamma$), where

$$\delta_E = W\left(\delta_{S1} + \delta_{S2}\right), \text{and} \tag{6.2.2}$$

$$\delta_{log\left(\frac{n_e}{n_\gamma}\right)} = \frac{\delta_{S2} - \delta_R}{n_e} - \frac{\delta_{S1} + \delta_R}{n_\gamma}, \tag{6.2.3}$$

using the relations that $\delta_{n_e} = \delta_{S2} - \delta_R$ and $\delta_{n_\gamma} = \delta_{S1} + \delta_R$. From which we can derive the elements of our covariance matrix

$$\Sigma_{E,E} = \left\langle \delta_E^2 \right\rangle = W^2 \left(\sigma_{S2}^2 + \sigma_{S1}^2 \right), \tag{6.2.4}$$

$$\Sigma_{log\left(\frac{n_e}{n_\gamma}\right), log\left(\frac{n_e}{n_\gamma}\right)} = \left\langle \delta^2_{log\left(\frac{n_e}{n_\gamma}\right)} \right\rangle = \frac{\sigma_{S2}^2}{n_e^2} + \frac{\sigma_{S1}^2}{n_\gamma^2} + \left(\frac{1}{n_e} + \frac{1}{n_\gamma} \right)^2 \sigma_R^2, \text{ and} \tag{6.2.5}$$

$$\Sigma_{E, log\left(\frac{n_e}{n_\gamma}\right)} = \left\langle \delta_E \delta_{log\left(\frac{n_e}{n_\gamma}\right)} \right\rangle = W \left(\frac{\sigma_{S2}^2}{n_e} - \frac{\sigma_{S1}^2}{n_\gamma} \right), \tag{6.2.6}$$

where we have used the independence of the three types of fluctuation, $\langle \delta_i \delta_j \rangle = 0$ for $(i/j) \in \{S1, S2, R\}$ and $i \neq j$ [65].

With these relations we construct our bivariate normal distributions by fitting the underlying populations, figure (6.2), and find the 1-sigmoid contours of the bivariate normal distributions for the populations from activated xenon and the corresponding deconvolution into constituent fluctuations at the 1-σ level for each source.

An identical analysis is performed on the 661.6 keV ^{137}Cs photo-absorption peak and the 41.5 keV ^{83m}Kr decay. From these analyses we fit a functional form for the size of S1 and S2 fluctuations as a function of reconstructed mean number of quanta in the event population, figure (6.3).

Error bars in figure (6.3) are dominated by systematic errors resulting from uncertainties in the values of g_1, g_2 and W, and were estimated by varying across the one sigma values of all three parameters simultaneously. Statistical error bars from fitting are also shown but are the size of the points or smaller for all measurements. Statistical error bars were found by taking an initial estimate from the root HESSE algorithm, a finite-difference algorithm to compute the Hessian matrix. This estimate is then used as an initial seed to a MCMC. The MCMC used affine invariant walker algorithms [90] with 100 walkers distributed in a small 5-D Gaussian ball around the initial maximum likelihood solution parameters. Example resulting variances and covariances from the MCMC for ^{83m}Kr are shown in

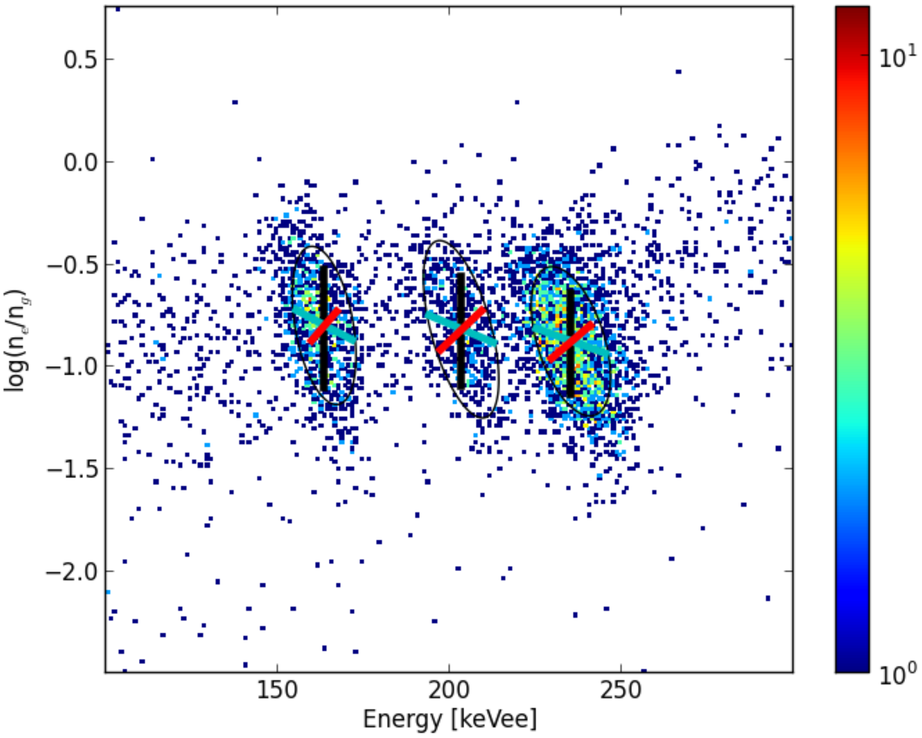

FIGURE 6.2: Density plot of event populations from activated xenon observed in the first half of the 85.3 live day data, as described in figure (6.1). Black ellipses are the 1-sigmoid contours from bivariate normal fits to underlying activated xenon populations. Also shown are de-convolved one sigma fluctuations in S1 [cyan], S2 [red], and recombination [black]. Note the different directions of dispersion resulting from each separate constituent fluctuation.

figure (6.5). We allow a burn-in period of 500 steps for the walkers, with the walkers positions over the total 2000 steps shown in figure (6.4). Here we have chosen ^{83m}Kr as an example because it shows the largest shift in derived fit parameters from the original HESSE solutions of any of the populations used.

Fitting of S2 and S1 measurement variance, σ^2_{S1} and σ^2_{S2}, is done using a model in which these fluctuations are functions of number of quanta produced at the event site in the related channel:

$$\sigma^2_{Si} = A_i + B_i * n_i + C_i * n_i^2, \tag{6.2.7}$$

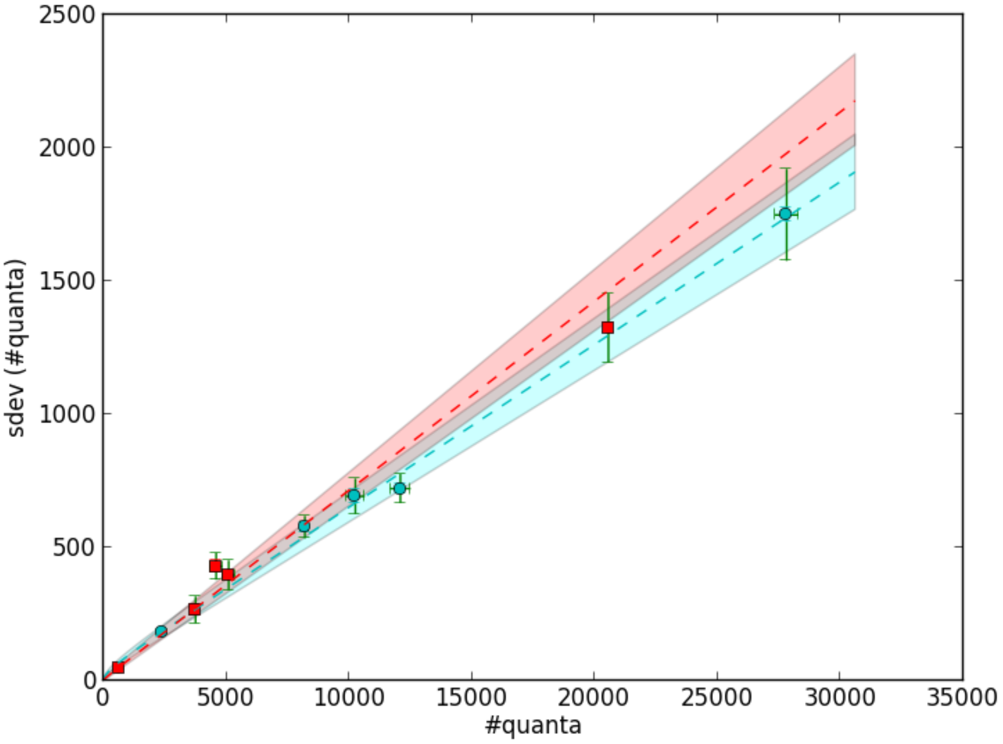

FIGURE 6.3: Measured one sigma size of S1 [cyan] and S2 [red] fluctuations (in number of quanta) versus the reconstructed number of quanta in that channel. Also shown are fits for S1 [dashed-cyan] and S2 [dashed-red] using the functional forms outlined in the text and 1-sigma limits for S1 [shaded-cyan] and S2 [shaded-red]. Green error bars shown are the sum of statistical and systematic error bars, where the systematic uncertainty comes from varying W, g_1, and g_2 within their one-sigma constraints described in section (5.2.3) for g_1 and g_2, and [83] for W. Statistical error bars from fitting are also shown in corresponding color (cyan or red) but are smaller than or equivalent in size to the points for all measurements.

where coefficients $A_i, B_i,$ and C_i arise from effects such as baseline noise, binomial fluctuations on the number of collected quanta, and uncorrected detector inhomogeneity respectively. In practice, both S1 and S2 fluctuations were fit without a constant term, $\sigma^2_{S_i}(n_i = 0) = 0$, as baseline fluctuations are expected to be extremely small in comparison to signal size, [70].

These functional forms for S1 and S2 measurement fluctuations break observed fluctuations into statistical, growing as $\sqrt{n_i}$ or “instrumental” growing as n_i. These statistical fluctuations in S1 and S2 signal arise in both channels from variation in

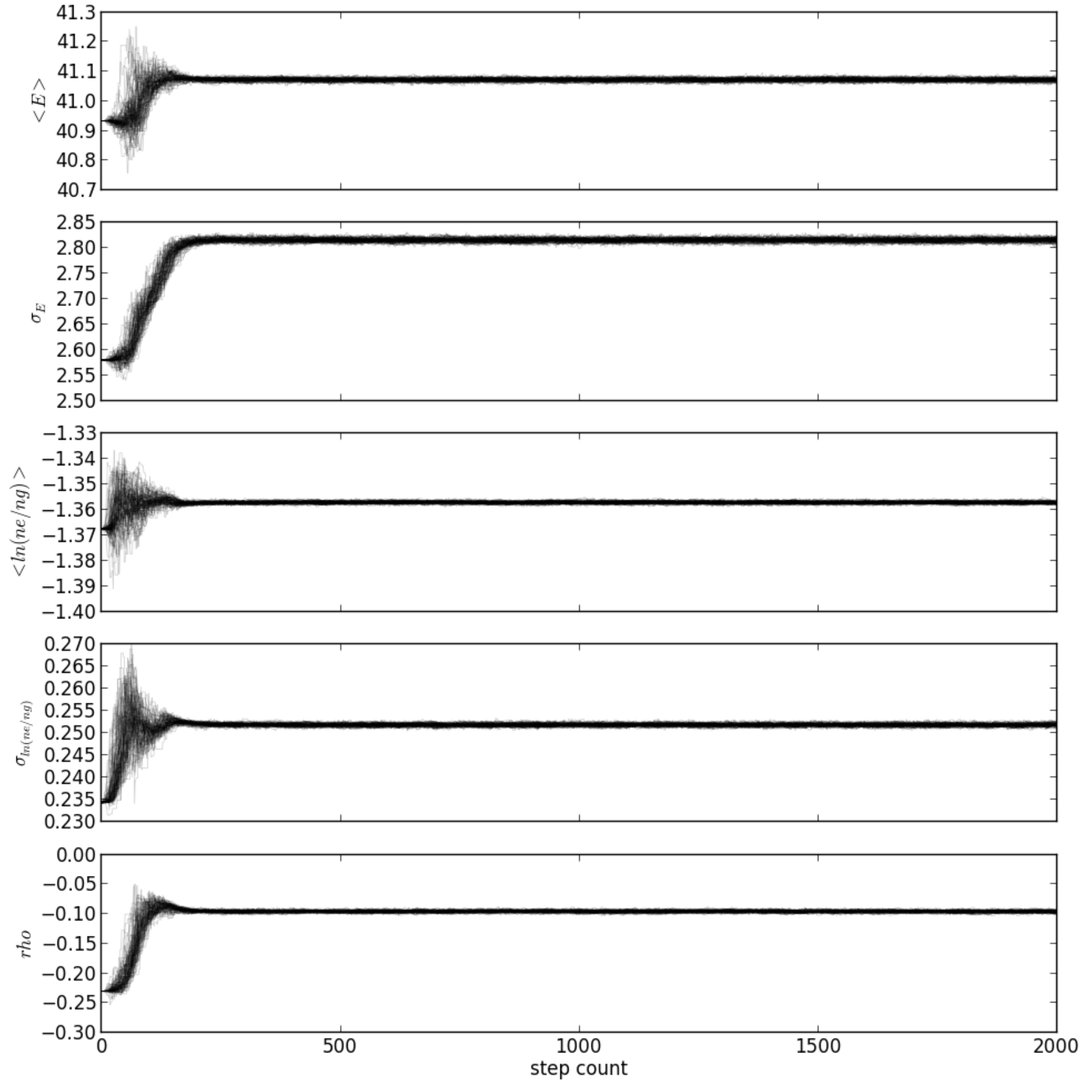

FIGURE 6.4: Relative position of the 100 walkers after each step in the Markov-Chain Monte-Carlo. Final parameter estimates, as in figure (6.5) used only parameter values found after an initial "burn-in" period of 500 steps.

the single photo-electron response, with an additional term in S1 fluctuations from the binomial process of light collection. S2 statistical fluctuations are the result of binomial fluctuations in electron extraction due to incomplete extraction efficiency, the result of low extraction fields obtainable in LUX. From our knowledge of these underlying processes we can estimate the expected statistical fluctuations in each channel, finding:

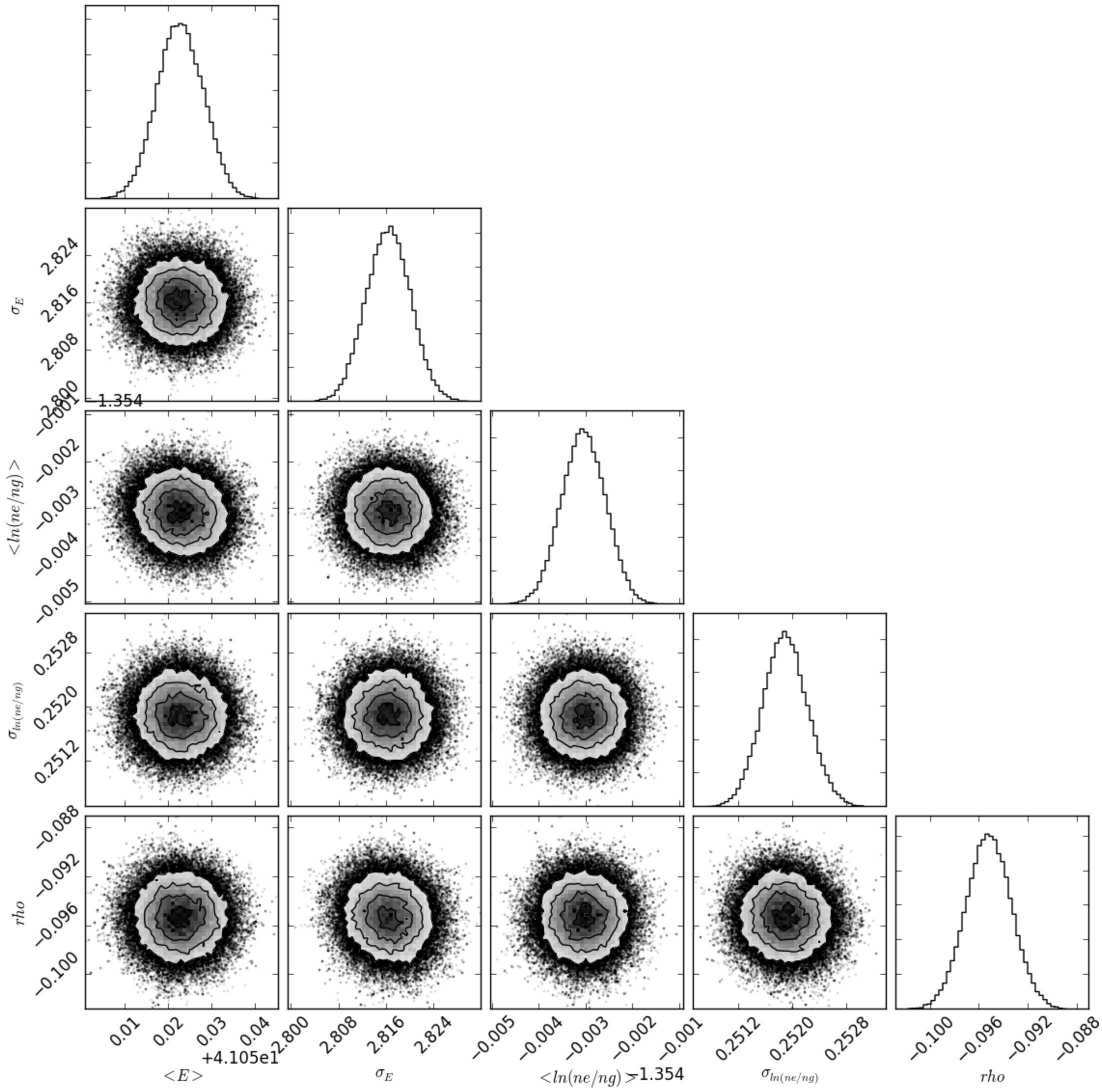

FIGURE 6.5: Parameter estimates, variances, and covariances for bivariate normal fit to the ^{83m}Kr event population from Markov-Chain Monte-Carlo. MCMC used 100 affine invariant walkers initially seeded in a small 5-D guassian ball of parameters space centered on initial parameters estimates found from numerical computation of the Hessian matrix.

$$\sigma^2_{S1,\text{statistical}} = \frac{1 - g_1 + \sigma^2_{sphe}}{g_1} n_\gamma, \text{ and} \tag{6.2.8}$$

$$\sigma^2_{S2,\text{statistical}} = \left((1-\epsilon)\epsilon + \frac{1 + \sigma^2_{sphe}}{g_2} \right) n_e, \tag{6.2.9}$$

where σ^2_{sphe} is the measured variance in the single photo-electron size and ϵ is the electron extraction efficiency (eee). From $\epsilon = 0.7 \pm 0.1$ [81], and $\sigma_{sphe} = .341 \pm 0.07$ [92], we estimate:

$$\sigma_{S1,\text{statistical}} = (2.82 \pm 0.08)\sqrt{n_\gamma} \tag{6.2.10}$$

and

$$\sigma_{S2,\text{statistical}} = (0.58 \pm 0.03)\sqrt{n_e}. \tag{6.2.11}$$

From these fits for S1 and S2 fluctuations we obtain:

$$\sigma_{S1} = (2.2 \pm 0.53) \cdot \sqrt{n_\gamma} + (6.168 \pm 0.004)/100 \cdot n_\gamma \tag{6.2.12}$$

and

$$\sigma_{S2} = (1.0 \pm 0.84) \cdot \sqrt{n_e} + (7.099 \pm 0.005)/100 \cdot n_e, \tag{6.2.13}$$

finding agreement with our estimated parameters, equations (6.2.10) and (6.2.11), at the 1σ level. We can now take these functional forms for S2 and S1 measurement fluctuations and examine the observed variance in broad-band data, the beta spectrum from an injected tritiated-methane source and the Compton scatter spectrum from the ^{137}Cs source. From these we will deconvolve the strength of recombination fluctuations as a function of energy.

6.3 Tritium and ^{137}Cs

Taking our measured functional size of S1 and S2 fluctuations as a function of reconstructed number of quanta at the event site in each channel, we now measure both the mean recombination fraction and the size of recombination fluctuations as a function of energy. We make use of two calibration sources, an external ^{137}Cs source, which is placed in a source-tube outside the vacuum shielding of LUX, as described in section (3.10), and an injected tritiated tethane source.

Tritiated methane was used in the LUX experiment because the detector is the first liquid-noble dark matter detector large enough to require an internal *in situ* calibration of its electron recoil band to overcome the intrinsic self-shielding of the xenon. Tritiated methane is injected into the fluid stream, and swept into the active region with the circulating xenon following the path described in section (3.7). This source provides high-statistics calibration data of low-energy ($E_{max} <$ 18 keV) beta decays uniformly in the active volume [47], [93]. Here we will outline the method using the tritiated methane data before presenting results from both spectra, as all methods are identical unless explicitly stated otherwise.

Figure (6.6) shows the event population from an injection of tritiated methane. As we are faced with a finite amount of data, we slice the data into discreet bins in energy and fit for the mean and variance in each bin. While this gives a mean that is the centroid value in the bin, it systematically inflates the observed variance if the centroid is not constant across each bin. To avoid this effect we construct a smooth centroid from the data and then subtract it from the observed spectra, working in centroid subtracted space, using the process described in appendix A.

We construct the centroid estimator by cutting the data into bins of 0.5 keVee [20 keVee for the ^{137}Cs due to lower statistics] requiring at least 1000 events in each bin. We iteratively fit the band population in each bin with a one-dimensional Gaussian, extending to $\pm 2\sigma$, until a stable value of the measured variance in each bin is found. The centroid is then estimated by using a smoothing, interpolated, univariate spline of degree 4 between the mean values. Having obtained a first estimator of the centroid, we subtract the centroid and then iterate over the entire process until we have found a stable value for the overall shift in the location of the

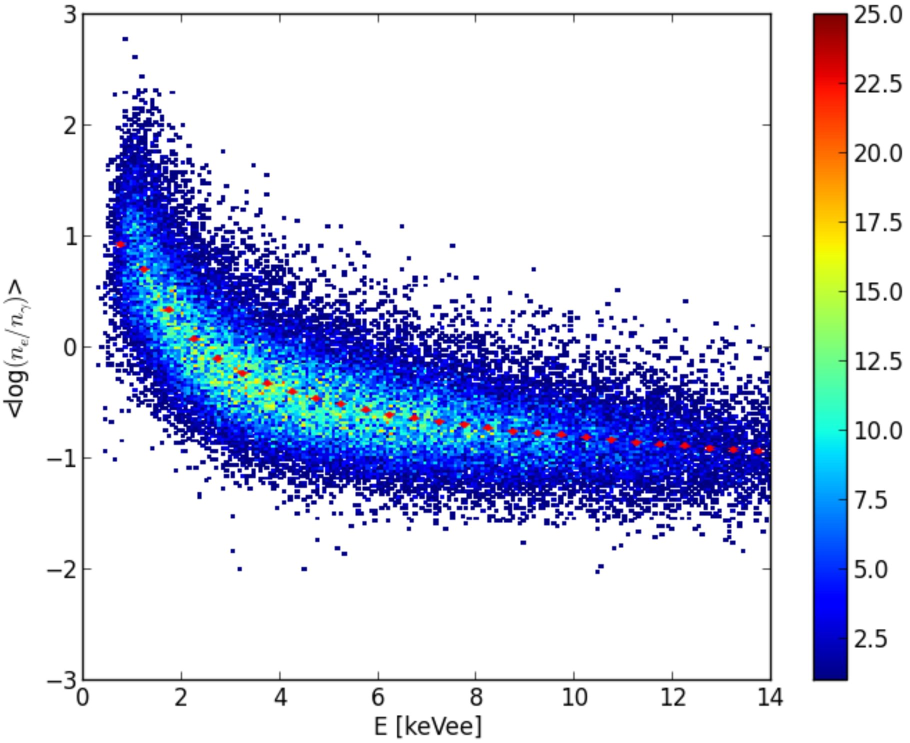

Figure 6.6: Histogram of log(n_e/n_γ) versus energy for tritiated methane. Also shown are the mean values found [red] for use in centroid subtraction. We refer to the varying mean as a function of energy as the centroid in this text.

centroid, normally after 2-3 iterations, resulting in the centroid subtracted band as shown in figure (6.7).

To quantify the expected shift in the observed variance due to any inaccuracy in estimating the true centroid, equation (A.2.2), we compute the centroid again using an un-smoothed spline through the values, estimating $\delta[\mu]$ from the difference between these two centroid estimates as the true $\delta[\mu]$ is unknown. We find this effect to be smaller then the statistical 1σ error bars on the data points, figure (6.8).

From our centroid-subtracted band, we measure the variance in each bin, and compare to the predicted variance from S1 and S2 fluctuations as found in section (6.2), figure (6.9). The error bars on the as-measured variances are statistical error bars and the width of the shaded bands are due to the systematic error on g_1, g_2,

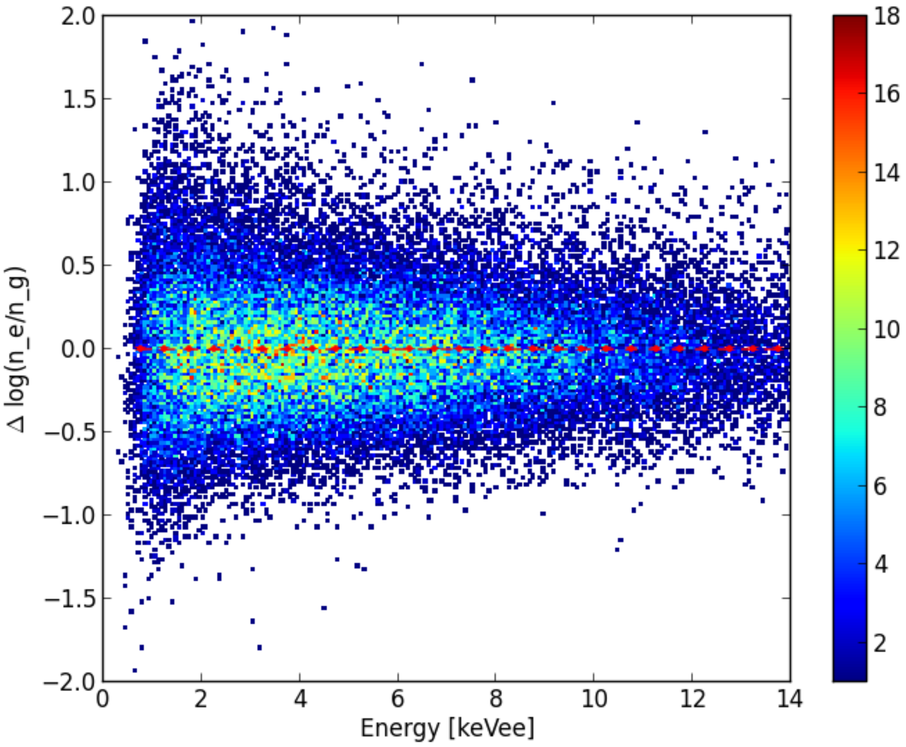

FIGURE 6.7: Histogram of $\log(n_e/n_\gamma)$ versus energy for tritiated methane after centroid subtraction. Centroid subtracted data is used for variance measurement as it mitigates effects due to changes in the mean of the population internal to bins in energy, which would otherwise contribute to observed variance.

and W. We infer the strength of recombination fluctuations at the event site, as making up the remaining observed variance in each bin.

Using this method, we can also find the mean recombination fraction, r, from section (5.1) in each bin of energy, figure (6.10), using the relationship between r and the ionization yield:

$$r = 1 - \left(\frac{a}{b}\frac{N_{ex}}{N_{ion}} + 1\right)\left(\frac{n_e}{n_e + n_\gamma}\right), \tag{6.3.1}$$

and assuming $a = b = 1$ and $N_{ex}/N_{ion} = 0.06$ from theoretical calculations [94].

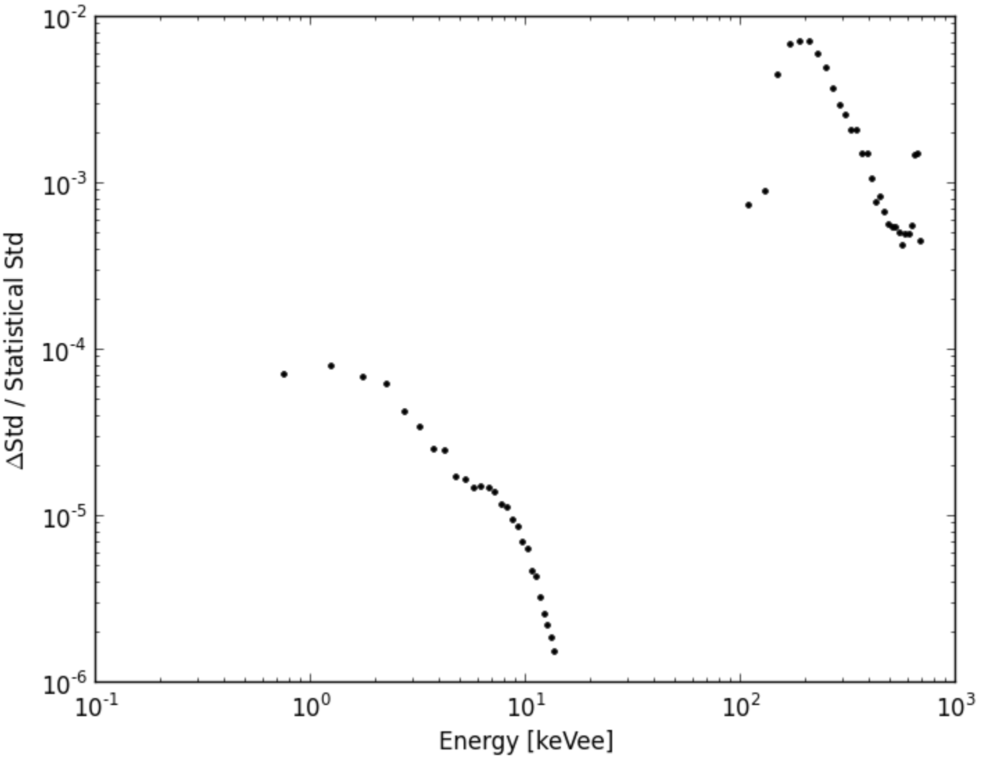

Figure 6.8: Ratio of the estimated change in the standard deviation through the calculation of $\delta[\mu]$. as a function of energy. While the true $\delta[\mu]$ is unknowable, we compare the fit used, a smoothed spline, to a spline with no smoothing to estimate the possible effect. Ratio is found to be significantly less than one all all energies, implying the change in variance is small compared to already established error bars.

6.4 Recombination Fraction and Fluctuations Versus Event Energy

Performing an identical analysis on the ^{137}Cs, we compute the size of fluctuations in recombination as a function of energy, figures (6.11) and (6.12), we find that the strength of recombination fluctuations grows as a function of energy.

Oscillations in predicted strength of S1 and S2 measurement fluctuations in the highest energy bins of the ^{137}Cs data are due to the beginnings of breakdown in the accuracy of the estimation of the derivative of the underlying band, which is one

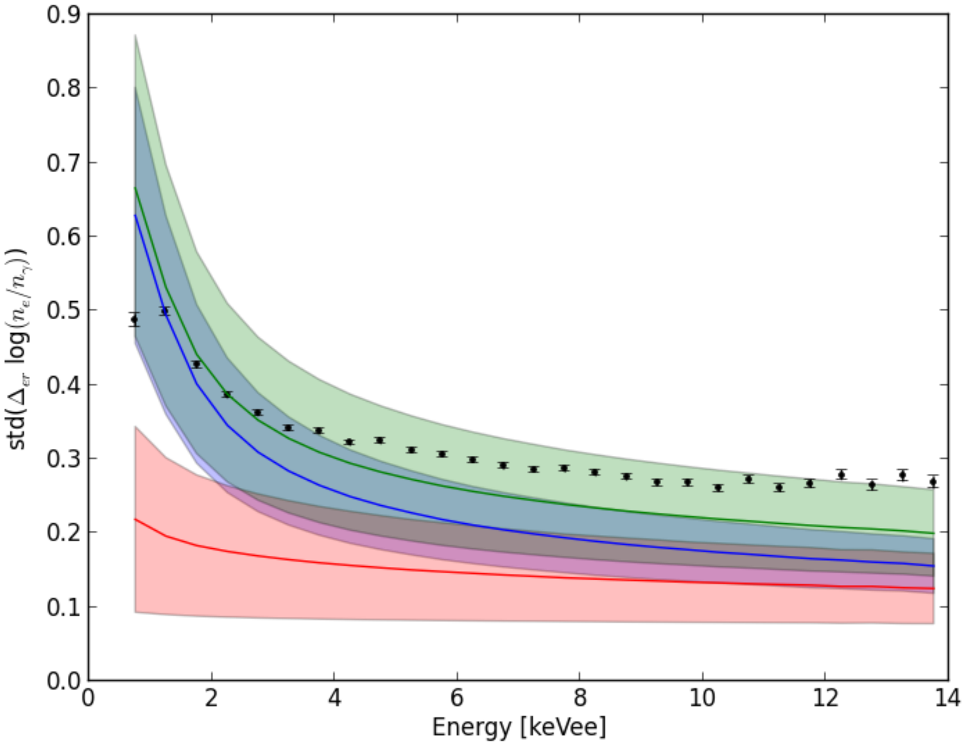

FIGURE 6.9: Measured one sigma fluctuation size [black] observed in the energy spectrum data from tritiated methane as compared to predicted strength of S1 [blue] and S2 [red] measurement fluctuations from section (6.2) and their sum [green]. Error bars on measured points are 1σ statistical error bars, while shaded contours on predicted S1 and S2 fluctuations are 1σ systematic error bars dominated by uncertainty in the values of g_1, g_2 and W. Residual fluctuations observed are due to fluctuations in the amount of recombination at the event site.

of the assumptions underlying our ability to deconvolve the the band analytically, described fully in appendix A.

As the size of recombination fluctuations is the result of underlying differences in the physical track geometry for each event, the rate of energy dependence might be expected to follow a binomial distribution, $\sigma_R \propto \sqrt{n}$, as we expect an underlying binomial process for each recombining ion/electron pair in the track. We find fluctuations growing significantly faster than $\sqrt(E) \propto \sqrt(n)$ as a function of energy, confirming earlier results as measured from ^{57}Co [65].

We also note one other prominent feature in the data, with important implications,

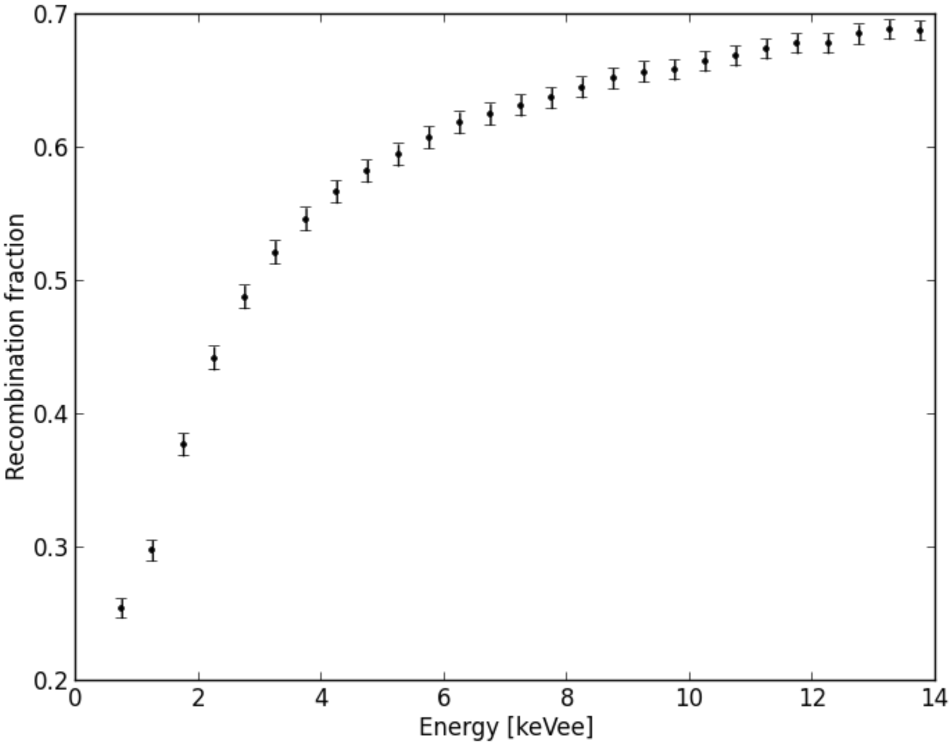

FIGURE 6.10: Measured mean recombination fraction as a function of event energy from tritiated methane. Mean recombination fraction ,r, is calculated using equation (6.3.1) and is the mean amount of recombination experienced by events of a given energy, equation (5.1.2).

recombination fluctuations, which dominate at higher energies, are observed to "turn-off" for small energy events. With S1 measurement fluctuations becoming the dominant fluctuation below $E \sim 4$ keVee and completely dominant by $E = 2$ keVee. Combining this with equation (6.2.8), the dominant statistical fluctuation in the measurement of S1 is the result of binomial light collection:

$$\sigma^2_{S1,LC} = \frac{1-g_1}{g_1}\, n_\gamma. \tag{6.4.1}$$

From this result we infer that light collection, as parameterized by the g_1 is the parameter that dominates the discrimination power of this class of detectors at the lowest energies. As light-collection also dominates the thresholds for finding events, as will be seen in chapter 7, it is of the utmost importance for determining

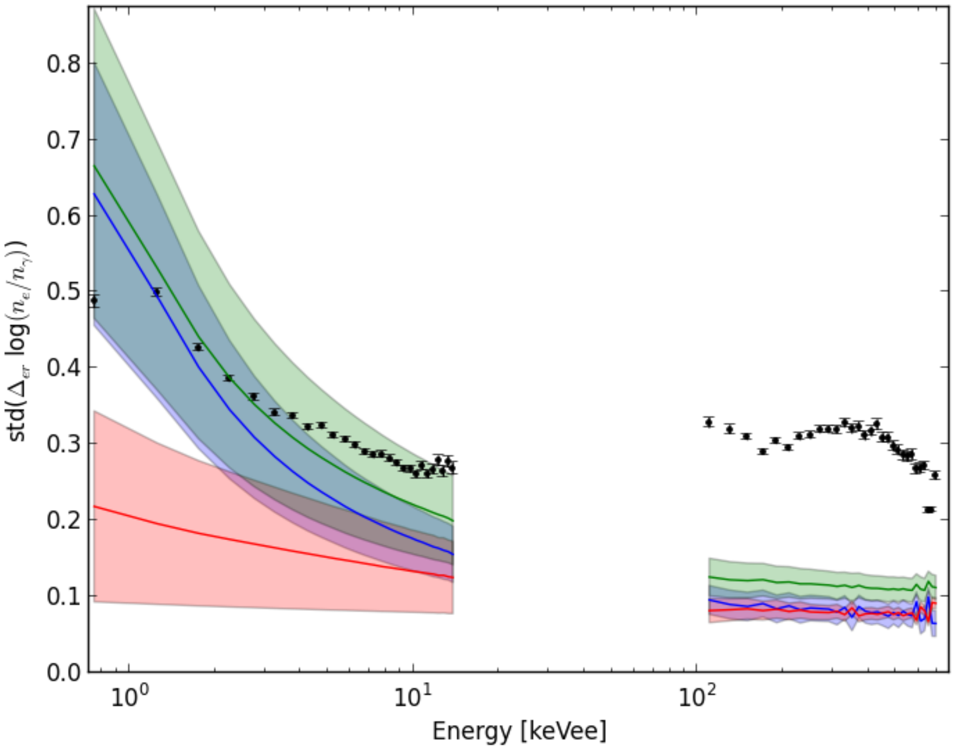

FIGURE 6.11: Measured one sigma fluctuation size [black] observed in the energy spectrum data from ^{83m}Kr and ^{137}Cs as compared to predicted strength of S1 [blue] and S2 [red] measurement fluctuations from section (6.2) and their sum [green]. Error bars on measured points are statistical, while shaded contours on predicted S1 and S2 fluctuations are from systematic uncertainty in the values of g_1, g_2 and w. Residual fluctuations observed are due to fluctuations in the amount of recombination at the event site. The gap from 14 keVee to ∼100 keVee is due to the lack of statistics in the datasets to fulfill the required 1000 event criteria.

the sensitivity of this class of detector, especially to the weak signals expected for low-mass WIMP candidates.

At present an underlying model for the physics behind the size of recombination fluctuations does not exist, however results soon to be published in [95] may illuminate this topic. Further treatment of this work in the face of the systematics discussed in chapter 7 is also needed to account for possible shifts in g_1 and g_2. Though methods outlined in section (5.2.3) are robust in the face of these changes. We expect the publishing of these updates in parallel with this writing, expected in early fall, 2014 [91].

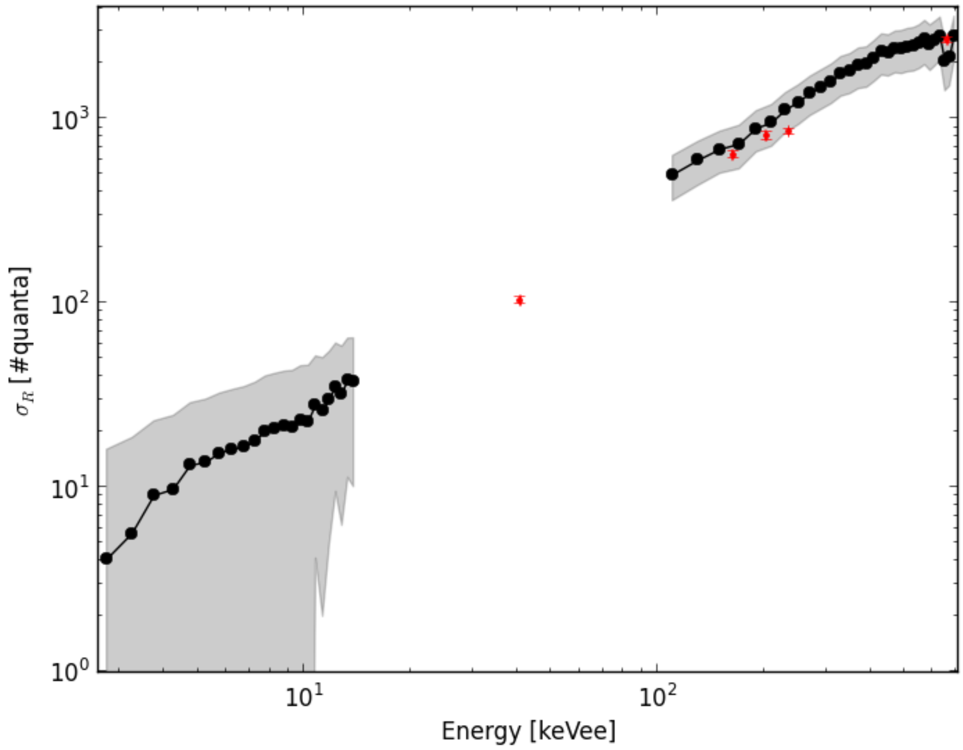

FIGURE 6.12: Measured size of recombination fluctuations as a function of energy [black] with systematic and statistical error [shaded gray]. Points with error bars to values below zero are set to a lower limit of 10^{-4} for plotting purposes. Red points are the size of recombination fluctuations measured using the mono-energetic features described in section (6.2). Recombination fluctuations are seen to grow as a function of energy and "turn-off" at the lowest energies.

6.5 Summary

Having now examined a method for finding the strength of constituent fluctuations, resulting both from uncorrelated fluctuations in the measurement process in S1 and S2, and from fundamental fluctuations at the event site, we have observed that previous measurements of the strength of recombination fluctuations are consistent with those measured in LUX. We now examine the first WIMP search results of the LUX experiment, where we will discuss how energy reconstruction and the intrinsic discrimination power of the LUX experiment lead to the current world-leading result. Finally, we'll discuss next steps both for the LUX related and successor dark matter searches.

Chapter 7

Results From the First WIMP Search in the LUX experiment

Having now reviewed the LUX detector instrumentation and performance in chapters 3 and 4 and examined energy reconstruction and intrinsic fluctuations for the events in chapters 5 and 6 we now examine the results of the first WIMP search, conducted between April and August of 2013. Encapsulating $\sim$ 85 live-days of data taking, this search sets the world's leading limit on the spin-independent WIMP-nucleon cross section. After arriving at the WIMP limit result, we detail next steps both in the LUX program and next generational efforts to pursue dark matter.

7.1 WIMP Search Duration and Diagnostics

As discussed in section (4.1.3), the first WIMP search was conducted between April 21 and August 8 of 2013 in the Davis cavern at the Sanford Underground Research Facility (SURF). After subtracting out dead time due to detector instability (0.8%), a hold-off after large S2 pulses to allow baselines to stabilize (2.2%), and DAQ dead-time (0.2%) the final live-time recorded was 85.3 live-days [47]. This data is analyzed in a non-blind fashion allowing for the rapid dissemination of results through the use of simple data quality cuts.

As discussed previously, detector stability was well established over the duration of the run, with liquid level variation, detector pressure, and detector temperature all controlled within initial performance goals. Due to either observed cross-talk or shorts, three PMTs, two in the upper array and one in the lower, were left unbiased for the duration of the WIMP search. This necessitated the use of only the bottom-array of PMTs to reconstruct S2 [$S2_b$] pulses to avoid the bias in reconstruction of events occurring directly below an unbiased PMT.

Events selection is based on a requirement of single S1 and S2 pairs, both of which are required to fall within a window of 324 μs, the maximum drift-time for the chamber, corresponding to the time required for electrons from an event at the cathode grid to be extracted from the liquid surface.

7.2 Calibrations

Calibrations for the WIMP search are done using a variety of sources: xenon activation lines and ^{83m}Kr, as discussed in chapter 5, tritiated methane, and AmBe and ^{252}Cf for neutron data. The first step in calibration is the measurement of the detector response as a function of three-dimensional position. Here, weekly injections of ^{83m}Kr are used as the krypton disperses uniformly into the active region, providing a uniform map of mono-energetic events. From these mono-energetic events, the LUX detector response is measured as a function of 3D position, and event signals are then normalized to the center of the detector for S1 and to the center of the liquid surface for S2. Krypton injections are done using an automated system designed at Yale with the ^{83m}Kr being injected directly into the circulating xenon fluid stream, discussed previously in section (3.7). After injection, a period of ∼30 minutes is waited to allow for the ^{83m}Kr to homogenize throughout the active region of the detector.

Once calibration of the 3D position response is done, calibration of the electron recoil response is accomplished using tritiated methane injections, which provide robust, electron recoil event populations at low energies throughout the fiducial region. For the calibration of equivalent nuclear recoil response, a combination of

AmBe and ^{252}Cf are used. As both AmBe and ^{252}Cf are external sources, simulation is used to model additional effects that would not be present in a WIMP signal, but are inherent to these sources. Figures (7.1) and (7.2), reproduced from [96], show the simulated AmBe and ^{252}Cf spectra as compared to the data, in addition to the corresponding simulation-backed curve expected for WIMP interactions. Differences between calibration data and expected WIMP recoil spectra result from multiple scatters in the source data as well as unwanted Compton scatters from AmBe and unwanted γ and (n,γ) events from ^{252}Cf [47]. WIMP spectra are simulated individually using the tuned simulation and are dependent on the WIMP mass to determine the expected signal above threshold for a profile-likelihood analysis [47].

Figure (7.3) shows the calibration data used in the first WIMP search to model the electron recoil and nuclear recoil bands. Centroids for each band are shown as solid colored lines (blue/red) with their 90% one-sided confidence intervals [$\pm 1.28\sigma$] plotted as dashed lines. The shape of the electron recoil band shows a distinct “hook” or “kink” upwards below $\sim$ 1.8 keVee, which, from our examination of fundamental fluctuations in chapter 6, we recognize as the energy where measurement fluctuations in S1 become dominant over recombination fluctuations. This change in shape is understood as the change in the direction that the dominant fluctuations cause events to differ from their centroid values.

The final calibration is the energy calibration, discussed in detail in chapter 5, with values of g_1 and g_2 derived from a combination of the sources discussed in chapter 5 and the injectable tritiated methane source discussed in section 6.3. For the first WIMP search the simulation-backed method of determining g_1 and g_2 is used.

In this chapter, we plot results in $\log_{10}(\mathrm{S2}_b/\mathrm{S1})$ versus S1 size in photoelectrons (phe), in comparison to plots in the previous chapters that used $\log(n_e/n_\gamma)$ versus energy. Here the choice to work in $\log_{10}(\mathrm{S2}_b/\mathrm{S1})$ versus S1 results from a desire to make for easier comparison to measurements from the period before energy reconstruction in liquid xenon was fully understood. Where appropriate, energy contours, calculated as described in section (5.1), are provided, labeled in keVee

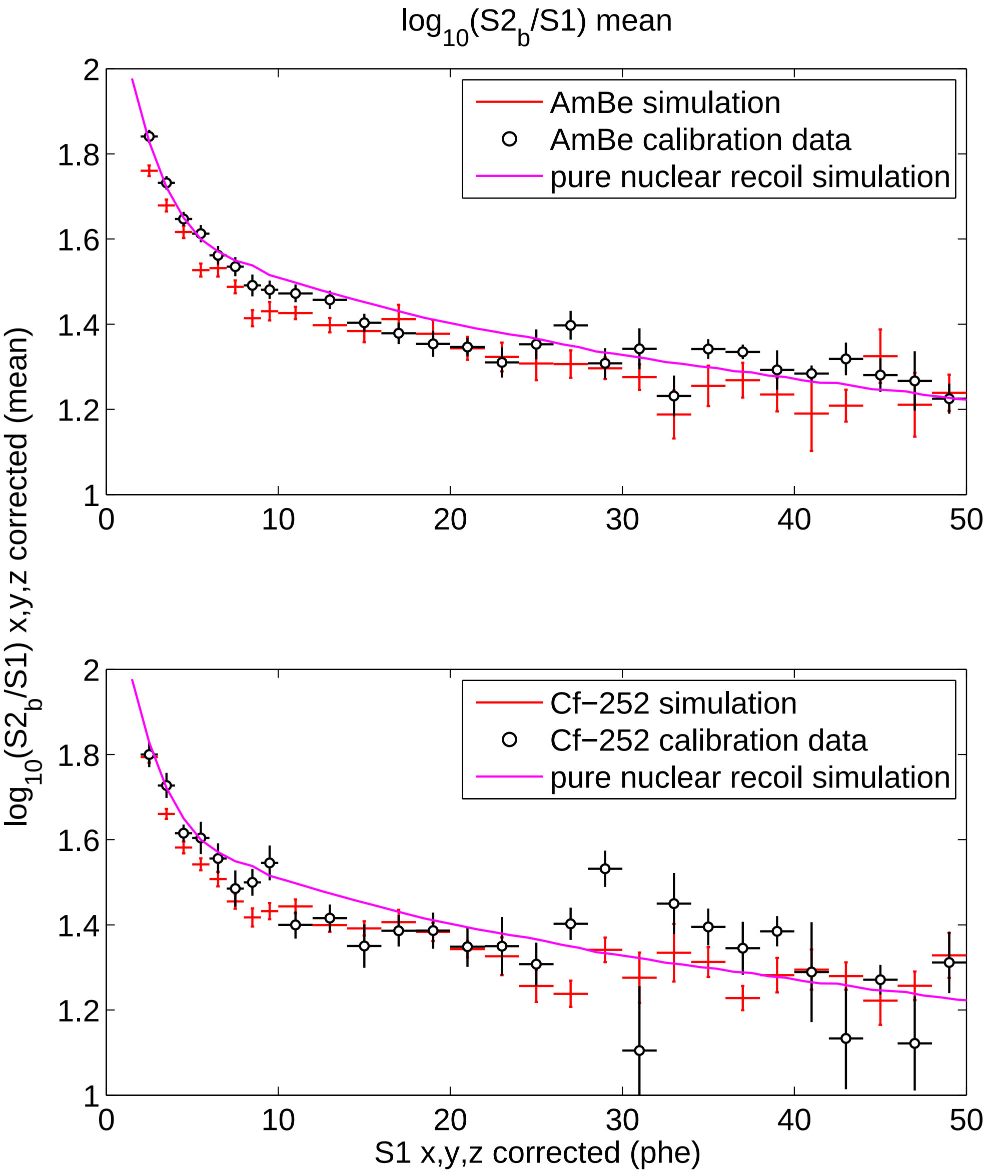

Figure 7.1: Comparison of band means between data [black] from the AmBe soucre [top] and the ^{252}Cf source [bottom], and LUXSim simulated data from the same source [red]. Also shown are the predicted spectra for WIMP nuclear recoils. Differences observed are the result of multiple scatters as well as unwanted Compton scatters from AmBe and γ and (n,γ) interactions from ^{252}Cf [47]. Figure reproduced from [96].

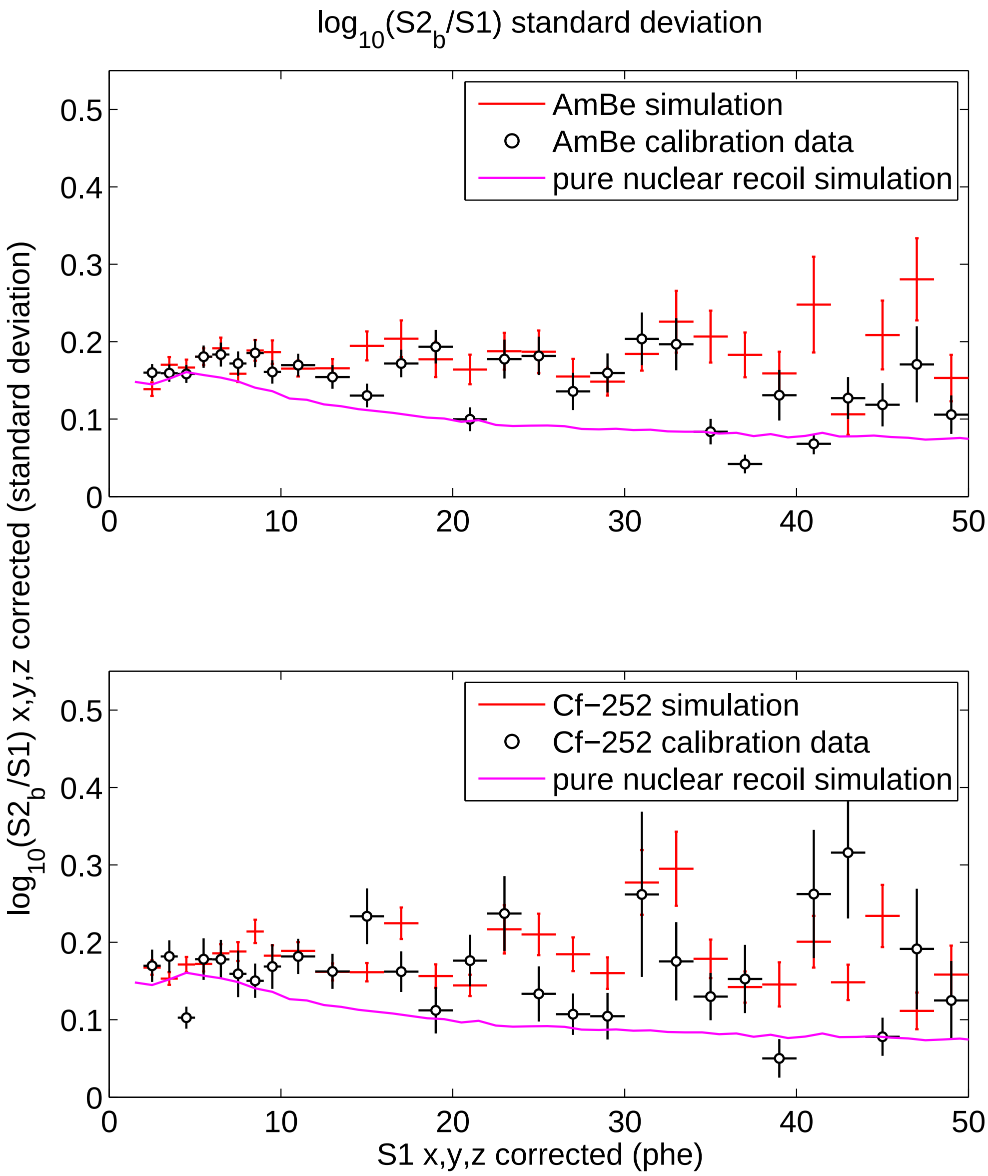

Figure 7.2: Comparison of band standard deviations between data [black] from the AmBe soucre [top] and the ^{252}Cf source [bottom], and LUXSim simulated data from the same source [red]. Also shown are the predicted spectra for WIMP nuclear recoils. Differences observed are the result of multiple scatters as well as unwanted Compton scatters from AmBe and γ and (n,γ) interactions from ^{252}Cf [47]. Companion figure to 7.1. Figure reproduced from [96].

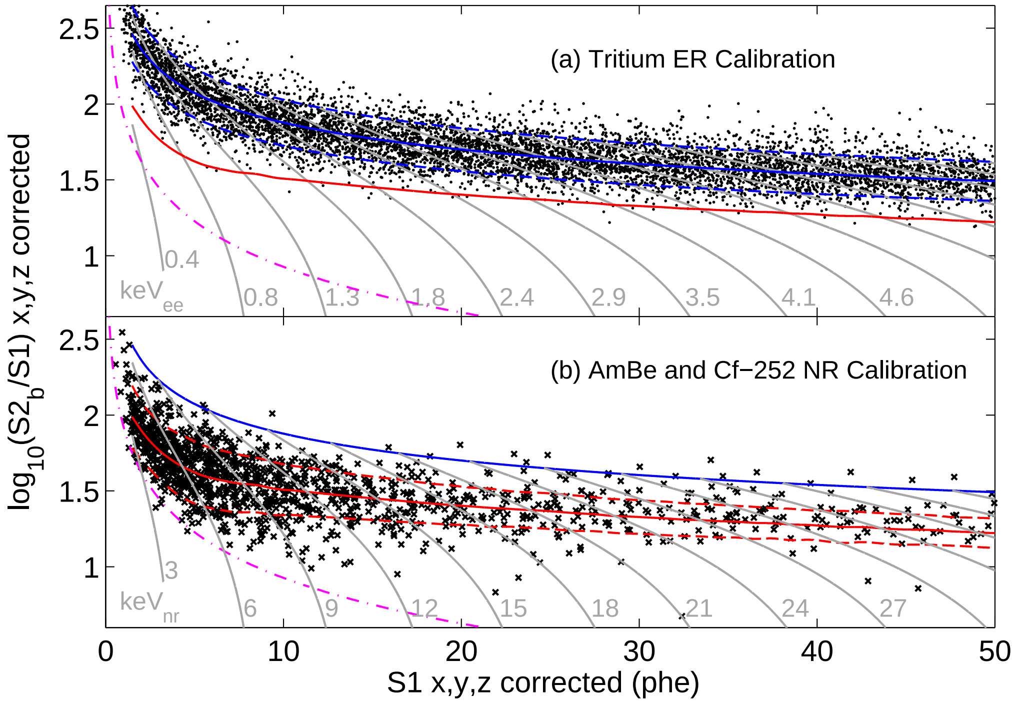

FIGURE 7.3: Calibration of the electron recoil [top] and nuclear recoil [bottom] response of the LUX experiment for the first WIMP search result. Solid lines are centroid values while dashed lines are drawn at 1.28σ. The mean centroid of the ER band is plotted with the NR data and vice-versa. The magenta line is representative of the 200 photoelectron cutoff in S2, which we discuss in section (7.3). Gray contours are lines of constant energy, calculated using the combined energy framework discussed in chapter 5. Contours on both plots are the same energies but are labeled in keVee [top] and keVnr [bottom] accounting for the Lindhard factor discussed in section (5.1.3). The ER band is directly measured from tritium data [top] while the NR band [bottom] is from simulation taking account for source effects not expected in true WIMP events, such as multiple scatters. Figure reproduced from [47].

for electron recoils, keVnr for nuclear recoils, or both if recoil type is unknown, such as in the WIMP search data.

7.3 Data Quality Cuts

Besides the live-time cuts discussed in section (7.1) and the requirement of single-scatter events, we also require the raw area of the S2 in an event to be greater than 200 phe ($\sim$ 8 extracted electrons) to account for any possible pile-up of single-electron populations following a large S2. This cut also removes a class of small events which have large uncertainties on their x-y position, which could result in events from outside the fiducial region being falsely reconstructed into the core volume or vice-versa. This is a problem because contamination on the detector walls, such as ^{216}Pb is observed to lose charge (S2 signal) resulting in events that can look like NR events. The choice of 200 phe is tuned by examination of events outside the energy range of interest in the WIMP search and by studying the accuracy of the position reconstruction module, called Mercury, at rejecting wall events [47]. We also exclude from the WIMP search periods of data displaying high rates of single electron emission from the liquid surface, containing greater than 4 electrons in a 1 ms window, with an associated loss of live-time of 0.8% [47].

We also apply cuts on S1 and S2 size corresponding to the energy region of interest during the WIMP search. For an event to be considered for the WIMP search it must have an S1 in the range of $2 < \text{S1} < 30$ phe and an S2 in the range of $200 < \text{S2} < 3300$ phe [47].

The final cut, the fiducial cut, is described in detail in the next section. Table (7.1) describes the net effect of each data cut, mapping from the recorded $83,673,413$ triggers over the full run to the 160 events considered in the WIMP search result.

Cut	**Events Remaing**
all triggers	$83,673,413$
detector stability	$82,918,902$
single scatter	$6,585,686$
S1 energy (2 - 30 phe)	$26,824$
S2 energy (200 - 3300 phe)	$20,989$
single electron background	$19,796$
fiducial volume	160

Table 7.1: Table of all cuts of use in the WIMP search results presented in section (7.7). Cuts are determined from examination of background event populations in the data in an un-blinded fashion, [47] supplementary material.

7.4 Fiducialization

Fiducialization is an essential part of reducing the number of background events that would otherwise dominate any possible observed signal. We perform fiducialization in the LUX experiment by examinaing events originating from the decays of ^{222}Rn daughters embedded on the PTFE panels surrounding the active region, where event selection is outside the WIMP energy region (S1 $>$ 30 phe). Using a fiducial radius of 18 cm we exclude events from these radon progeny embedded in the walls, which would otherwise form a population of events below the nuclear recoil band, though intersecting the band at the lowest energies [47].

Fiducialization is also done in z, to cut events originating from either ^{222}Rn progeny or component gamma backgrounds, dominated by events from the grids and PMTs respectively [47]. Examining the same population as for radial events, S1 $>$ 30 phe, cuts are placed requiring events in the fiducial volume to have measured electron drift time, between 38 and 308 μs. This corresponds to between $\sim$5.7 and $\sim$46 cm as measured from the liquid surface, with 48 cm being near the bottom of the detector.

The effect of fiducialization is seen in figure (7.4), which depicts events from the first WIMP search dataset with S1 signals in the region of interest, $2 <$ S1 < 30 phe, as a function of position inside the detector. Fiducialization removes the event populations resulting from the walls, gate, and cathode grids. Also shown are positions of events passing the fiducialization cuts as well as the locations of the PTFE walls of the upright-dodecagonal prism active region.

After fiducializing to remove backgrounds, a 118.3 ± 6.5 kg fiducial mass remains, which is used as the target mass for calculating the WIMP limits in section (7.7). Fiducial mass is determined by combining known detector dimensions with the reconstructed position maps provided by the tritium data which are expected to be spatially uniform, and confirmed with the ^{83m}Kr source [47].

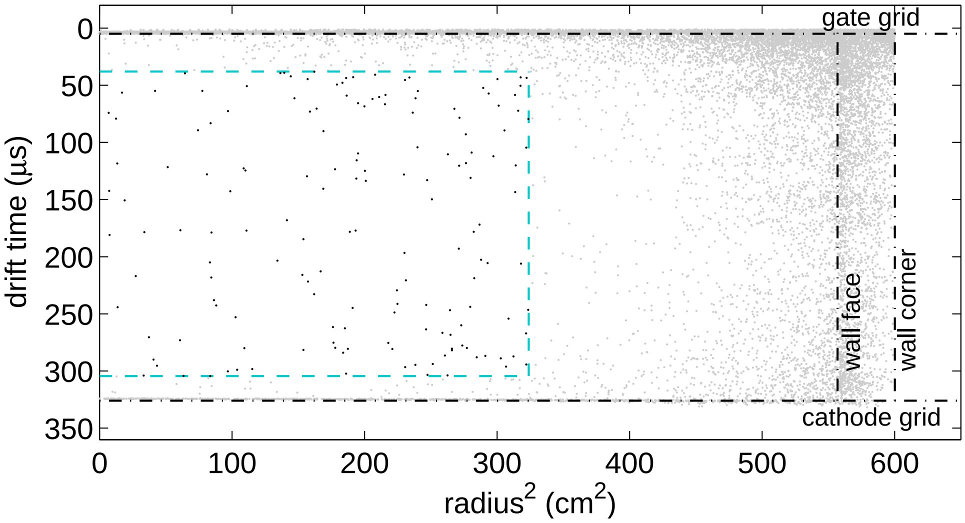

FIGURE 7.4: Physical location in x,y, and z of events during the first WIMP search. Events [gray] are required to be single scatters with an S1 signal in the range $2 < \text{S1} < 30$ phe. Also depicted are the location of the fiducialization cut [cyan] as well as the locations of important physical structures such as the PTFE reflector walls and corners, the gate grid, and the cathode grid. Figure reproduced from [47]

7.5 Efficiencies and Light Yield Model

Efficiency for detecting low energy single scatters, with both the S1 and S2 signal being observed, are displayed in figures (7.5) and (7.6). Efficiencies for finding low energy scatters are dominated by the efficiency with which we detect low energy S1 signals, with the efficiency for finding S2 signals above the analysis threshold of 200 phe being $> 99\%$ [47]. Absolute efficiency for the observation of events is estimated in two ways: via the injected tritiated-methane source, from which we measure the efficiency of finding low energy β^- events given the known energy spectrum of the tritium source and the measured activity of an injection, and a hand-scan of nuclear recoil calibration data, which finds a 98% absolute efficiency for the detection of nuclear recoils [47].

Combining all efficiencies and cuts results in a detection efficiency for WIMPs ranging between 17% at 3 keVnr and $> 95\%$ above 7.5 keVnr, with 50% acceptance occurring at 4.3 keVnr [47].

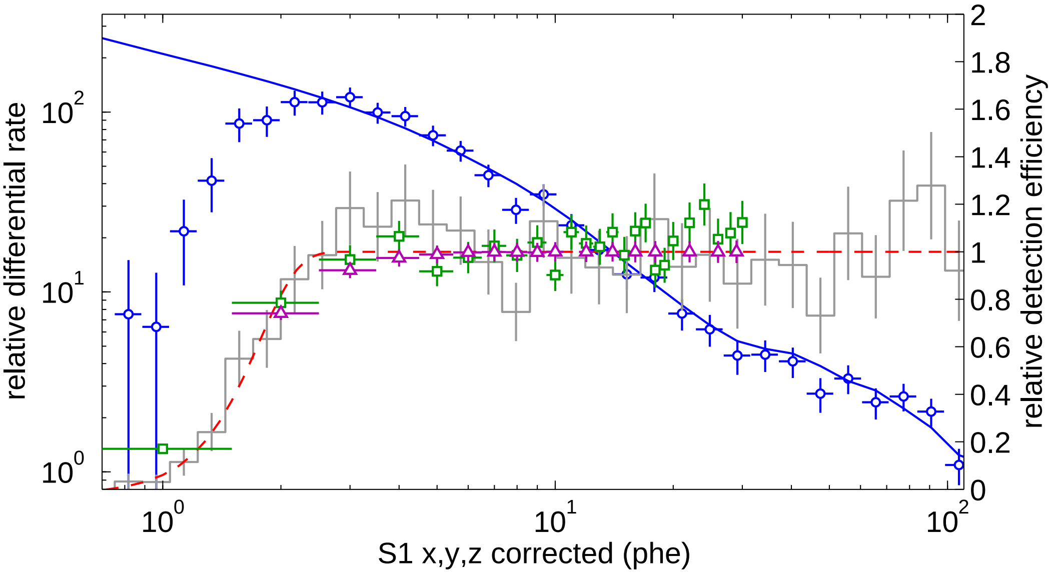

Figure 7.5: Relative differential rate for AmBe data (blue circles) and LUXSim simulation (blue line) normalized using the high energy bins. The gray histogram is the corresponding relative detection efficiency with fit [red dashed line]. Also shown are tritium measured detection efficiency for electron recoil events [green] and simulated detection efficiency for the pure nuclear recoils spectra as shown in figures (7.1) and (7.2) [purple triangles]. Relative efficiency is convolved with measures of absolute efficiency described in the text to calculate the final efficiencies. Figure reproduced from [47]

Figure (7.6) shows the nuclear recoil acceptance rate as a function of energy but does not show the assumed light and charge yield as a function of energy, which is shown in figure (7.9). Here a conservative limit through all the world's current data is used in the profile-likelihood modeling, section (7.7). In addition, a cutoff in response is used by setting simulated charge and light yield to zero below the lowest energy response measurement done in liquid xenon. This cutoff is included in the first WIMP search result as a measure of conservatism, preventing the need for any data extrapolation. Since the time of this first result however, we have performed new calibrations *in situ* using a deuterium-deuterium neutron generator, which we discuss in section (7.8).

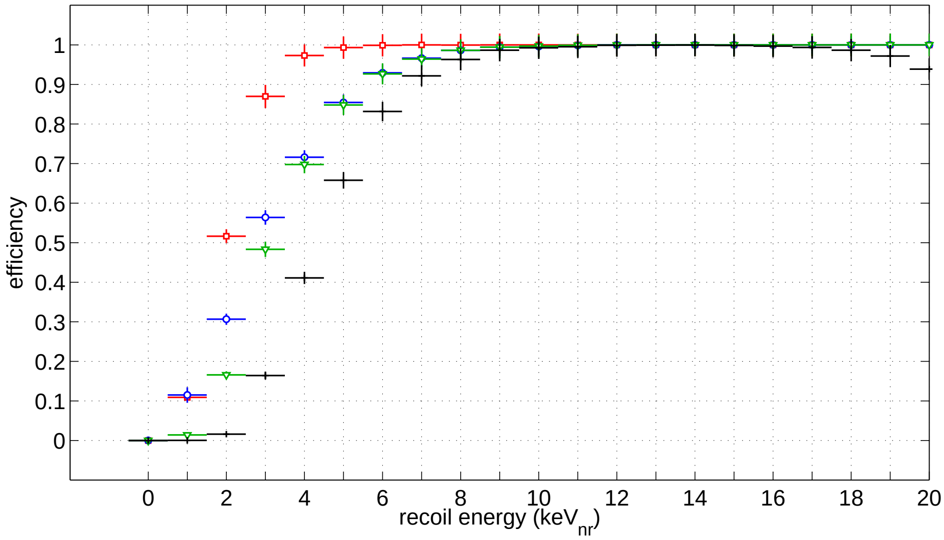

FIGURE 7.6: Nuclear recoil detection efficiency for finding the S1 [blue], the S2 [red], both the S1 and S2 [green], and the full efficiency including the analysis thresholds for $3 < \mathrm{S1} < 30$ phe and $\mathrm{S2} > 200$ phe. The roll-off beginning to appear in the full efficiency at recoil energies > 17 keVnr is due to the cutoff restricting $\mathrm{S1} < 30$ phe. Not shown is the cutoff in simulated light and charge yield below 3 keVnr below which the likelihood model assumes no light or charge yield for the extraction of WIMP limits. Figure reproduced from [47]

7.6 Backgrounds

Extensive modeling of background populations is done which we summarize here but refer the reader to [43] for full details. Background sources considered for the first WIMP search are a combination of backgrounds from internal components, resulting mainly from γ rays generated by radioisotope decays of impurities contained in the detector construction materials, intrinsic backgrounds such as cosmogenically activated xenon and ^{85}Kr, and external backgrounds which are found to be sub-dominant [43].

Component backgrounds were modeled using LUXSim which was compared to measured data at high energy ($E > 500$ keVee) to avoid contamination from intrinsic sources, such as the line features resulting from cosmogenically activated xenon described in table (5.1). Comparison of simulation to high energy data is done to constrain the estimates of ^{238}U, ^{232}Th, ^{40}K, and ^{60}Co present in the detector components. Independent fitting of the measured γ ray spectrum as a function

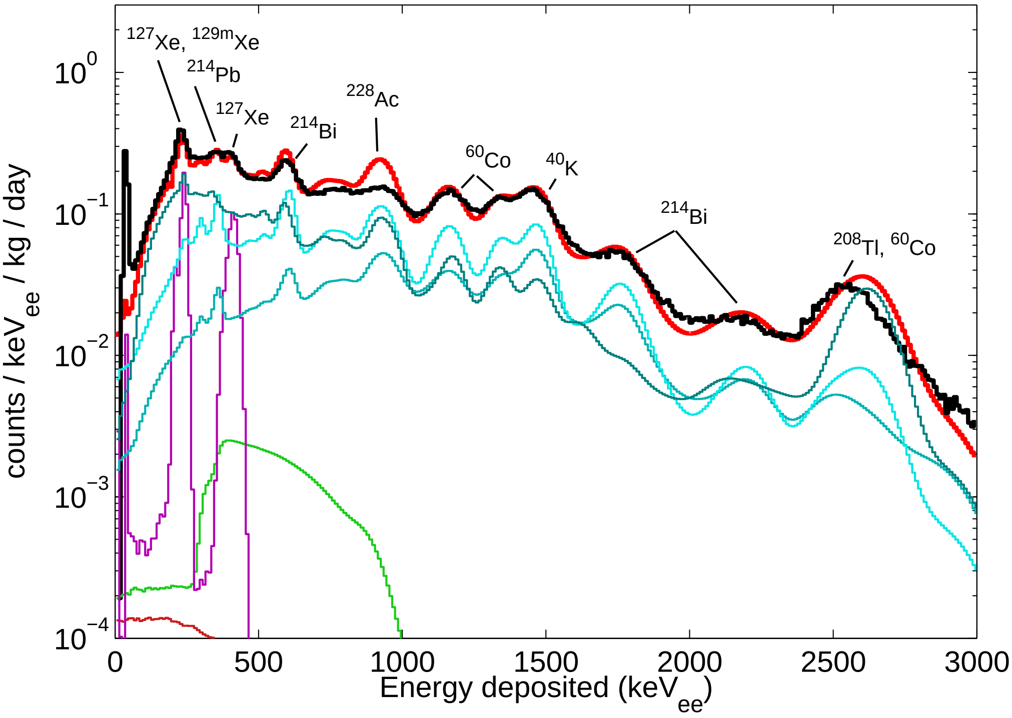

FIGURE 7.7: Histogram of the rate of high energy background events as measured in a 225 kg fiducial (cut 2 cm inwards from grids but no radius cut) [black] and best-fit simulation [red]. Simulation split sources based on geometric location of top (blue), bottom (dark blue) and side (light green). Simulation accounts for γ rays from ^{238}U, ^{232}Th, ^{40}K, and ^{60}Co, fitted above 500 keVee. Simulation fit below 500 keVee is also shown, convolving in ^{85}Kr, ^{214}Pb, and activated xenon (purple). Figure reproduced from [47].

of position is done to determine the decay rate of each isotope [43]. Figure (7.7) shows the measured and simulated backgrounds for these sources.

Though the simulation does well over a broad range of energies it fails to achieve good agreement with the ^{238}Ac line at 969 keV, possibly due to removal of its parent ^{238}Ra during manufacturing of internal components [43].

The presence of backgrounds from ^{214}Pb are the result of ^{222}Rn, present from contamination during air exposure periods of construction, from the use of a radon calibration source in Run 2, and from possible sources internal to the circulation system from thoriated welds [97].

Backgrounds from ^{85}Kr are present due to atmospheric contamination as described in section (3.3). Purification of the ^{85}Kr is done using chromatographic separation via a column of activated charcoal, and krypton concentration is measured via the online sampling system, section (3.8). During the WIMP search the average krypton concentration is measured to be 3.5 ± 1.0 ppt g/g, for an ER background rate of $0.17 \pm 0.1 \cdot 10^{-3}$ counts/kg/keVee/day [43].

Though several activated xenon isotopes are present in the xenon target, table (5.1), only ^{127}Xe contributes to the low energy WIMP background population [43]. These low energy backgrounds result from a decay of the xenon isotope and its daughter ^{127}I when the ^{127}I γ-ray escapes the active region leaving only an L (or higher) shell x-ray to be detected. Estimation of these events indicate 50% of L shell decays for which the ^{127}I γ-ray escapes leak into the WIMP energy search region and all higher shell x-rays are in the WIMP search window [43].

Table (7.2) shows the overall predicted and observed background rate for low-energy events in the 118 kg fiducial target used in the WIMP search, with the background models showing good agreement with observed background rates across a range of energy scales and sources.

Source	**Background Rate** [10^{-3} **cnts/keVee/kg/day**]
γ rays	$1.8 \pm 0.2_{\text{stat}} \pm 0.3_{\text{sys}}$
^{127}Xe	$0.5 \pm 0.02_{\text{stat}} \pm 0.1_{\text{sys}}$
^{214}Pb	$0.11 - 0.22$ (0.20 expected)
^{85}Kr	$0.17 \pm 0.10_{\text{sys}}$
Total Predicted	$2.6 \pm 0.2_{\text{stat}} \pm 0.4_{\text{sys}}$
Total Observed	$3.6 \pm 0.3_{\text{stat}}$

TABLE 7.2: Table of background rates for low energy events in the 118 kg fiducial volume predicted from simulation and overall observed. γ rays are the result of decays of radioisotope contaminants in detector materials. Table modified [to label cnts/keVee/kg/day] from [43].

7.7 Results

Figure (7.8) shows the 160 events passing all cuts described in table (7.1). Events mainly populate the electron recoil band as expected for non-neutron backgrounds.

To determine if the data are consistent with an observation of a WIMP signal, a profile-likelihood-ratio (PLR) test is conducted. This PLR test is run over the events in WIMP search fiducial region and models signal, derived from AmBe and ^{252}Cf sources, and backgrounds, comparing whether the observed data are consistent with a background-only model. Models for backgrounds encode uncertainty in the background rates but no variation in spatial distributions for the backgrounds is done, with these distributions instead being extracted from simulations. Separation between signals and backgrounds are expected in four primary channels. Two of these are spatial, radius and depth, where we expect WIMP signals to be uniform while backgrounds may display non-uniform behavior. The other two are our discrimination parameters, the amount of S2 (charge) and S1 (light) signal seen from a given event [47], also used as a proxy for energy.

Signal models in the PLR are generated using an isothermal Maxwellian halo model, with an escape velocity of 544 km/s, a v_0 of 220 km/s, an Earth velocity of 245 km/s, and a WIMP density of 0.3 GeV/cm^3, though no variation due to uncertainties in astro-physical parameters is done [47]. Figure 7.9 shows the light yield as a function of energy assumed for modeling the signal expected from WIMP interactions.

From this testing, we conclude the observed distribution is consistent with no WIMP signal, with Monte Carlo background-only simulations up-fluctuating to be more discrepant then the observed data 35% of the time [47]. Given this, we calculate a limit curve as a function of WIMP mass, setting the world's most sensitive limit on spin-independent WIMP-nucleon cross section, figure (7.10).

Here, the LUX experiment results are in tension with several previous potential low-mass WIMP detections, from CoGeNT [51], CDMS II silicon [54], CRESST II [49], and DAMA/LIBRA [45]. Whether these tensions are the result of exotic properties of the dark matter [53] or systematics or backgrounds in the various detectors and searches performed remains to be determined.

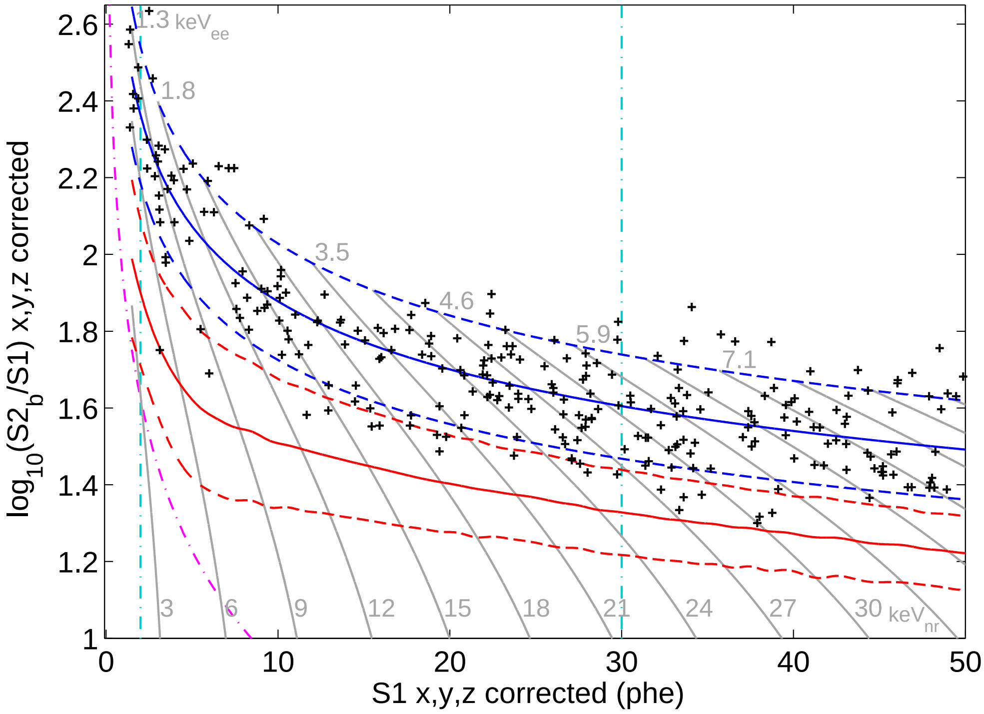

FIGURE 7.8: Events [black] passing all selection criteria described in table (7.1) in log($S2_b$/S1) versus S1. Event signal sizes are plotted after position corrections for both S1 and S2. Only events within the cyan lines are considered as part of the WIMP search, corresponding to the *a priori* set boundaries of $2 < \text{S1} < 30$ photoelectrons. Also shown are means [solid] and 90% one-sided confidence intervals [dashed] on the nuclear [red] and electron recoil [blue] bands from the calibration data shown in figure (7.3). Gray contours are iso-curves of energy, labeled in keVee at top and keVnr at bottom. Figure reproduced from [47].

7.8 Next Steps

In this section we review the future plans of the LUX experiment followed by brief comments on the planned next generational experiment, LUX-Zeplin. Given the lack of a WIMP signal detection in the first search, these next steps may provide us the first detection of WIMP interactions or a look into the final window of accessible parameter space in WIMP cross-section prior to hitting the astrophysical neutrino background.

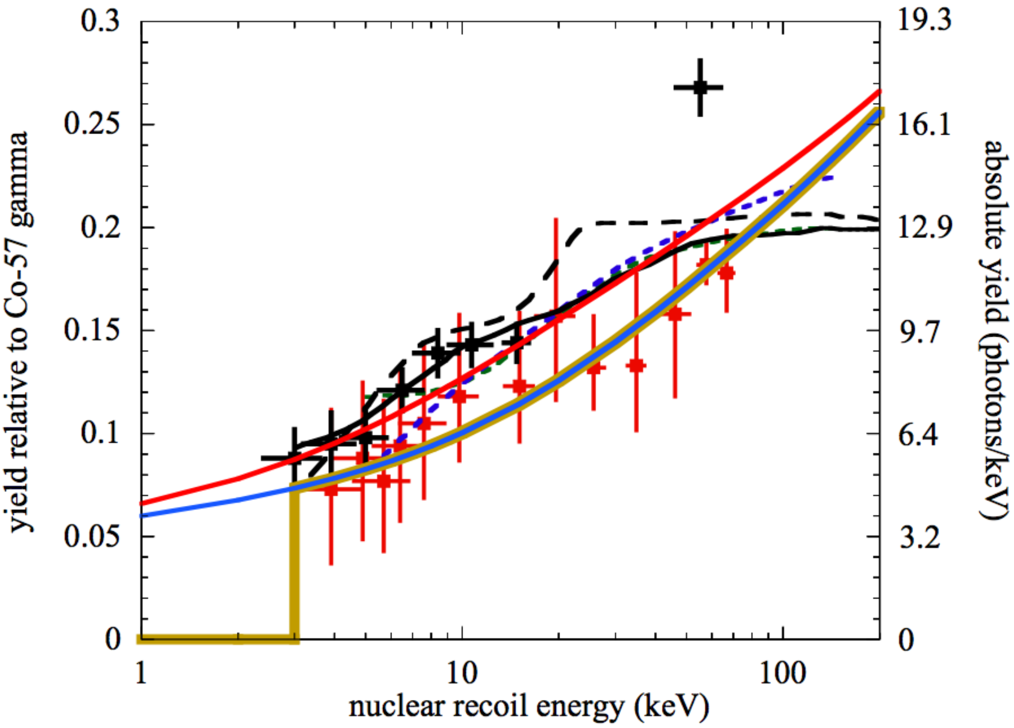

Figure 7.9: Light yield in photons/keVnr relative to ^{127}Co source [left axis] and absolute [right axis]. Conservative NEST model based on neutron calibrations discussed in section (7.2) [blue], and corresponding zero-field [red]. Inclusion of conservative cutoff in light production [gold], as used in the WIMP search. Plot also includes results from Xe100 [98], [99], and [100] (black dashed, solid, and squares respectively) Zeplin3 [101] (green and blue for first and second run respectively), and [102] (red squares). Figure reproduced from [96].

7.8.1 The LUX First WIMP Search Re-Analysis

After completing the first WIMP search, and subsequent analysis, the LUX collaboration is moving on to preparing for the full 300-day blinded WIMP search run, described in more detail in section (7.8.3). As part of this process, we are reexamining our backgrounds and technical limitations from the perspective of finding any possible bias that may have been included in the first result.

One discovery of this ongoing search is the presence of sub-threshold “ringing” following single photoelectron (sphe) pulses. This ringing results in a tail of positive area on the distribution of sphe pulses that is truncated in the first WIMP result. Because larger pulses are a sum of sphe pulses and the pulse window is dynamic

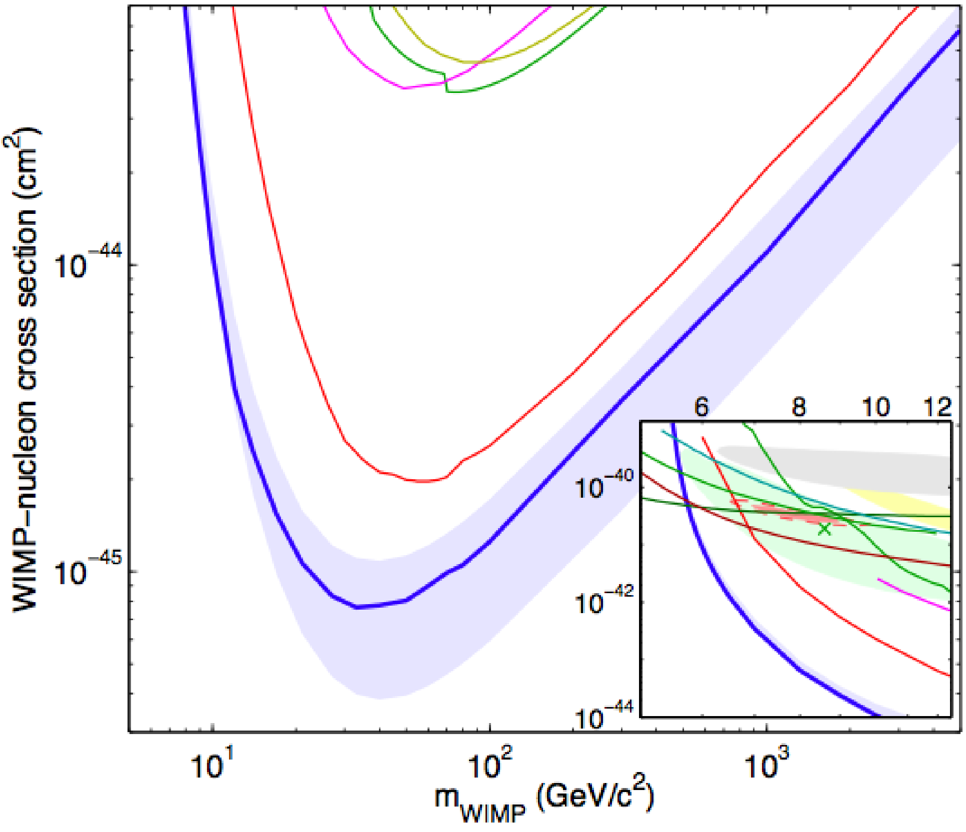

FIGURE 7.10: Spin-independent WIMP-nucelon cross section from LUX (blue) with ±1σ contours as well as from Edelweiss II [dark yellow line], CDMS II [light green line], ZEPLIN-III [magenta], CDMSlite [dark green line], XENON100 S2 only analysis [brown], SIMPLE [light blue], and XENON100 both 100 and 225 live-day exposures [orange and red respectively] where results are from [103], [103], [48], [104], [54], [105], [106], [107], and [108], respectively. The inset displays regions measured from CoGeNT annual modulation signal [light red], exclusion limits from CDMS II low-threshold analysis [upper green], CDMS II Si detectors 95% confidence allowed region [green shaded] with centroid [green x], CRESST II allowed region [yellow], and the DAMA/LIBRA allowed region as interpreted by [109]. Inset data from [51], [110], [54], [49], and [45], respectively. Figure reproduced from [47].

over the length of the pulse, this effect results in a bias for the calculated area of pulses in photoelectrons, longer pulses including more of the normally truncated tails. This effect is due to sphe peaks occurring in the middle of the pulse that do not have truncated tails as the pulse window is continuing until the end of the pulse.

The second effect in the run 3 data is double electron production from the photocathode when exposed to xenon VUV scintillation light. In the first WIMP analysis the PMT gains are obtained from LED data, where the LEDs are 430 nm (blue) LEDs inside PTFE diffusers [75]. Xenon scintillation light has a wavelength of 178 nm, a factor of ~ 2 in energy, and preliminarily have a $\sim 30\%$ chance of causing a second electron to be produced in the PMT photocathode [111]. These double emissions seem to be much less probable in LED calibrations, indicating they are a result of the higher energy of the xenon VUV photons. While this effect has been theoretically described, [112], [113], and the previous dark matter search, ZEPLIN III, successfully performed *in situ* calibration using S2 light [114], no measurement of the probability of double electron emission for PMTs exposed to xenon VUV radiation has been done, resulting in an ongoing effort to calibrate LUX using xenon VUV photons directly.

Both of these effects are currently being measured, with plans for a full data reprocessing and reanalysis before publishing a new paper in early Fall 2014. These effects are in addition to the planned change in the light yield model resulting from the use of the deuterium-deuterium generator, which we will discuss in section (7.8.2). While preliminary analyses indicate only minor shifts in the size of small pulses, $\sim 2-4\%$ for those of interest in the WIMP search region, large pulses are expected to have an $\sim 20-30\%$ shift in size [115], resulting in a need to recalculate g_1 and g_2 from calibrated data, as described in 5. Results from correction of these two effects and subsequent improvements to the LUX energy reconstruction, position reconstruction, and data-processing, in addition to the inclusion of the results of the deuterium-deuterium generator will be published in [116]. The methodologies we discuss in chapters 5 and 6 are expected to be robust through these changes but publication of full results is delayed to allow the full reprocessing.

7.8.2 Deuterium-Deuterium Generator Calibrations

As described in section (7.7) the first WIMP search is done with an assumed light yield model that was both a conservative interpretation of the observed data, and included a cut-off in the light and charge yield below 3 keVnr. In order to better characterize the LUX light and charge yields with respect to low-energy nuclear recoils a program of *in situ* calibrations using a deuterium-deuterium (D-D) generator is being performed.

This generator, an Adelphi Technologies DD108, is placed outside the LUX water shield, and a plastic collimator, consisting of a hollow tube of plastic, is used to allow neutrons from the generator to penetrate the water tank. When not in use, this plastic tube is lowered back to its resting position below the detector so no compromise of the water shielding occurs during running.

D-D generators create a monochromatic neutron source, $E_n = 2.45$ MeV, using the reaction:

$$D + D \rightarrow {}^{3}\text{He} + n, \tag{7.8.1}$$

as the source of the neutrons [117]. For LUX calibration, 2.45 MeV is above the desired calibration energy range but we can achieve low energy calibration through the examination of double scatter events that have a low-energy primary scatter. Here use is made of the large physical scale of LUX to maintain reasonable event rates of completely contained double-scatter events. Knowing the incident neutron energy and the position of both scatter vertices we can determine the energy of the first scatter purely kinematically:

$$E_r = 2 \cdot E_n \frac{M_n M_{Xe}}{(M_n + M_{Xe})^2} \cdot (1 - cos\,\theta)\,, \tag{7.8.2}$$

where E_r is the energy of the first recoil, E_n is the energy of the incoming neutron, 2.5 MeV, M_n is the mass of the neutron, M_{Xe} is the mass of the xenon atom, and θ is the angle between the two scatters in the center of mass frame. Using kinematic energy reconstruction provides an independent energy calibration in addition to the signal-based reconstruction.

Initial calibrations using the system are indicative of light response below the currently imposed cut-off, and inclusion of these results is expected to significantly lower the current WIMP limit with respect to low-mass WIMPs, $M_{WIMP} \lessapprox 20$ GeV/c^2 based on preliminary simulations using LUXSim [85], [118], [119], and [120]. Full results are expected to be reported in [121].

7.8.3 300 day WIMP Search Run

In parallel to the re-analysis effort described above, LUX plans a 300 live-day science run. Expected to achieve a $\sim$ 5 times greater WIMP sensitivity, in addition to improvements due to the D-D data. This improvement in sensitivity is due to longer search time, the use of more accurate light yield model, improvements in thresholds, and the use of better position reconstruction leading to a slightly larger fiducial volume. Further reduction of the background rate due to the decay of ^{127}Xe is also expected.

The 300 day WIMP search is scheduled to begin in early Fall of 2014, after a series of calibration steps including further use of the D-D generator and tritium at multiple allowed drift fields for the refinement of the NEST model.

7.8.4 LZ - A Next Generation Experiment

In parallel to the LUX science run, a next generation detector, LUX-Zeplin (LZ) is in development, with a planned active region containing $\sim$ 7 tonnes of liquid xenon. Learning from the LUX design, in which the heat exchange system was internal to the detector, resulting in significant overhead in insulation and significant design constraints as outlined in chapter 4, LZ will make use of a separate chamber outside the detector for its heat exchanger systems, allowing for much larger scale purification and simpler design of the TPC.

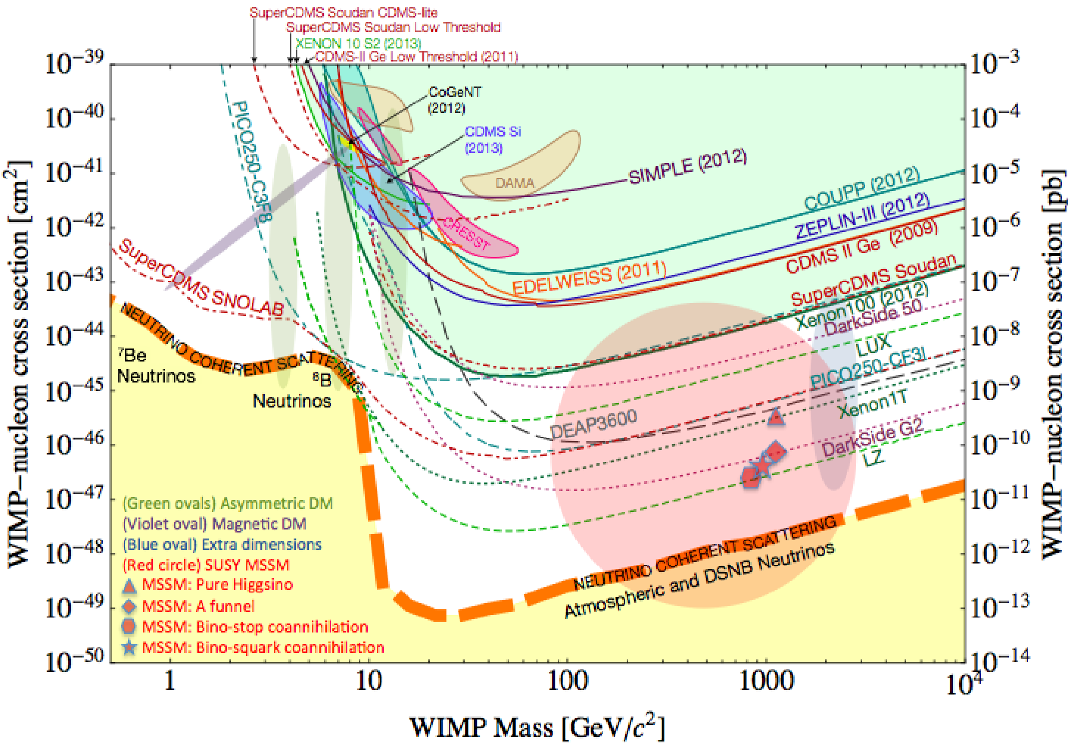

FIGURE 7.11: "A compilation of WIMP-nucleon spin-independent cross section limits (solid curves), hints for WIMP signals (shaded closed contours) and projections (dot and dot-dashed curves) for US-led direct detection experiments that are expected to operate over the next decade. Also shown is an approximate band where coherent scattering of 8B solar neutrinos, atmospheric neutrinos and diffuse supernova neutrinos with nuclei will begin to limit the sensitivity of direct detection experiments to WIMPs. Finally, a suite of theoretical model predictions is indicated by the shaded regions, with model references included." Figure and caption reproduced from [62].

LZ is scheduled to begin running by 2018, directly replacing the LUX detector installation in the current Davis cavern at the Sanford Underground Research Facility. Figure (7.11) shows the predicted future reach of experiments with respect to the the detection of WIMPs via spin-independent WIMP-nucleon interactions.

7.9 Conclusion

Having begun with a survey of the background research motivating the search for WIMPs and dark matter in general, we also reviewed current experimental techniques to search for these extremely rarely-interacting particles, culminating chapters 1 and 2 with a discussion of the currently leading technology in the search for the spin-independent coupling between nucleons and WIMPs.

In chapters 3 and 4, we discussed the LUX detector systems and performance that allowed for the development of a stabile platform on which to perform a WIMP search. Here, the focus was the LUX heat exchange system, which demonstrated $\sim 90\%$ efficient heat exchange at 27 slpm, the sustainable flow rate in the LUX detector given the circulation system. We further showed that this system allowed for both rapid purification of the xenon target and the development of extremely well behaved thermodynamic conditions internal to the detector.

In chapter 5 we described the energy calibration process required for detectors of this type, finding g_1 and g_2 through several methods, which allowed for the first determination of the presence of systematic offsets in the data, requiring the reprocessing described in section (7.8.1). Further studies of these effects after this reprocessing are planned to be published in [91].

From the discussions on discrimination we determined two important aspects of discrimination for xenon TPCs: intrinsic fluctuations arising from recombination, turn-off at the lowest energies, and it is light-collection that determines discrimination power at the lowest energies. Light-collection dominating observed low energy fluctuations and setting the analysis thresholds described in this chapter.

Finally, in this chapter, we examined the results of the first WIMP search using the LUX experiment and the setting of the world-leading limits on the spin-independent WIMP-nucleon cross section. We then examined future plans for both the LUX experiment and its successor experiment, LZ, a planned rich experimental program to continue to lead the world in the search for weakly interacting dark matter.

We conclude with figure (7.11) that shows the many classes of technology being investigated for future dark matter searches [62]. The search for dark matter continues both in WIMP and axion searches, and in searches for more exotic candidates as well.

With hints of detection having been observed in several detectors, we may need to confront more complex theories of dark matter interactions with nuclei [53], which may require the use of multiple technological platforms to maintain sensitivity. In addition, next generational experiments will also need to overcome large-scale technological challenges in order to meet their science goals. The ability of a TPC to eventually reach the neutrino background, the final boundary of searching for WIMPs on Earth, will be set by whether detectors of this class can overcome technical challenges while maintaining maximal discrimination power.

The goal of this work is that methods outlined here help future scientists be ready for the day when the unblinding of the search data comes and a significant excess of unexplainable events is observed, whether that day be in the next run of LUX, in LZ, or in physics experiments beyond what is being planned now.

Appendix A

Method of Centroid Subtraction

A.1 Introduction

This appendix describes the method of using centroid subtraction to create linear bands in a given parameter space, of great use when working with finite histogram binned data as a way to avoid inflation in measured variance in each bin due to variation in the underlying centroid across the bin. Moving to small bins in the face of large statistics can also be used to mitigate these effects, but as interesting analyses will often be statistics limited, the following method provides a general framework for avoiding this problem. We first examine the general principle before applying it explicitly to the case of the discriminant $\log(n_e/n_\gamma)$, reproducing the work by C.E. Dahl [65], and extend it to the case of number of quanta in a single channel versus energy, for example n_e or n_γ vs Energy.

A.2 Basic Method and mapping of fluctuations through the transform

We begin with the general problem, in which we seek to find a smoothly varying "centroid" of some distribution, f(E), where we define the "centroid" as the mean of the conditional distribution f at E, so we can subtract out the centroid to find some new distribution $\Delta f(E)$,

$$\Delta f(E) = f(E) - \langle f(E) \rangle_E, \tag{A.2.1}$$

where $\Delta f(E)$ is our centroid subtracted distribution, f(E) is our starting distribution, and $\langle f(E) \rangle_E$ is the true mean of the distribution f(E) at E.

As we seek to work in the framework of binned data we must construct an estimator of the true centroid of the distribution which we do not know *a priori*, and expect this operation may introduce some systematic offset in the observed bin-by-bin variance. We denote our estimator of $\langle f(E) \rangle_E$ in bin E as μ with $\delta[\mu]$ as the difference between our binned centroid estimator and the true centroid across our bin and can thus calculate the change in variance inside the bin defined by edges E_1 and E_2:

$$\delta[\sigma^2] = \langle \delta[\mu^2] \rangle - \langle \delta[\mu] \rangle^2 = \frac{\int_{E1}^{E2} dE (\delta[\mu])^2}{E2 - E1} - \left(\frac{\int_{E1}^{E2} dE (\delta[\mu])}{E2 - E1} \right)^2 \tag{A.2.2}$$

We caution the reader to observe the difference between this δ and the one used later in the text which refers to individual event fluctuations. We note, that as we cannot know the true centroid across a bin, we will be forced to make an estimate of this variance shift, but leave such a treatment to specific applications, such as the estimator calculated in figure (6.8). We now seek to fully understand how fundamental fluctuations, $\delta[a]$, in a single member of our distribution f, corresponding in our examples to the effects of variation in S1 and S2 per event, will affect how that event shifts in our centroid subtracted space. This mapping will then provide a way to analytically map back and forth between the regular and centroid subtracted -spaces with some limiting assumptions.

We begin by examining a single underlying fluctuation, $\delta[a]$ on event i of m within a single bin under the approximation that fluctuations $\delta[a]$ are small compared to the curvature of the centroid, allowing us to estimate the observed change in the centroid value the i^{th} event observes using only the first derivative within our bin.

To be explicit in our notation, if our distribution f(E) was well characterized by a gaussian in bin x, $\sigma_{a,x} = \langle \delta[a] \rangle_x$. We further make an assumption that we have enough events in each bin such that the centroid estimator itself is not meaningfully changed by any single event level fluctuation, writing our two assumptions as:.

$$\begin{aligned} \delta[a] &<< \tfrac{d^2 f(E)}{dE^2}, \text{and} \\ m &>> 1, \end{aligned} \tag{A.2.3}$$

where m is the number of events in the bin our examined fluctuation is drawn from. For clarity this second assumption is simply the statement that each of our bins contains many events. Where we use δ to represent the change in the individual event and Δ to refer to a centroid subtracted quantity. With these assumptions we can then perform the following mapping from our fundamental event level shift $\delta[a]$ to $\delta[\Delta f(E)]$, how it shifts in our centroid-subtracted space.

$$\begin{aligned} \delta[\Delta f(E)] &= \delta[f(E)] - \delta[\langle f(E) \rangle_E] \\ &= \tfrac{df(E)}{da}\delta[a] - \tfrac{d\langle f(E) \rangle_E}{da}\delta[a] \\ &= \tfrac{df(E)}{da}\delta[a] - \tfrac{d\langle f(E) \rangle_E}{dE}\tfrac{dE}{da}\delta[a], \end{aligned} \tag{A.2.4}$$

where the final line comes from a simple change of variables $d/da \to d/dE$. The first term represents the shift in the non-centroid subtracted value while the second is the change in the centroid our event observed due to changing it's value of E from the fluctuation $\delta[a]$.

Practically, the main limitation of this analytical method is often due to inability to accurately reconstruct our derivative of some underlying interpolated fit to the means of the population in our bins of interest, in which case we must seek alternate methods such as monte-carlo. We now turn to two examples of interest, the first an examination of this mapping to create a centroid-subtracted discriminant, and the second for number of quanta in a single channel.

A.3 Example - the LUX discriminant

The LUX discriminant, though often taken in $ln\left(\frac{S2}{S1}\right)$, is perhaps more fundamentally taken as $ln\left(\frac{n_e}{n_\gamma}\right)$ which we shall use here. We note before beginning the combined energy relation,

$$E = (n_e + n_\gamma) = \left(\frac{S1}{g1} + \frac{S2}{g2}\right). \tag{A.3.1}$$

We now apply the framework given above in equation (A.2.4) but generalizing for two fundamental variations of interest, variations in the measured S1 signal and variations in the measured S2 signal, $\delta[S1]$ and $\delta[S2]$ respectively in units of quanta. These variations on n_e and n_γ arise from uncorrelated instrumental and statistical fluctuations in signal production. We avoid the use of the notation $\delta[n_e]$ and $\delta[n_\gamma]$ to avoid confusion with variations arising between $n_e and n_\gamma$ due to correlated effects such as recombination. Using equation (A.2.4) we derive:

$$\begin{aligned}
\delta[\Delta ln\left(\tfrac{n_e}{n_\gamma}\right)] &= \delta[ln\left(\tfrac{n_e}{n_\gamma}\right)] - \delta[\left\langle ln\left(\tfrac{n_e}{n_\gamma}\right)\right\rangle_E] \\
&= \frac{d\ ln\left(\frac{n_e}{n_\gamma}\right)}{dS1}\delta[S1] + \frac{d\ ln\left(\frac{n_e}{n_\gamma}\right)}{dS2}\delta[S2] - \frac{d\left\langle ln\left(\frac{n_e}{n_\gamma}\right)\right\rangle_E}{dS1}\delta[S1] - \frac{d\left\langle ln\left(\frac{n_e}{n_\gamma}\right)\right\rangle_E}{dS2}\delta[S2] \\
&= -\tfrac{\delta[S1]}{S1} + \tfrac{\delta[S2]}{S2} - \tfrac{d\langle\ \rangle_E}{dE}\tfrac{dE}{dS1}\delta[S1] - \tfrac{d\langle\ \rangle_E}{dE}\tfrac{dE}{dS2}\delta[S2] \\
\delta[\Delta ln\left(\tfrac{n_e}{n_\gamma}\right)] &= \left(\tfrac{\delta[S2]}{S2} - \tfrac{\delta[S1]}{S1}\right) - w\left(\delta[S1] + \delta[S2]\right)\tfrac{d}{dE}\left\langle ln\left(\tfrac{n_e}{n_\gamma}\right)\right\rangle_E .
\end{aligned} \tag{A.3.2}$$

We also note the fortuitous coincidence that in regions of this space where $\frac{d}{dE}\left\langle ln\ \left(\frac{n_e}{n_\gamma}\right)\right\rangle$ is negative the contributions from S1 fluctuations have reduced impact on $\Delta ln\ \left(\frac{n_e}{n_\gamma}\right)$ as in the WIMP search region for both electron and nuclear recoils. Or equivalently phrased, S1 fluctuations shift events along the band instead of perpendicular to the centroid, preserving discrimination power in the low energy bins.

A.4 Example - Number of quanta at an event site versus total quanta

We now turn the outlined method to estimation of band centroids in single quanta channels *i.e* n_e or n_γ as a function of energy, or equivalently, as is treated here $n_e + n_\gamma$. We find an equivalent formulation as is found geometrically by A. Dobi [92] under the assumption of a linear underlying centroid of slope M, but note the breakdown of geometric methods when the underlying centroid is non-linear as our transformation then no longer preserves angles. Using equation (A.2.4), we derive:

$$\begin{aligned}
\delta[\Delta n_e] &= \delta[n_e] - \delta[\langle n_e\rangle_{n_e+n_\gamma}] \\
&= \cancelto{1}{\tfrac{dn_e}{dn_e}}\delta[n_e] + \cancelto{0}{\tfrac{dn_e}{dn_\gamma}}\delta[n_\gamma] - \delta[\langle n_e\rangle_{n_e+n_\gamma}] \\
&= \delta[n_e] - \tfrac{d\langle n_e\rangle}{d(n_e+n_\gamma)}\tfrac{d(n_e+n_\gamma)}{dn_e}\delta[n_e] - \tfrac{d\langle n_e\rangle}{d(n_e+n_\gamma)}\tfrac{d(n_e+n_\gamma)}{dn_\gamma}\delta[n_\gamma] \\
\delta[\Delta n_e] &= \delta[n_e] - \left(\delta\left[n_\gamma\right] + \delta\left[n_e\right]\right)\tfrac{d\langle n_e\rangle}{d(n_e+n_\gamma)} \\
\delta[\Delta n_e] &= (1-M)\delta[n_e] - M\delta[n_\gamma] \\
\langle\delta[\Delta n_e]^2\rangle &= (1-M)^2\langle\delta^2[n_e]\rangle + M^2\langle\delta^2[n_\gamma]\rangle - 2M(1-M)\cancelto{0}{\langle\delta[n_e]\delta[n_\gamma]\rangle} \\
\chi^2 &\equiv Var\left(\Delta n_e\right) = \langle\delta[\Delta n_e]^2\rangle.
\end{aligned} \tag{A.4.1}$$

Making use of the uncorrelated nature of S1 and S2 fluctuations in order to take terms in equation (A.4.1) to zero.

A.5 Conclusion

Centroid subtraction provides a valuable technique for handling increased width in observed distributions due to binning where the underlying centroid value is changing across the bin-size, especially useful when dealing with finite statistics. The main limitation of the method is often finding accurate derivatives of the underlying centroid, the affect of which can be observed as oscillations with negative correlation in the example of the LUX discriminant versus energy.

Bibliography

[1] F H Oort. The force exerted by the stellar system in the direction perpendicular to the galactic plane and some related problems. *Buletin of the Astronomical Institues of the Netherlands*, VI.(238):1–39, August 1932.

[2] F Zwicky. On the Masses of Nebulae and of Clusters of Nebulae. *The Astrophysical Journal*, 86:217–246, October 1937.

[3] Ryan J Cooke, Max Pettini, Regina A Jorgenson, Michael T Murphy, and Charles C Steidel. Precision Measures of the Primordial Abundance of Deuterium. *The Astrophysical Journal*, 781(1):31, January 2014.

[4] E Komatsu, K M Smith, J Dunkley, C L Bennett, B Gold, G Hinshaw, N Jarosik, D Larson, M R Nolta, L Page, D N Spergel, M Halpern, R S Hill, A Kogut, M Limon, S S Meyer, N Odegard, G S Tucker, J L Weiland, E Wollack, and E L Wright. Seven-year Wilkinson Microwave Anisotropy Probe (WMAP) Observations: Cosmological Interpretation. *The Astrophysical Journal Supplement Series*, 192(2):18, February 2011.

[5] D Larson, J Dunkley, G Hinshaw, E Komatsu, M R Nolta, C L Bennett, B Gold, M Halpern, R S Hill, N Jarosik, A Kogut, M Limon, S S Meyer, N Odegard, L Page, K M Smith, D N Spergel, G S Tucker, J L Weiland, E Wollack, and E L Wright. Seven-year Wilkinson Microwave Anisotropy Probe (WMAP) Observations: Power Spectra and WMAP-derived Parameters. *The Astrophysical Journal Supplement Series*, 192(2):16, February 2011.

[6] N Jarosik, C L Bennett, J Dunkley, B Gold, M R Greason, M Halpern, R S Hill, G Hinshaw, A Kogut, E Komatsu, D Larson, M Limon, S S Meyer,

M R Nolta, N Odegard, L Page, K M Smith, D N Spergel, G S Tucker, J L Weiland, E Wollack, and E L Wright. Seven-year Wilkinson Microwave Anisotropy Probe (WMAP) Observations: Sky Maps, Systematic Errors, and Basic Results. *The Astrophysical Journal Supplement Series*, 192(2):14, February 2011.

[7] Will J Percival, Beth A Reid, Daniel J Eisenstein, Neta A Bahcall, Tamas Budavari, Joshua A Frieman, Masataka Fukugita, James E Gunn, Željko Ivezić, Gillian R Knapp, Richard G Kron, Jon Loveday, Robert H Lupton, Timothy A McKay, Avery Meiksin, Robert C Nichol, Adrian C Pope, David J Schlegel, Donald P Schneider, David N Spergel, Chris Stoughton, Michael A Strauss, Alexander S Szalay, Max Tegmark, Michael S Vogeley, David H Weinberg, Donald G York, and Idit Zehavi. Baryon acoustic oscillations in the Sloan Digital Sky Survey Data Release 7 galaxy sample. *Monthly Notices of the Royal Astronomical Society*, 401(4):2148–2168, February 2010.

[8] Donald G York, J Adelman, Jr John E Anderson, Scott F Anderson, James Annis, Neta A Bahcall, J A Bakken, Robert Barkhouser, Steven Bastian, Eileen Berman, William N Boroski, Steve Bracker, Charlie Briegel, John W Briggs, J Brinkmann, Robert Brunner, Scott Burles, Larry Carey, Michael A Carr, Francisco J Castander, Bing Chen, Patrick L Colestock, A J Connolly, J H Crocker, István Csabai, Paul C Czarapata, John Eric Davis, Mamoru Doi, Tom Dombeck, Daniel Eisenstein, Nancy Ellman, Brian R Elms, Michael L Evans, Xiaohui Fan, Glenn R Federwitz, Larry Fiscelli, Scott Friedman, Joshua A Frieman, Masataka Fukugita, Bruce Gillespie, James E Gunn, Vijay K Gurbani, Ernst de Haas, Merle Haldeman, Frederick H Harris, J Hayes, Timothy M Heckman, G S Hennessy, Robert B Hindsley, Scott Holm, Donald J Holmgren, Chi-hao Huang, Charles Hull, Don Husby, Shin-Ichi Ichikawa, Takashi Ichikawa, Željko Ivezić, Stephen Kent, Rita S J Kim, E Kinney, Mark Klaene, A N Kleinman, S Kleinman, G R Knapp, John Korienek, Richard G Kron, Peter Z Kunszt, D Q Lamb, B Lee, R French Leger, Siriluk Limmongkol, Carl Lindenmeyer, Daniel C Long, Craig Loomis, Jon Loveday, Rich Lucinio, Robert H Lupton, Bryan MacKinnon, Edward J Mannery, P M Mantsch, Bruce Margon, Peregrine McGehee, Timothy A McKay, Avery Meiksin, Aronne Merelli, David G Monet, Jeffrey A Munn,

Vijay K Narayanan, Thomas Nash, Eric Neilsen, Rich Neswold, Heidi Jo Newberg, R C Nichol, Tom Nicinski, Mario Nonino, Norio Okada, Sadanori Okamura, Jeremiah P Ostriker, Russell Owen, A George Pauls, John Peoples, R L Peterson, Donald Petravick, Jeffrey R Pier, Adrian Pope, Ruth Pordes, Angela Prosapio, Ron Rechenmacher, Thomas R Quinn, Gordon T Richards, Michael W Richmond, Claudio H Rivetta, Constance M Rockosi, Kurt Ruthmansdorfer, Dale Sandford, David J Schlegel, Donald P Schneider, Maki Sekiguchi, Gary Sergey, Kazuhiro Shimasaku, Walter A Siegmund, Stephen Smee, J Allyn Smith, S Snedden, R Stone, Chris Stoughton, Michael A Strauss, Christopher Stubbs, Mark SubbaRao, Alexander S Szalay, Istvan Szapudi, Gyula P Szokoly, Anirudda R Thakar, Christy Tremonti, Douglas L Tucker, Alan Uomoto, Dan Vanden Berk, Michael S Vogeley, Patrick Waddell, Shu-i Wang, Masaru Watanabe, David H Weinberg, Brian Yanny, and Naoki Yasuda. The Sloan Digital Sky Survey: Technical Summary. *The Astronomical Journal*, 120(3):1579–1587, September 2000.

[9] Peter Kernan and Lawrence Krauss. Refined big bang nucleosynthesis constraints on ΩB and Nν. *Physical Review Letters*, 72(21):3309–3312, May 1994.

[10] Timothy Clifton, Pedro G Ferreira, Antonio Padilla, and Constantinos Skordis. Modified Gravity and Cosmology. June 2011.

[11] M Milgrom. A modification of the Newtonian dynamics as a possible alternative to the hidden mass hypothesis. *The Astrophysical Journal*, 270: 365–370, July 1983.

[12] Benoit Famaey and Stacy S McGaugh. Modified Newtonian Dynamics (MOND): Observational Phenomenology and Relativistic Extensions. *Living Reviews in Relativity*, 15, 2012.

[13] S Shapiro, J Davis, D Lebach, and J Gregory. Measurement of the Solar Gravitational Deflection of Radio Waves using Geodetic Very-Long-Baseline Interferometry Data, 1979–1999. *Physical Review Letters*, 92(12):121101, March 2004.

[14] M Markevitch, A H Gonzalez, D Clowe, A Vikhlinin, W Forman, C Jones, S Murray, and W Tucker. Direct Constraints on the Dark Matter Self-Interaction Cross Section from the Merging Galaxy Cluster 1E 0657–56. *The Astrophysical Journal*, 606(2):819–824, May 2004.

[15] Planck Collaboration, P A R Ade, N Aghanim, C Armitage-Caplan, M Arnaud, M Ashdown, F Atrio-Barandela, J Aumont, C Baccigalupi, A J Banday, R B Barreiro, J G Bartlett, E Battaner, K Benabed, A Benoît, A Benoit-Lévy, J P Bernard, M Bersanelli, P Bielewicz, J Bobin, J J Bock, A Bonaldi, J R Bond, J Borrill, F R Bouchet, M Bridges, M Bucher, C Burigana, R C Butler, E Calabrese, B Cappellini, J F Cardoso, A Catalano, A Challinor, A Chamballu, R R Chary, X Chen, H C Chiang, L Y Chiang, P R Christensen, S Church, D L Clements, S Colombi, Colombo, L. P. L., F Couchot, A Coulais, B P Crill, A Curto, F Cuttaia, L Danese, R D Davies, R J Davis, P de Bernardis, A de Rosa, G de Zotti, J Delabrouille, J M Delouis, F X Désert, C Dickinson, J M Diego, K Dolag, H Dole, S Donzelli, O Doré, M Douspis, J Dunkley, X Dupac, G Efstathiou, F Elsner, T A Enßlin, H K Eriksen, F Finelli, O Forni, M Frailis, A A Fraisse, E Franceschi, T C Gaier, S Galeotta, S Galli, K Ganga, M Giard, G Giardino, Y Giraud-Héraud, E Gjerløw, J González-Nuevo, K M Górski, S Gratton, A Gregorio, A Gruppuso, J E Gudmundsson, J Haissinski, J Hamann, F K Hansen, D Hanson, D Harrison, S Henrot-Versille, C Hernández-Monteagudo, D Herranz, S R Hildebrandt, and E Hivon. Planck 2013 results. XVI. Cosmological parameters. *arXiv.org*, March 2013.

[16] Fabian Walter, Elias Brinks, W J G de Blok, Frank Bigiel, Robert C Kennicutt Jr, Michele D Thornley, and Adam Leroy. THINGS: The H I Nearby Galaxy Survey. *The Astronomical Journal*, 136(6):2563–2647, December 2008.

[17] Daniel J Eisenstein, Idit Zehavi, David W Hogg, Roman Scoccimarro, Michael R Blanton, Robert C Nichol, Ryan Scranton, Hee-Jong Seo, Max Tegmark, Zheng Zheng, Scott F Anderson, Jim Annis, Neta Bahcall, Jon Brinkmann, Scott Burles, Francisco J Castander, Andrew Connolly, István Csabai, Mamoru Doi, Masataka Fukugita, Joshua A Frieman, Karl Glazebrook, James E Gunn, John S Hendry, Gregory Hennessy, Željko Ivezić,

Stephen Kent, Gillian R Knapp, Huan Lin, Yeong-Shang Loh, Robert H Lupton, Bruce Margon, Timothy A McKay, Avery Meiksin, Jeffery A Munn, Adrian Pope, Michael W Richmond, David Schlegel, Donald P Schneider, Kazuhiro Shimasaku, Christopher Stoughton, Michael A Strauss, Mark SubbaRao, Alexander S Szalay, Istvan Szapudi, Douglas L Tucker, Brian Yanny, and Donald G York. Detection of the Baryon Acoustic Peak in the Large-Scale Correlation Function of SDSS Luminous Red Galaxies. *The Astrophysical Journal*, 633(2):560–574, November 2005.

[18] D J Fixsen. The Temperature of the Cosmic Microwave Background. *arXiv*, November 2009.

[19] M Limousin, J Richard, J P Kneib, H Brink, R Pello, E Jullo, H Tu, J Sommer-Larsen, E Egami, M J Michalowski, R Cabanac, and D P Stark. Strong Lensing in Abell 1703: Constraints on the Slope of the Inner Dark Matter Distribution. *Astronomy and Astrophysics*, (1):23–35, February 2008.

[20] Nobuhiro Okabe, Toshifumi Futamase, Masaru Kajisawa, and Risa Kuroshima. Subaru Weak-Lensing Survey of Dark Matter Subhalos in the Coma Cluster : Subhalo Mass Function and Statistical Properties. *arXiv*, April 2013.

[21] Douglas Clowe, Maruša Bradač, Anthony H Gonzalez, Maxim Markevitch, Scott W Randall, Christine Jones, and Dennis Zaritsky. A Direct Empirical Proof of the Existence of Dark Matter. *The Astrophysical Journal Letters*, 648(2):L109–L113, September 2006.

[22] Q Ahmad, R Allen, T Andersen, J D Anglin, J Barton, E Beier, M Bercovitch, J Bigu, S Biller, R Black, I Blevis, R Boardman, J Boger, E Bonvin, M Boulay, M Bowler, T Bowles, S Brice, M Browne, T Bullard, G Bühler, J Cameron, Y Chan, H Chen, M Chen, X Chen, B Cleveland, E Clifford, J Cowan, D Cowen, G Cox, X Dai, F Dalnoki-Veress, W Davidson, P Doe, G Doucas, M Dragowsky, C Duba, F Duncan, M Dunford, J Dunmore, E Earle, S Elliott, H Evans, G Ewan, J Farine, H Fergani, A Ferraris, R Ford, J Formaggio, M Fowler, K Frame, E Frank, W Frati, N Gagnon, J Germani, S Gil, K Graham, D Grant, R Hahn, A Hallin,

E Hallman, A Hamer, A Hamian, W Handler, R Haq, C Hargrove, P Harvey, R Hazama, K Heeger, W Heintzelman, J Heise, R Helmer, J Hepburn, H Heron, J Hewett, A Hime, M Howe, J Hykawy, M Isaac, P Jagam, N Jelley, C Jillings, G Jonkmans, K Kazkaz, P Keener, J Klein, A Knox, R Komar, R Kouzes, T Kutter, C Kyba, J Law, I Lawson, M Lay, H Lee, K Lesko, J Leslie, I Levine, W Locke, S Luoma, J Lyon, S Majerus, H Mak, J Maneira, J Manor, A Marino, N McCauley, A McDonald, D McDonald, K McFarlane, G McGregor, R Meijer Drees, C Mifflin, G Miller, G Milton, B Moffat, M Moorhead, C Nally, M Neubauer, F Newcomer, H Ng, A Noble, E Norman, V Novikov, M O'Neill, C Okada, R Ollerhead, M Omori, J Orrell, S Oser, A Poon, T Radcliffe, A Roberge, B Robertson, R Robertson, S Rosendahl, J Rowley, V Rusu, E Saettler, K Schaffer, M Schwendener, A Schülke, H Seifert, M Shatkay, J Simpson, C Sims, D Sinclair, P Skensved, A Smith, M Smith, T Spreitzer, N Starinsky, T Steiger, R Stokstad, L Stonehill, R Storey, B Sur, R Tafirout, N Tagg, N Tanner, R Taplin, M Thorman, P Thornewell, P Trent, Y Tserkovnyak, R Van Berg, R Van de Water, C Virtue, C Waltham, J X Wang, D Wark, N West, J Wilhelmy, J Wilkerson, J Wilson, P Wittich, J Wouters, and M Yeh. Direct Evidence for Neutrino Flavor Transformation from Neutral-Current Interactions in the Sudbury Neutrino Observatory. *Physical Review Letters*, 89(1):011301, June 2002.

[23] George R Blumenthal, S M Faber, Joel R Primack, and Martin J Rees. Formation of galaxies and large-scale structure with cold dark matter. *Nature*, 311(5986):517–525, October 1984.

[24] Leanne D Duffy and Karl van Bibber. Axions as dark matter particles. *New Journal of Physics*, 11(10):105008, October 2009.

[25] C A Baker, D D Doyle, P Geltenbort, K Green, M G D van der Grinten, P G Harris, P Iaydjiev, S N Ivanov, D J R May, J M Pendlebury, J D Richardson, D Shiers, and K F Smith. Improved Experimental Limit on the Electric Dipole Moment of the Neutron. *Physical Review Letters*, 97(13):131801, September 2006.

[26] P Sikivie. Experimental Tests of the "Invisible" Axion. *Physical Review Letters*, 51(16):1415–1417, October 1983.

[27] Richard Lynn Davis. Goldstone bosons in string models of galaxy formation. *Physical Review D*, 32(12):3172–3177, December 1985.

[28] R L Davis. Cosmic axions from cosmic strings. *Physics Letters B*, 180(3): 225–230, November 1986.

[29] David H Lyth. Estimates of the cosmological axion density. *Physics Letters B*, 275(3-4):279–283, January 1992.

[30] S Chang and P Sikivie. Studies of the motion and decay of axion walls bounded by strings. *Physical Review D*, 59(2):023505, December 1998.

[31] John Preskill, Mark B Wise, and Frank Wilczek. Cosmology of the invisible axion. *Physics Letters B*, 120(1-3):127–132, January 1983.

[32] S J Asztalos, G Carosi, C Hagmann, D Kinion, K van Bibber, M Hotz, L J Rosenberg, G Rybka, J Hoskins, J Hwang, P Sikivie, D B Tanner, R Bradley, and J Clarke. SQUID-Based Microwave Cavity Search for Dark-Matter Axions. *Physical Review Letters*, 104(4):041301, January 2010.

[33] E Arik, S Aune, D Autiero, K Barth, A Belov, B Beltrán, S Borghi, G Bourlis, F S Boydag, H Bräuninger, J M Carmona, S Cebrián, S A Cetin, J I Collar, T Dafni, M Davenport, L Di Lella, O B Dogan, C Eleftheriadis, N Elias, G Fanourakis, E Ferrer-Ribas, H Fischer, P Friedrich, J Franz, J Galán, T Geralis, I Giomataris, S Gninenko, H Gómez, R Hartmann, M Hasinoff, F H Heinsius, I Hikmet, D H H Hoffmann, I G Irastorza, J Jacoby, K Jakovčić, D Kang, K Königsmann, R Kotthaus, M Krčmar, K Kousouris, M Kuster, B Lakić, C Lasseur, A Liolios, A Ljubičić, G Lutz, G Luzón, D Miller, J Morales, T Niinikoski, A Nordt, A Ortiz, T Papaevangelou, M J Pivovaroff, A Placci, G Raffelt, H Riege, A Rodríguez, J Ruz, I Savvidis, Y Semertzidis, P Serpico, R Soufli, L Stewart, K van Bibber, J Villar, J Vogel, L Walckiers, and K Zioutas. Probing eV-scale axions with CAST. *Journal of Cosmology and Astroparticle Physics*, 2009(02):008–008, February 2009.

[34] S Andriamonje, S Aune, D Autiero, K Barth, A Belov, B Beltrán, H Bräuninger, J M Carmona, S Cebrián, J I Collar, T Dafni, M Davenport, L Di Lella, C Eleftheriadis, J Englhauser, G Fanourakis, E Ferrer Ribas, H Fischer, J Franz, P Friedrich, T Geralis, I Giomataris, S Gninenko, H Gómez, M Hasinoff, F H Heinsius, D H H Hoffmann, I G Irastorza, J Jacoby, K Jakovčić, D Kang, K Königsmann, R Kotthaus, M Krčmar, K Kousouris, M Kuster, B Lakić, C Lasseur, A Liolios, A Ljubičić, G Lutz, G Luzón, D Miller, A Morales, J Morales, A Ortiz, T Papaevangelou, A Placci, G Raffelt, H Riege, A Rodríguez, J Ruz, I Savvidis, Y Semertzidis, P Serpico, L Stewart, J Vieira, J Villar, J Vogel, L Walckiers, K Zioutas, and CAST Collaboration. An improved limit on the axion–photon coupling from the CAST experiment. *Journal of Cosmology and Astroparticle Physics*, 2007(04):010–010, April 2007.

[35] Gerard Jungman, Marc Kamionkowski, and Kim Griest. Supersymmetric dark matter. *Physics Reports*, 267(5-6):195–373, March 1996.

[36] O Adriani, G C Barbarino, G A Bazilevskaya, R Bellotti, M Boezio, E A Bogomolov, L Bonechi, M Bongi, V Bonvicini, and S Borisov. A statistical procedure for the identification of positrons in the PAMELA experiment. *Astroparticle Physics*, 34(1):1–11, August 2010.

[37] M Aguilar, G Alberti, B Alpat, A Alvino, G Ambrosi, K Andeen, H Anderhub, L Arruda, P Azzarello, A Bachlechner, F Barao, B Baret, A Barrau, L Barrin, A Bartoloni, L Basara, A Basili, L Batalha, J Bates, R Battiston, J Bazo, R Becker, U Becker, M Behlmann, B Beischer, J Berdugo, P Berges, B Bertucci, G Bigongiari, A Biland, V Bindi, S Bizzaglia, G Boella, W de Boer, K Bollweg, J Bolmont, B Borgia, S Borsini, M Boschini, G Boudoul, M Bourquin, P Brun, M Buénerd, J Burger, W Burger, F Cadoux, X Cai, M Capell, D Casadei, J Casaus, V Cascioli, G Castellini, I Cernuda, F Cervelli, M Chae, Y Chang, A Chen, C Chen, H Chen, G Cheng, H Chen, L Cheng, N Chernoplyiokov, A Chikanian, E Choumilov, V Choutko, C Chung, C Clark, R Clavero, G Coignet, V Commichau, C Consolandi, A Contin, C Corti, M Costado Dios, B Coste, D Crespo, Z Cui, M Dai, C Delgado, S Della Torre, B Demirkoz, P Dennett, L Derome, S Di Falco, X Diao, A Diago, L Djambazov, C Díaz, P von Doetinchem,

W Du, J Dubois, R Duperay, M Duranti, D D'Urso, A Egorov, A Eline, F Eppling, T Eronen, J van Es, H Esser, A Falvard, E Fiandrini, A Fiasson, E Finch, P Fisher, K Flood, R Foglio, M Fohey, S Fopp, N Fouque, Y Galaktionov, M Gallilee, L Gallin-Martel, G Gallucci, B García, J García, R García-López, L García-Tabares, C Gargiulo, H Gast, I Gebauer, S Gentile, M Gervasi, W Gillard, F Giovacchini, L Girard, P Goglov, J Gong, C Goy-Henningsen, D Grandi, M Graziani, A Grechko, A Gross, I Guerri, C de la Guía, K Guo, M Habiby, S Haino, F Hauler, Z He, M Heil, J Heilig, R Hermel, H Hofer, Z Huang, W Hungerford, M Incagli, M Ionica, A Jacholkowska, W Jang, H Jinchi, M Jongmanns, L Journet, L Jungermann, W Karpinski, G Kim, K Kim, Th Kirn, R Kossakowski, A Koulemzine, O Kounina, A Kounine, V Koutsenko, M Krafczyk, E Laudi, G Laurenti, C Lauritzen, A Lebedev, M Lee, S Lee, C Leluc, H León Vargas, V Lepareur, J Li, Q Li, T Li, W Li, Z Li, P Lipari, C Lin, D Liu, H Liu, T Lomtadze, Y Lu, S Lucidi, K Lübelsmeyer, J Luo, W Lustermann, S Lv, J Madsen, R Majka, A Malinin, C Mañá, J Marín, T Martin, G Martínez, F Masciocchi, N Masi, D Maurin, A McInturff, P McIntyre, A Menchaca-Rocha, Q Meng, M Menichelli, I Mereu, M Millinger, D Mo, M Molina, P Mott, A Mujunen, S Natale, P Nemeth, J Ni, N Nikonov, F Nozzoli, P Nunes, A Obermeier, S Oh, A Oliva, F Palmonari, C Palomares, M Paniccia, A Papi, W Park, M Pauluzzi, F Pauss, A Pauw, E Pedreschi, S Pensotti, R Pereira, E Perrin, G Pessina, G Pierschel, F Pilo, A Piluso, C Pizzolotto, V Plyaskin, J Pochon, M Pohl, V Poireau, S Porter, J Pouxe, A Putze, L Quadrani, X Qi, P Rancoita, D Rapin, Z Ren, J Ricol, E Riihonen, I Rodríguez, U Roeser, S Rosier-Lees, L Rossi, A Rozhkov, D Rozza, A Sabellek, R Sagdeev, J Sandweiss, B Santos, P Saouter, M Sarchioni, S Schael, D Schinzel, M Schmanau, G Schwering, A Schulz von Dratzig, G Scolieri, E Seo, B Shan, J Shi, Y Shi, T Siedenburg, R Siedling, D Son, F Spada, F Spinella, M Steuer, K Stiff, W Sun, W Sun, X Sun, M Tacconi, C Tang, X Tang, Z Tang, L Tao, J Tassan-Viol, Samuel Ting, S Ting, C Titus, N Tomassetti, F Toral, J Torsti, J Tsai, J Tutt, J Ulbricht, T Urban, V Vagelli, E Valente, C Vannini, E Valtonen, M Vargas Trevino, S Vaurynovich, M Vecchi, M Vergain, B Verlaat, C Vescovi, J Vialle, G Viertel, G Volpini, D Wang, N Wang, Q Wang, R Wang, X Wang, Z Wang, W Wallraff, Z Weng, M Willenbrock, and M... Wlochal. First Result from the Alpha Magnetic Spectrometer on the International Space Station: Precision Measurement of the Positron Fraction in Primary Cosmic Rays of 0.5–350 GeV. *Physical Review Letters*, 110 (14):141102, April 2013.

[38] Fermi-LAT Collaboration, M Ackermann, M Ajello, A Albert, L Baldini, G Barbiellini, K Bechtol, R Bellazzini, B Berenji, R D Blandford, E D Bloom, E Bonamente, A W Borgland, M Brigida, R Buehler, S Buson, G A Caliandro, R A Cameron, P A Caraveo, J M Casandjian, C Cecchi, E Charles, A Chekhtman, J Chiang, S Ciprini, R Claus, J Cohen-Tanugi, J Conrad, F D'Ammando, F de Palma, C D Dermer, E do Couto e Silva, P S Drell, A Drlica-Wagner, Y Edmonds, R Essig, C Favuzzi, S J Fegan, Y Fukazawa, S Funk, P Fusco, F Gargano, D Gasparrini, S Germani, N Giglietto, F Giordano, M Giroletti, T Glanzman, G Godfrey, I A Grenier, S Guiriec, M Gustafsson, D Hadasch, M Hayashida, D Horan, R E Hughes, T Kamae, J Knödlseder, M Kuss, J Lande, A M Lionetto, M Llena Garde, F Longo, F Loparco, M N Lovellette, P Lubrano, M N Mazziotta, P F Michelson, W Mitthumsiri, T Mizuno, A A Moiseev, C Monte, M E Monzani, A Morselli, I V Moskalenko, S Murgia, M Naumann-Godo, J P Norris, E Nuss, T Ohsugi, A Okumura, E Orlando, J F Ormes, D Paneque, J H Panetta, M Pesce-Rollins, F Piron, G Pivato, T A Porter, D Prokhorov, S Rainò, R Rando, M Razzano, O Reimer, M Roth, C Sbarra, J D Scargle, C Sgrò, and E J Siskind. Fermi LAT Search for Dark Matter in Gamma-ray Lines and the Inclusive Photon Spectrum. *arXiv*, May 2012.

[39] Dan Hooper. Indirect Searches For Dark Matter: Signals, Hints and Otherwise. *arXiv*, October 2007.

[40] G Aad, T Abajyan, B Abbott, J Abdallah, S Abdel Khalek, O Abdinov, R Aben, B Abi, M Abolins, O S AbouZeid, H Abramowicz, H Abreu, Y Abulaiti, B S Acharya, L Adamczyk, D L Adams, T N Addy, J Adelman, S Adomeit, T Adye, S Aefsky, T Agatonovic-Jovin, J A Aguilar-Saavedra, M Agustoni, S P Ahlen, A Ahmad, F Ahmadov, M Ahsan, G Aielli, T P A Åkesson, G Akimoto, A V Akimov, M A Alam, J Albert, S Albrand, M J Alconada Verzini, M Aleksa, I N Aleksandrov, F Alessandria, C Alexa,

G Alexander, G Alexandre, T Alexopoulos, M Alhroob, M Aliev, G Alimonti, L Alio, J Alison, B M M Allbrooke, L J Allison, P P Allport, S E Allwood-Spiers, J Almond, A Aloisio, R Alon, A Alonso, F Alonso, A Altheimer, B Alvarez Gonzalez, M G Alviggi, K Amako, Y Amaral Coutinho, C Amelung, V V Ammosov, S P Amor Dos Santos, A Amorim, S Amoroso, N Amram, G Amundsen, C Anastopoulos, L S Ancu, N Andari, T Andeen, C F Anders, G Anders, K J Anderson, A Andreazza, V Andrei, X S Anduaga, S Angelidakis, P Anger, A Angerami, F Anghinolfi, A V Anisenkov, N Anjos, A Annovi, A Antonaki, M Antonelli, A Antonov, J Antos, F Anulli, M Aoki, L Aperio Bella, R Apolle, G Arabidze, I Aracena, Y Arai, A T H Arce, S Arfaoui, J-F Arguin, S Argyropoulos, E Arik, M Arik, A J Armbruster, O Arnaez, V Arnal, O Arslan, A Artamonov, G Artoni, S Asai, N Asbah, S Ask, B Åsman, L Asquith, K Assamagan, R Astalos, A Astbury, M Atkinson, N B Atlay, B Auerbach, E Auge, K Augsten, M Aurousseau, G Avolio, G Azuelos, Y Azuma, M A Baak, C Bacci, A M Bach, H Bachacou, K Bachas, M Backes, M Backhaus, J Backus Mayes, E Badescu, P Bagiacchi, P Bagnaia, Y Bai, D C Bailey, T Bain, J T Baines, O K Baker, S Baker, P Balek, F Balli, E Banas, Sw Banerjee, D Banfi, A Bangert, V Bansal, H S Bansil, L Barak, S P Baranov, T Barber, E L Barberio, D Barberis, M Barbero, D Y Bardin, T Barillari, M Barisonzi, T Barklow, N Barlow, B M Barnett, R M Barnett, A Baroncelli, G Barone, A J Barr, F Barreiro, J Barreiro Guimarães da Costa, R Bartoldus, A E Barton, V Bartsch, A Bassalat, A Basye, R L Bates, L Batkova, J R Batley, M Battistin, F Bauer, H S Bawa, T Beau, P H Beauchemin, R Beccherle, P Bechtle, H P Beck, K Becker, S Becker, M Beckingham, A J Beddall, A Beddall, S Bedikian, V A Bednyakov, C P Bee, L J Beemster, T A Beermann, M Begel, K Behr, C Belanger-Champagne, P J Bell, W H Bell, G Bella, L Bellagamba, A Bellerive, M Bellomo, A Belloni, O L Beloborodova, K Belotskiy, O Beltramello, O Benary, D Benchekroun, K Bendtz, N Benekos, Y Benhammou, E Benhar Noccioli, J A Benitez Garcia, D P Benjamin, J R Bensinger, K Benslama, S Bentvelsen, D Berge, E Bergeaas Kuutmann, N Berger, F Berghaus, E Berglund, J Beringer, C Bernard, P Bernat, R Bernhard, C Bernius, F U Bernlochner, T Berry, P Berta, C Bertella, F Bertolucci, M I Besana, G J Besjes, O Bessidskaia, N Besson, S Bethke, W Bhimji, R M Bianchi, L Bianchini, M Bianco, O Biebel, S P Bieniek, K Bierwagen, J Biesiada, M Biglietti, J Bilbao De Mendizabal, H Bilokon, M Bindi, S Binet, A Bingul, C Bini, B Bittner, C W Black, J E Black, K M Black, D Blackburn, R E Blair, J B Blanchard, T Blazek, I Bloch, C Blocker, J Blocki, W Blum, U Blumenschein, G J Bobbink, V S Bobrovnikov, S S Bocchetta, A Bocci, C R Boddy, M Boehler, J Boek, T T Boek, N Boelaert, J A Bogaerts, A G Bogdanchikov, A Bogouch, C Bohm, J Bohm, V Boisvert, T Bold, V Boldea, A S Boldyrev, N M Bolnet, M Bomben, M Bona, M Boonekamp, S Bordoni, C Borer, A Borisov, G Borissov, M Borri, S Borroni, J Bortfeldt, V Bortolotto, K Bos, D Boscherini, M Bosman, and ... Boterenbrood. Search for Dark Matter in Events with a Hadronically Decaying W or Z Boson and Missing Transverse Momentum in pp Collisions at $\sqrt{s}$=8 TeV with the ATLAS Detector. *Physical Review Letters*, 112(4):041802, January 2014.

[41] J D Lewin and P F Smith. Review of mathematics, numerical factors, and corrections for dark matter experiments based on elastic nuclear recoil. *Astroparticle Physics*, 1996.

[42] Richard Helm. Inelastic and Elastic Scattering of 187-Mev Electrons from Selected Even-Even Nuclei. *Phys. Rev.*, 104(5):1466–1475, December 1956.

[43] D S Akerib, H M Araujo, X Bai, A J Bailey, J Balajthy, E Bernard, A Bernstein, A Bradley, D Byram, S B Cahn, M C Carmona-Benitez, C Chan, J J Chapman, A A Chiller, C Chiller, T Coffey, A Currie, L de Viveiros, A Dobi, J Dobson, E Druszkiewicz, B Edwards, C H Faham, S Fiorucci, C Flores, R J Gaitskell, V M Gehman, C Ghag, K R Gibson, M G D Gilchriese, C Hall, S A Hertel, M Horn, D Q Huang, M Ihm, R G Jacobsen, K Kazkaz, R Knoche, N A Larsen, C Lee, A Lindote, M I Lopes, D C Malling, R Mannino, D N McKinsey, D M Mei, J Mock, M Moongweluwan, J Morad, A St J Murphy, C Nehrkorn, H Nelson, F Neves, R A Ott, M Pangilinan, P D Parker, E K Pease, K Pech, P Phelps, L Reichhart, T Shutt, C Silva, V N Solovov, P Sorensen, K O'Sullivan, T J Sumner, M Szydagis, D Taylor, B Tennyson, D R Tiedt, M Tripathi, S Uvarov, J R Verbus, N Walsh, R Webb, J T White, M S Witherell, F L H Wolfs, M Woods, and C Zhang. Radiogenic and Muon-Induced Backgrounds in the LUX Dark Matter Detector. *arXiv*, March 2014. URL `http://arxiv.org/abs/1403.1299`.

[44] Katherine Freese, Mariangela Lisanti, and Christopher Savage. Annual Modulation of Dark Matter: A Review. *arXiv*, September 2012.

[45] R Bernabei, P Belli, F Cappella, R Cerulli, C J Dai, A d'Angelo, H L He, A Incicchitti, H H Kuang, J M Ma, F Montecchia, F Nozzoli, D Prosperi, X D Sheng, and Z P Ye. First results from DAMA/LIBRA and the combined results with DAMA/NaI. *The European Physical Journal C*, 56(3):333–355, August 2008.

[46] The XENON100 Collaboration, E Aprile, K Arisaka, F Arneodo, A Askin, L Baudis, A Behrens, E Brown, J M R Cardoso, B Choi, D B Cline, S Fattori, A D Ferella, K L Giboni, K Hugenberg, A Kish, C W Lam, J Lamblin, R F Lang, K E Lim, J A M Lopes, T Marrodan Undagoitia, Y Mei, A J Melgarejo Fernandez, K Ni, U Oberlack, S E A Orrigo, E Pantic, G Plante, A C C Ribeiro, R Santorelli, J M F dos Santos, M Schumann, P Shagin, A Teymourian, D Thers, E Tziaferi, H Wang, and C Weinheimer. First Dark Matter Results from the XENON100 Experiment. *Physical Review Letters*, (13), May 2010. URL http://arxiv.org/abs/1005.0380.

[47] S. Akerib, D. M. Araújo, H. X. Bai, J. Bailey, A. J. Balajthy, S. Bedikian, E. Bernard, A. Bernstein, A. Bolozdynya, A. Bradley, D. Byram, B. Cahn, S. C. Carmona-Benitez, M. C. Chan, J. Chapman, J. A. Chiller, A. C. Chiller, K. Clark, T. Coffey, A. Currie, A. Curioni, S. Dazeley, L. de Viveiros, A. Dobi, J. Dobson, M. Dragowsky, E. E. Druszkiewicz, B. Edwards, H. Faham, C. S. Fiorucci, C. Flores, J. Gaitskell, R. M. Gehman, V. C. Ghag, R. Gibson, K. G.D̃. Gilchriese, M. C. Hall, M. Hanhardt, A. Hertel, S. M. Horn, Q. Huang, D. M. Ihm, G. Jacobsen, R. L. Kastens, K. Kazkaz, R. Knoche, S. Kyre, R. Lander, A. Larsen, N. C. Lee, S. Leonard, D. T. Lesko, K. A. Lindote, I. Lopes, M. A. Lyashenko, C. Malling, D. R. Mannino, N. McKinsey, D. D.-M. Mei, J. Mock, M. Moongweluwan, J. Morad, M. Morii, St.J̃. Murphy, A. C. Nehrkorn, H. Nelson, F. Neves, A. Nikkel, J. A. Ott, R. M. Pangilinan, D. Parker, P. K. Pease, E. K. Pech, P. Phelps, L. Reichhart, T. Shutt, C. Silva, W. Skulski, J. Sofka, C. N. Solovov, V. P. Sorensen, T. Stiegler, K. O'Sullivan, J. Sumner, T. R. Svoboda, M. Sweany, M. Szydagis, D. Taylor, B. Tennyson, R. Tiedt, D. M. Tripathi, S. Uvarov, R. Verbus, J. N. Walsh, R. Webb, T. White, J.

D. White, S. Witherell, M. M. Wlasenko, L.H̃. Wolfs, F. M. Woods, and C. Zhang. First results from the lux dark matter experiment at the sanford underground research facility. *Phys. Rev. Lett.*, 112:091303, Mar 2014. doi: 10.1103/PhysRevLett.112.091303. URL `http://link.aps.org/doi/10.1103/PhysRevLett.112.091303`.

[48] The CDMS Collaboration and Z Ahmed. Results from the Final Exposure of the CDMS II Experiment. *Science*, 327:16–19, December 2010. URL `http://arxiv.org/abs/0912.3592`.

[49] G Angloher, M Bauer, I Bavykina, A Bento, C Bucci, C Ciemniak, G Deuter, F von Feilitzsch, D Hauff, P Huff, C Isaila, J Jochum, M Kiefer, M Kimmerle, J C Lanfranchi, F Petricca, S Pfister, W Potzel, F Pröbst, F Reindl, S Roth, K Rottler, C Sailer, K Schäffner, J Schmaler, S Scholl, W Seidel, M von Sivers, L Stodolsky, C Strandhagen, R Strauß, A Tanzke, I Usherov, S Wawoczny, M Willers, and A Zöller. Results from 730 kgdays of the CRESST-II Dark Matter search. *The European Physical Journal C*, 72(4): 1–22, April 2012.

[50] J Lindhard, V Nielson, M Scharff, and P V Thomsen. Integral Equations Governing Radiation Effects. *Mat. Fys. Medd*, 33(10), 1963.

[51] C E Aalseth, P S Barbeau, J Colaresi, J I Collar, and J D Leon. CoGeNT: A search for low-mass dark matter using p-type point contact germanium detectors. *Physical Review D*, 2013.

[52] R Agnese, Z Ahmed, A Anderson, S Arrenberg, D Balakishiyeva, R Basu Thakur, D Bauer, J Billard, A Borgland, D Brandt, P Brink, T Bruch, R Bunker, B Cabrera, D Caldwell, D Cerdeno, H Chagani, J Cooley, B Cornell, C Crewdson, P Cushman, M Daal, F Dejongh, E do Couto e Silva, T Doughty, L Esteban, S Fallows, E Figueroa-Feliciano, J Filippini, J Fox, M Fritts, G Godfrey, S Golwala, J Hall, R Harris, S Hertel, T Hofer, D Holmgren, L Hsu, M Huber, A Jastram, O Kamaev, B Kara, M Kelsey, A Kennedy, P Kim, M Kiveni, K Koch, M Kos, S Leman, B Loer, E Lopez Asamar, R Mahapatra, V Mandic, C Martinez, K McCarthy, N Mirabolfathi, R Moffatt, D Moore, P Nadeau, R Nelson, K Page, R Partridge, M Pepin, A Phipps, K Prasad, M Pyle, H Qiu, W Rau, P Redl,

A Reisetter, Y Ricci, T Saab, B Sadoulet, J Sander, K Schneck, R Schnee, S Scorza, B Serfass, B Shank, D Speller, K Sundqvist, A Villano, B Welliver, D Wright, S Yellin, J Yen, J Yoo, B Young, J Zhang, and CDMS Collaboration. Silicon Detector Dark Matter Results from the Final Exposure of CDMS II. *Physical Review Letters*, 111(25):251301, December 2013.

[53] Nikhil Anand, A Liam Fitzpatrick, and W C Haxton. Model-independent Analyses of Dark-Matter Particle Interactions. *arXiv*, May 2014. URL `http://arxiv.org/abs/1405.6690`.

[54] R Agnese, A J Anderson, M Asai, D Balakishiyeva, R Basu Thakur, D A Bauer, J Billard, A Borgland, M A Bowles, D Brandt, P L Brink, R Bunker, B Cabrera, D O Caldwell, D G Cerdeno, H Chagani, J Cooley, B Cornell, C H Crewdson, P Cushman, M Daal, Di Stefano, P. C. F., T Doughty, L Esteban, S Fallows, E Figueroa-Feliciano, G L Godfrey, S R Golwala, J Hall, H R Harris, S A Hertel, T Hofer, D Holmgren, L Hsu, M E Huber, A Jastram, O Kamaev, B Kara, M H Kelsey, A Kennedy, M Kiveni, K Koch, B Loer, E Lopez Asamar, R Mahapatra, V Mandic, C Martinez, K A McCarthy, N Mirabolfathi, R A Moffatt, D C Moore, P Nadeau, R H Nelson, K Page, R Partridge, M Pepin, A Phipps, K Prasad, M Pyle, H Qiu, W Rau, P Redl, A Reisetter, Y Ricci, T Saab, B Sadoulet, J Sander, K Schneck, R W Schnee, S Scorza, B Serfass, B Shank, D Speller, A N Villano, B Welliver, D H Wright, S Yellin, J J Yen, B A Young, and J Zhang. CDMSlite: A Search for Low-Mass WIMPs using Voltage-Assisted Calorimetric Ionization Detection in the SuperCDMS Experiment. *Physical Review Letters*, (4):041302, September 2013. URL `http://arxiv.org/abs/1309.3259`.

[55] E Behnke, J I Collar, P S Cooper, K Crum, M Crisler, M Hu, I Levine, D Nakazawa, H Nguyen, B Odom, E Ramberg, J Rasmussen, N Riley, A Sonnenschein, M Szydagis, and R Tschirhart. Improved Spin-Dependent WIMP Limits from a Bubble Chamber. *Science*, (5865):933–936, April 2008.

[56] First dark matter search results from a 4-kg CF3I bubble chamber operated in a deep underground site. *Phys. Rev. D*, 86, 2012. URL `http://journals.aps.org/prd/abstract/10.1103/PhysRevD.86.052001`.

[57] P Gorel. Search for Dark Matter with Liquid Argon and Pulse Shape Discrimination: Results from DEAP-1 and Status of DEAP-3600. *arXiv*, June 2014.

[58] M G Boulay, B Cai, M Chen, V V Golovko, P Harvey, R Mathew, J J Lidgard, A B McDonald, P Pasuthip, T Pollman, P Skensved, K Graham, A L Hallin, D N McKinsey, W H Lippincott, J Nikkel, C J Jillings, F Duncan, B Cleveland, and I Lawson. Measurement of the scintillation time spectra and pulse-shape discrimination of low-energy beta and nuclear recoils in liquid argon with DEAP-1. *arXiv*, April 2009.

[59] T Doke, A Hitachi, S Kubota, A Nakamoto, and T Takahashi. Estimation of Fano factors in liquid argon, krypton, xenon and xenon-doped liquid argon. *Nuclear Instruments and Methods*, 134(2):353–357, April 1976.

[60] XENON100 Collaboration and E Aprile. Response of the XENON100 dark matter detector to nuclear recoils. *Physical Review D*, 2013.

[61] ArDM Collaboration, A Badertscher, F Bay, N Bourgeois, C Cantini, M Daniel, U Degunda, S DiLuise, L Epprecht, A Gendotti, S Horikawa, L Knecht, D Lussi, G Maire, B Montes, S Murphy, G Natterer, K Nikolics, K Nguyen, L Periale, S Ravat, F Resnati, L Romero, A Rubbia, R Santorelli, F Sergiampietri, D Sgalaberna, T Viant, and S Wu. Status of the ArDM Experiment: First results from gaseous argon operation in deep underground environment. *arXiv.org*, June 2013.

[62] P Cushman, C Galbiati, D N McKinsey, H Robertson, T M P Tait, D Bauer, A Borgland, B Cabrera, F Calaprice, J Cooley, T Empl, R Essig, E Figueroa-Feliciano, R Gaitskell, S Golwala, J Hall, R Hill, A Hime, E Hoppe, L Hsu, E Hungerford, R Jacobsen, M Kelsey, R F Lang, W H Lippincott, B Loer, S Luitz, V Mandic, J Mardon, J Maricic, R Maruyama, R Mahapatra, H Nelson, J Orrell, K Palladino, E Pantic, R Partridge, A Ryd, T Saab, B Sadoulet, R Schnee, W Shepherd, A Sonnenschein, P Sorensen, M Szydagis, T Volansky, M Witherell, D Wright, and K Zurek. Snowmass CF1 Summary: WIMP Dark Matter Direct Detection. October 2013. URL `http://arxiv.org/abs/131.8327`.

[63] A I Bolozdynya. Two-phase emission detectors and their applications. *Nuclear Instruments and Methods*, A442:314–320, January 1999.

[64] L Miller, S Howe, and W Spear. Charge Transport in Solid and Liquid Ar, Kr, and Xe. *Phys. Rev.*, 166(3):871–878, February 1968.

[65] C E Dahl. The physics of background discrimination in liquid xenon, and first results from Xenon10 in the hunt for WIMP dark matter. *Ph.D. thesis - Princeton*, pages 1–182, May 2009.

[66] D S Akerib, X Bai, S Bedikian, A Bernstein, A Bolozdynya, A Bradley, S Cahn, D Carr, J J Chapman, K Clark, T Classen, A Curioni, C E Dahl, S Dazeley, L deViveiros, M Dragowsky, E Druszkiewicz, S Fiorucci, R J Gaitskell, C Hall, C Faham, B Holbrook, L Kastens, K Kazkaz, J Kwong, R Lander, D Leonard, D Malling, R Mannino, D N McKinsey, D Mei, J Mock, M Morii, J Nikkel, P Phelps, T Shutt, W Skulski, P Sorensen, J Spaans, T Steigler, R Svoboda, M Sweany, J Thomson, M Tripathi, N Walsh, R Webb, J White, F L H Wolfs, M Woods, and C Zhang. The LUX Prototype Detector: Heat Exchanger Development. *arXiv.org*, July 2012. URL http://arxiv.org/abs/1207.3665v2.

[67] D S Akerib, X Bai, S Bedikian, E Bernard, A Bernstein, A Bradley, S B Cahn, M C Carmona-Benitez, D Carr, J J Chapman, Y-D Chan, K Clark, T Classen, T Coffey, S Dazeley, L deViveiros, M Dragowsky, E Druszkiewicz, C H Faham, S Fiorucci, R J Gaitskell, K R Gibson, C Hall, M Hanhardt, B Holbrook, M Ihm, R G Jacobsen, L Kastens, K Kazkaz, R Lander, N Larsen, C Lee, D Leonard, K Lesko, A Lyashenko, D C Malling, R Mannino, D McKinsey, D Mei, J Mock, M Morii, H Nelson, J A Nikkel, M Pangilinan, P D Parker, P Phelps, T Shutt, W Skulski, P Sorensen, J Spaans, T Stiegler, R Svoboda, A Smith, M Sweany, M Szydagis, J Thomson, M Tripathi, J R Verbus, N Walsh, R Webb, J T White, M Wlasenko, F L H Wolfs, M Woods, S Uvarov, and C Zhang. Radio-assay of Titanium samples for the LUX Experiment. *JINST*, physics.ins-det, 2011.

[68] M Yamashita, T Doke, K Kawasaki, J Kikuchi, and S Suzuki. Scintillation response of liquid Xe surrounded by PTFE reflector for gamma rays. *Nuclear*

Instruments and Methods in Physics Research Section A: Accelerators, Spectrometers, Detectors and Associated Equipment, 535(3):692–698, December 2004.

[69] D S Akerib, X Bai, E Bernard, A Bernstein, A Bradley, D Byram, S B Cahn, M C Carmona-Benitez, D Carr, J J Chapman, Y-D Chan, K Clark, T Coffey, L deViveiros, M Dragowsky, E Druszkiewicz, B Edwards, C H Faham, S Fiorucci, R J Gaitskell, K R Gibson, C Hall, M Hanhardt, B Holbrook, M Ihm, R G Jacobsen, L Kastens, K Kazkaz, N Larsen, C Lee, K Lesko, A Lindote, M I Lopes, A Lyashenko, D C Malling, R Mannino, D McKinsey, D Mei, J Mock, M Morii, H Nelson, F Neves, J A Nikkel, M Pangilinan, K Pech, P Phelps, T Shutt, C Silva, W Skulski, V N Solovov, P Sorensen, J Spaans, T Stiegler, M Sweany, M Szydagis, D Taylor, J Thomson, M Tripathi, S Uvarov, J R Verbus, N Walsh, R Webb, J T White, M Wlasenko, F L H Wolfs, M Woods, and C Zhang. An Ultra-Low Background PMT for Liquid Xenon Detectors. *arXiv.org*, May 2012. URL http://arxiv.org/abs/1205.2272v2.

[70] D S Akerib, X Bai, S Bedikian, E Bernard, A Bernstein, A Bradley, S B Cahn, M C Carmona-Benitez, D Carr, J J Chapman, K Clark, T Classen, T Coffey, A Curioni, S Dazeley, L deViveiros, M Dragowsky, E Druszkiewicz, C H Faham, S Fiorucci, R J Gaitskell, K R Gibson, C Hall, M Hanhardt, B Holbrook, M Ihm, R G Jacobsen, L Kastens, K Kazkaz, R Lander, N Larsen, C Lee, D Leonard, K Lesko, A Lyashenko, D C Malling, R Mannino, D N McKinsey, D Mei, J Mock, M Morii, H Nelson, J A Nikkel, M Pangilinan, P Phelps, T Shutt, W Skulski, P Sorensen, J Spaans, T Stiegler, R Svoboda, M Sweany, M Szydagis, J Thomson, M Tripathi, J R Verbus, N Walsh, R Webb, J T White, M Wlasenko, F L H Wolfs, M Woods, and C Zhang. Data Acquisition and Readout System for the LUX Dark Matter Experiment. *arXiv.org*, August 2011. URL http://arxiv.org/abs/1108.1836v2.

[71] Jochen Ahlswede, Simon Hebel, Martin B Kalinowski, and Jens Ole Roß. *Update of the global krypton-85 emission inventory*. Carl-Friedrich-von-Weizsäcker-Zentrum für Naturwissenschaft und Friedensforschung der Universität Hamburg, 2009.

[72] Eugenio Eibenschutz Abeles. Thermosiphon engine and method, May 10 1977. US Patent 4,022,024.

[73] Aniruddha Pal, Yogendra Joshi, Monem H Beitelmal, Chandrakant D Patel, and Todd Wenger. Design and Performance Evaluation of a Compact Thermosyphon. URL `http://www.hpl.hp.com/research/papers/2002/thermosyphon.pdf`.

[74] Tom Shutt. Construction of the LUX Dark Matter Experiment at the Sanford Underground Science and Engineering Laboratory. pages 1–35, August 2007.

[75] D.S. Akerib, X. Bai, S. Bedikian, E. Bernard, A. Bernstein, A. Bolozdynya, A. Bradley, D. Byram, S.B. Cahn, C. Camp, M.C. Carmona-Benitez, D. Carr, J.J. Chapman, A. Chiller, C. Chiller, K. Clark, T. Classen, T. Coffey, A. Curioni, E. Dahl, S. Dazeley, L. de Viveiros, A. Dobi, E. Dragowsky, E. Druszkiewicz, B. Edwards, C.H. Faham, S. Fiorucci, R.J. Gaitskell, K.R. Gibson, M. Gilchriese, C. Hall, M. Hanhardt, B. Holbrook, M. Ihm, R.G. Jacobsen, L. Kastens, K. Kazkaz, R. Knoche, S. Kyre, J. Kwong, R. Lander, N.A. Larsen, C. Lee, D.S. Leonard, K.T. Lesko, A. Lindote, M.I. Lopes, A. Lyashenko, D.C. Malling, R. Mannino, Z. Marquez, D.N. McKinsey, D.-M. Mei, J. Mock, M. Moongweluwan, M. Morii, H. Nelson, F. Neves, J.A. Nikkel, M. Pangilinan, P.D. Parker, E.K. Pease, K. Pech, P. Phelps, A. Rodionov, P. Roberts, A. Shei, T. Shutt, C. Silva, W. Skulski, V.N. Solovov, C.J. Sofka, P. Sorensen, J. Spaans, T. Stiegler, D. Stolp, R. Svoboda, M. Sweany, M. Szydagis, D. Taylor, J. Thomson, M. Tripathi, S. Uvarov, J.R. Verbus, N. Walsh, R. Webb, D. White, J.T. White, T.J. Whitis, M. Wlasenko, F.L.H. Wolfs, M. Woods, and C. Zhang. The large underground xenon (lux) experiment. *Nuclear Instruments and Methods in Physics Research Section A: Accelerators, Spectrometers, Detectors and Associated Equipment*, 704(0):111 – 126, 2013. ISSN 0168-9002. doi: http://dx.doi.org/10.1016/j.nima.2012.11.135. URL `http://www.sciencedirect.com/science/article/pii/S0168900212014829`.

[76] LUX Collaboration, D S Akerib, X Bai, E Bernard, A Bernstein, A Bradley, D Byram, S B Cahn, M C Carmona-Benitez, J J Chapman, T Coffey, A Dobi,

E Dragowsky, E Druszkiewicz, B Edwards, C H Faham, S Fiorucci, R J Gaitskell, K R Gibson, M Gilchriese, C Hall, M Hanhardt, M Ihm, R G Jacobsen, L Kastens, K Kazkaz, R Knoche, N Larsen, C Lee, K T Lesko, A Lindote, M I Lopes, A Lyashenko, D C Malling, R Mannino, D N McKinsey, D Mei, J Mock, M Moongweluwan, M Morii, H Nelson, F Neves, J A Nikkel, M Pangilinan, K Pech, P Phelps, A Rodionov, T Shutt, C Silva, W Skulski, V N Solovov, P Sorensen, T Stiegler, M Sweany, M Szydagis, D Taylor, M Tripathi, S Uvarov, J R Verbus, L de Viveiros, N Walsh, R Webb, J T White, M Wlasenko, F L H Wolfs, M Woods, and C Zhang. Technical Results from the Surface Run of the LUX Dark Matter Experiment. *arXiv.org*, pages 34–43, October 2012. URL http://arxiv.org/abs/1210.4569v3.

[77] P.J. Linstrom and W.G. Mallard, editors. *NIST Chemistry WebBook, NIST Standard Reference Database Number 69*. National Institute of Standards and Technology, Gaithersburg MD, 20899, retrieved April 14, 2014.

[78] F Mayinger. Classification and applications of two-phase flow heat exchangers. *Lehrstuhl A für Thermodynamik*.

[79] XENON100 Collaboration, E Aprile, K Arisaka, F Arneodo, A Askin, L Baudis, A Behrens, E Brown, J M R Cardoso, B Choi, D Cline, S Fattori, A D Ferella, K L Giboni, A Kish, C W Lam, R F Lang, K E Lim, J A M Lopes, T Marrodan Undagoitia, Y Mei, A J Melgarejo Fernandez, K Ni, U Oberlack, S E A Orrigo, E Pantic, G Plante, A C C Ribeiro, R Santorelli, J M F dos Santos, M Schumann, P Shagin, A Teymourian, E Tziaferi, H Wang, and M Yamashita. The XENON100 Dark Matter Experiment. *Astroparticle Physics*, (9):573–590, July 2011. URL http://arxiv.org/abs/1107.2155.

[80] S Belogurov, A Bolozdyna, D Churakov, A Koutchenkov, V Morgunov, V Solovov, G Safronov, and G Smirnov. High pressure gas scintillation drift chamber with photomultipliers inside of working medium. *IEEE Nucl. Sci. Symp. & Med. Imag. Conf. Rec., San Francisco*.

[81] L dV Luiz. Measurement of the Electron Extraction in Run3. *Tech. Rep. - LUX Internal Note 92*, 2013.

[82] R Knoche. Two New Methods for Extracting Electron Lifetimes. *Tech. Rep. - LUX Internal Note 280*, 2014.

[83] M Szydagis, N Barry, K. Kazkaz, J. Mock, D Stolp, M. Sweany, M. Tripathi, S Uvarov, N. Walsh, and M. Woods. NEST: A Comprehensive Model for Scintillation Yield in Liquid Xenon. *arXiv*, June 2011. URL `http://arxiv.org/abs/1106.613v1`.

[84] Tadayoshi Doke, Akira Hitachi, Jun Kikuchi, Kimiaki Masuda, Hiroyuki Okada, and Eido Shibamura. Absolute Scintillation Yields in Liquid Argon and Xenon for Various Particles. *Japanese Journal of Applied Physics*, 41 (3R):1538–1545, March 2002.

[85] Matthew Szydagis, Adalyn Fyhrie, Daniel Thorngren, and Mani Tripathi. Enhancement of NEST Capabilities for Simulating Low-Energy Recoils in Liquid Xenon. *arXiv*, July 2013. URL `http://arxiv.org/abs/1307.6601`.

[86] Alastair Currie. Best-resolution versus weighting-by-reciprocal-gains energy estimators for a Dahl/NEST ER model. *Tech. Rep. - LUX Internal Note 266*, 2014.

[87] W.-D. Schmidt-Ott, W. Weirauch, F. Smend, H. Langhoff, and D. Gfller. Der zerfall des125m xe, des127m xe und des127g xe. *Zeitschrift fr Physik*, 217(3):282–293, 1968. ISSN 0044-3328. doi: 10.1007/BF01394102. URL `http://dx.doi.org/10.1007/BF01394102`.

[88] D S Akerib, X Bai, S Bedikian, E Bernard, A Bernstein, A Bradley, S B Cahn, M C Carmona-Benitez, D Carr, J J Chapman, K Clark, T Classen, T Coffey, S Dazeley, L de Viveiros, M Dragowsky, E Druszkiewicz, C H Faham, S Fiorucci, R J Gaitskell, K R Gibson, C Hall, M Hanhardt, B Holbrook, M Ihm, R G Jacobsen, L Kastens, K Kazkaz, R Lander, N Larsen, C Lee, D Leonard, K Lesko, A Lyashenko, D C Malling, R Mannino, D N McKinsey, D M Mei, J Mock, M Morii, H Nelson, J A Nikkel, M Pangilinan, P D Parker, P Phelps, T Shutt, W Skulski, P Sorensen, J Spaans, T Stiegler, R Svoboda, M Sweany, M Szydagis, J Thomson, M Tripathi, J R Verbus, N Walsh, R Webb, J T White, M Wlasenko, F L H Wolfs, M Woods, and C Zhang. LUXSim: A Component-Centric

Approach to Low-Background Simulations. *arXiv.org*, November 2011. URL http://arxiv.org/abs/1111.2074v1.

[89] L W Kastens, S Bedikian, S B Cahn, A Manzur, and D N McKinsey. A 83Krm Source for Use in Low-background Liquid Xenon Time Projection Chambers. *JINST*, 5(05):P05006, 2010.

[90] Jonathan Goodman and Jonathan Weare. Ensemble samplers with affine invariance. *Communications in Applied Mathematics and Computational Science*, 5(1):65–80, 2010.

[91] The LUX Collaboration. LUX detector WIMP search calibrations. *In preparation*, 2014.

[92] A Dobi. Calibration of the Large Underground Xenon Detector. *Ph.D. Thesis In Preparation - University of Maryland*, August 2014.

[93] The LUX Collaboration. A tritiated methane source for low energy calibration in the LUX detector. *In preparation*, 2014.

[94] T Takahashi, S Konno, T Hamada, M Miyajima, S Kubota, A Nakamoto, A Hitachi, E Shibamura, and T Doke. Average energy expended per ion pair in liquid xenon. *Physical Review A*, 12(5):1771–1775, November 1975.

[95] C E Dahl, P Kwong, J andPhelps, and T Shutt. Intrinsic xenon response and recombination fluctuations. *In preparation*, 2014.

[96] J C Chapman. First WIMP Search Results from the LUX Dark Matter Experiment. *Ph.D. Thesis - Brown University*, 2014.

[97] A Bradley. LUX Thermosyphon Cryogenics and Radon-Related Backgrounds for the First WIMP Result. *Ph.D. Disseration - Case Western Reserve University*, 2014.

[98] E Aprile and The XENON100 Collaboration. Response of the XENON100 dark matter detector to nuclear recoils. *Physical Review D*, 2013.

[99] E Aprile and XENON100 Collaboration. Dark matter results from 100 live days of XENON100 data. *Physical Review Letters*, 2011.

[100] G Plante, E Aprile, R Budnik, B Choi, and K L Giboni. New measurement of the scintillation efficiency of low-energy nuclear recoils in liquid xenon. *Physical Review C*, 2011.

[101] M Horn, V A Belov, D Y Akimov, H M Araujo, and E J Barnes. Nuclear recoil scintillation and ionisation yields in liquid xenon from ZEPLIN-III data. *Physics Letters B*, 2011.

[102] A Manzur, A Curioni, L Kastens, D N McKinsey, K Ni, and T Wongjirad. Scintillation efficiency and ionization yield of liquid xenon for mono-energetic nuclear recoils down to 4 keV. *Physical Review C*, (2):025808, September 2009. URL http://arxiv.org/abs/0909.1063.

[103] E Armengaud, C Augier, A Benoît, L Bergé, and J Blümer. Final results of the EDELWEISS-II WIMP search using a 4-kg array of cryogenic germanium detectors with interleaved electrodes. *Physics Letters B*, 2011.

[104] D Y Akimov, H M Araujo, E J Barnes, V A Belov, and A Bewick. WIMP-nucleon cross-section results from the second science run of ZEPLIN-III. *Physics Letters B*, 2012.

[105] J Angle, E Aprile, F Arneodo, L Baudis, and A Bernstein. Search for light dark matter in XENON10 data. *Physical review . . .*, 2011.

[106] M Felizardo, T A Girard, T Morlat, A C Fernandes, F Giuliani, A R Ramos, J G Marques, M Auguste, D Boyer, A Cavaillou, J Poupeney, C Sudre, J Puibasset, H S Miley, R F Payne, F P Carvalho, M I Prudêncio, and R Marques. Final Analysis and Results of the Phase II SIMPLE Dark Matter Search. June 2011. URL http://arxiv.org/abs/1106.3014.

[107] XENON100 Collaboration and E Apirle. Dark matter results from 100 live days of XENON100 data. *Physical Review Letters*, 2011.

[108] E Aprile, M Alfonsi, K Arisaka, F Arneodo, and C Balan. Dark matter results from 225 live days of XENON100 data. *Physical Review Letters*, 2012.

[109] C Savage, G Gelmini, P Gondolo, and K Freese. Compatibility of DAMA/LIBRA dark matter detection with other searches. *Journal of Cosmology and Astroparticle Physics*, 2009(04):010–010, April 2009.

[110] Z Ahmed, D S Akerib, S Arrenberg, and C N Bailey. Results from a low-energy analysis of the CDMS II germanium data. *Physical Review Letters*, 2011.

[111] A Currie. Calibration of photomultiplier responses to VUV photons, including two-electron emission. *Tech. Rep. - LUX Internal Note*, 2014.

[112] N Fominykh, J Henk, J Berakdar, P Bruno, H Gollisch, and R Feder. Double-Electron Photoemission from Surfaces. In *Many-Particle Spectroscopy of Atoms, Molecules, Clusters, and Surfaces*, pages 461–470. Springer US, Boston, MA, January 2001.

[113] N Fominykh, J Henk, J Berakdar, P Bruno, H Gollisch, and R Feder. Theory of two-electron photoemission from surfaces. *Solid State Communications*, 113(12):665–669, February 2000.

[114] F Neves, V Chepel, D Yu Akimov, H M Araujo, E J Barnes, V A Belov, A A Burenkov, A Currie, B Edwards, and C Ghag. Calibration of photomultiplier arrays. *Astroparticle Physics*, 33(1):13–18, February 2010.

[115] B Tomasz. Recalibration of the single photoelectron size from corruption of ringing tail distributions and baseline digitization. *Tech. Rep. - LUX Internal Note*, 2014.

[116] The LUX Collaboration. Reanalysis of the first WIMP search results from LUX - *In preparation.* 2014.

[117] INTERNATIONAL ATOMIC ENERGY AGENCY. *Neutron Generators for Analytical Purposes*, volume 1. 2012. ISBN 978-92-0-125110-7.

[118] B Tomasz. First Results from the DD Neutron Generator. *Tech. Rep. - LUX Internal Note 190*, 2014.

[119] J Verbus, C Carmona, R Gaitskell, and S Chan. LUX Low E NR Efficiency from DD Neutrons. *Tech. Rep. - LUX Internal Note 230*, 2014.

[120] C Carmona, J Verbus, and S Chan. LUX Internal Note - NG Simulations: Comparing rates to data and using E_{rec_angle}. *Tech. Rep. - LUX Internal Note 219*, 2014.

[121] J Verbus and The LUX Collaboraiton. Nuclear recoil calibration of the LUX detector using an *in-situ* D-D generator. *In preparation*, 2014.